

Effect of Gold Nanorods on the Performance of Polymer:Fullerene Organic Solar Cells

Mahmoud- Alaa Yahya

A Thesis
In The Department
of
Physics

Presented in Partial Fulfillment of the Requirements
For the Degree of
Doctor of Philosophy (Physics) at
Concordia University
Montreal, Quebec, Canada

March 2013

©Mahmoud-Alaa Yahya, 2013

CONCORDIA UNIVERSITY
School of Graduate Studies

This to certify that the thesis prepared

By: Alaa Mahmoud

Entitled: Effect of Gold Nanorods on the Performance of Polymer:Fullerene
Organic Solar Cells

and submitted in partial fulfillment of the requirements for the degree of

Doctor of Philosophy (Physics)

Complies with the regulations of the University and meets the accepted standards with originality and quality.

Signed by the final Examining Committee:

<u>Prof. Truong Vo-Van</u>	Chair
<u>Prof. Alain Haché</u>	Examiner
<u>Prof. Mojtaba Kahrizi</u>	Examiner
<u>Prof. Laszlo Kalman</u>	Examiner
<u>Prof. Mariana Frank</u>	Examiner
<u>Prof. Ricardo Izquierdo</u>	Co-Supervisor
<u>Prof. Truong Vo-Van</u>	Supervisor

Approved by Prof. Truong Vo-Van
Chair of Department or Graduate Program Director

March 2013 Prof. Brian Lewis
Dean of Faculty

ABSTRACT

Effect of Gold Nanorods on the Performance of Polymer:Fullerene Organic Solar Cells

Alaa Yahya Mahmoud, PhD

Concordia University, 2013

This research is an experimental investigation on the effect of inserting gold nanorods in various locations of conjugated polymer solar cells that comprise poly(3-hexylthiophene-2,5-diyl) as the electron donor, and [6,6]-phenyl-C61-butyric-acid-methyl-ester as the electron acceptor, on the cells performance. Since gold nanorods support at least two major plasmonic modes associated with metallic nanoparticles, incorporating such nanoparticles into thin films of polymer solar cells is supposed to trap light inside the cells in a broad wavelength range, leading to increasing absorptivity as well as power conversion efficiency.

First, several experiments were performed to manufacture devices with a good and reproducible efficiency by optimizing the fabrication conditions, particularly the lithium fluoride thickness as well as the annealing process. This optimization succeeded in producing reproducible devices with an enhanced power conversion efficiency from 0.36% to 1.67%.

Secondly, various approaches were used to introduce gold nanorods in our devices. Rods were deposited in contact with either the cells' front electrode, or the rear one. They were also blended with the solution of the anodic buffer layer, or the one of the photoactive layer. We compared the photovoltaic parameters extracted from completed devices made with/without gold nanorods, as well as their spectroscopic and structure properties. We found that for each location of rods in our devices there was an optimal concentration of the rods to

produce enhancement in the devices' performance. Based on theoretical considerations, devices enhancement was related to either the far field or near field effect induced by the presence of rods. It was found that increasing or decreasing the rods density from the optimal one reduced the overall efficiency of resulting devices. We experimentally verified that there was a relationship between the enhancement in the devices efficiency and the multi-mode excitations associated with gold nanorods. We also found that the influence of plasmonics on absorption of the devices depended on the thickness of the devices' photoactive layers. Using the rod shape of gold nanoparticles to increase the device performance is indeed a promising approach since a fairly low density of the rods in the layer succeeded in increasing remarkably the devices efficiency by up to 21.3 %.

Acknowledgments

I would like to express my special thanks to Prof. Truong Vo-Van and Prof. Ricardo Izquierdo for their supervision, valuable thoughts, and feedback that facilitated my development as a researcher and problem-solver, and helped me gain practical and educational skills.

I thank Prof. Dongling Ma for her help in synthesizing the gold nanorods, Prof. Muthukumaran Packirisamy for access to his laboratory, and Dr. Menouer Saidani for his technical help.

My thanks extend to Prof. Zain Yamani and Prof. Ahmed Mounir with utmost appreciation for their rich advices and discussions that supported me during my long Ph.D. journey.

Great thanks to my beloved family: my parents, brothers and sisters, for their encouraging and valuable support. Without the support and encouragement of my honorable husband and the patience of my kids, I would not have been able to complete my journey.

I would like to acknowledge King AbdulAziz University in Saudi Arabia and the Saudi Cultural Bureau in Canada for supporting my studies and providing me with a generous scholarship.

Dedication

For My Family

Table of contents

List of Figures.....	xii
List of Tables	xxii
List of Acronyms.....	xxiv
CHAPTER I Introduction.....	1
1.1 Solar energy.....	3
1.2 Inorganic solar cells.....	5
1.3 Organic solar cells.....	6
1.4 Motivation.....	8
1.5 Thesis flow	11
CHAPTER II Bulk Heterojunction Organic Solar Cells-Overview	12
2.1 Single and double layer solar cell.....	12
2.2 The concept of bulk heterojunction OSCs.....	13
2.3 BHJ-OSC materials and architecture.....	14
2.3.1 Electron donors (conductive polymer).....	15
2.3.2 Electron acceptors (fullerene C ₆₀ derivatives)	18
2.3.3 Anode materials	20
2.3.4 Cathode materials.....	22
2.4 Photogeneration mechanism in polymer solar cells.....	23
2.4.1 Absorption of the incident photon	23
2.4.2 Generation of excitons	24
2.4.3 Diffusion of excitons.....	24

2.4.4	Dissociation of excitons	24
2.4.5	Dissociation of polarons	26
2.4.6	Transport of charges	26
2.5	Current-voltage characteristics and photovoltaic parameters of OSCs.....	28
2.5.1	Open circuit voltage	30
2.5.2	Short circuit current	30
2.5.3	Fill factor.....	31
2.5.4	Power conversion efficiency.....	31
2.5.5	External quantum efficiency.....	32
2.5.6	Internal quantum efficiency	33
2.6	Loss factors during the PV steps	33
2.6.1	Optical loss.....	33
2.6.2	Nanostructure scale loss.....	34
2.6.3	Electrical mechanism loss.....	34
2.7	Challenges in organic solar cells.....	34
CHAPTER III Surface Plasmon Resonance in Metallic Nanoparticles		37
3.1	Plasma, plasmon, and surface plasmon	37
3.2	Localized surface plasmon resonance	38
3.3	Theoretical considerations of LSPR.....	42
3.3.1	Extinction of the incident light	43
3.3.2	Isotropic sphere: Mie theory	45
3.3.2	Anisotropic sphere: Gans formula	46
3.4	Optical properties of metallic nanoparticles	47

3.4.1	Frequency of the incident light	49
3.4.2	Local dielectric function	49
3.4.3	Anisotropic effect.....	50
3.4.4	Size effect.....	51
CHAPTER IV Plasmonic Solar Cells		54
4.1	Light trapping approaches inside a thin absorber	54
4.1.1	Light trapping using plasmonic scatterers	56
4.1.2	Light trapping via absorbing plasmon	59
4.1.3	Light trapping inside a thin absorber film via plasmon polaritons	60
4.2	Plasmonic in polymer solar cell, a literature review.....	63
4.3	Our objective	63
4.4	Gold nanorods properties.....	64
CHAPTER V Fabrication Process of Bulk Heterojunction Solar Cell.....		71
5.1	Preparation of the ITO-coated glass substrate	72
5.1.1	Preparing the substrate for patterning	72
5.1.2	Patterning the ITO.....	72
5.1.3	Etching ITO	74
5.2	Deposition of the PEDOT:PSS anodic buffer layer	75
5.3	Preparation and deposition of the photoactive solution.....	75
5.4	Thermal evaporation of the cathode materials	78
5.5	Device annealing.....	81
5.6	Characterization of the device	81

CHAPTER VI Optimization of the Fabrication Conditions of P3HT:PCBM Solar	
Cell.....	84
6.1 Optimizing the thickness of LiF.....	84
6.1.1 Procedures.....	85
6.1.2 Results and discussion	85
6.2 Optimizing the thermal annealing process and temperature	88
6.2.1 Effect of thermal annealing of the P3HT:PCBM film on its absorptivity	89
6.2.2 Optimizing the annealing process.....	90
6.2.3 Optimizing the post-annealing temperature.....	92
6.3 Conclusion	95
CHAPTER VII Gold Nanorods Incorporated into Polymer Solar Cells	97
7.1 Gold nanorods and P3HT:PCBM film characteristics.....	97
7.2 Depositing Au NRs in contact with the anodic ITO electrode.....	100
7.2.1 Procedures.....	101
7.2.2 Results and discussions.....	102
7.2.3 Conclusion	111
7.3 Embedding Au NRs in PEDOT:PSS layer	111
7.3.1 Procedures.....	112
7.3.2 Results and discussions.....	113
7.3.3 Conclusion	123
7.4 Mixing Au NRs with P3HT:PCBM layer	124
7.4.1 Procedures.....	125
7.4.2 Results and discussions.....	127

7.4.3 Conclusion	141
7.5 Depositing Au NRs on top of the P3HT:PCBM layer	142
7.5.1 Procedures.....	144
7.5.2 Results and discussions.....	144
7.5.3 Conclusion	152
Main findings and future work.....	153
Bibliography	156
Appendices.....	172
Synthesis of water-based and toluene-based gold nanorods.....	172
Chemicals and Materials.....	172
1. Synthesis of water-based Au NRs [88]:.....	172
2. Synthesis of toluene-based Au NRs [104,105]:.....	173

List of Figures

Figure 1.1: The concentrations of the long-lived greenhouse gases, carbon dioxide, methane and nitrous, in the earth's atmosphere over the last 2,000 years. The concentration units ppm and ppb are parts per million and billion (the number of molecules of the greenhouse gas per million or billion air molecules, respectively, in an atmospheric sample) [adapted from Ref. [1]].	2
Figure 1.2: Best research-solar cell efficiencies according to the National Renewable Energy Laboratory [adapted from Ref. [8]].	5
Figure 1.3: A schematic presentation to the process of producing Si wafer quartz. The energy input for electric-arc furnace is ~100 kWh/kg [adapted from Ref. [12]].	6
Figure 2.1: OSCs architectures and corresponding energy diagrams (a) Schottky; and (b) Heterojunction devices. HOMO: the highest occupied molecular orbital. LUMO: the lowest unoccupied molecular orbital [re-drawn from Ref. [36]].	13
Figure 2.2: The morphology of BHJ-OSC [adapted from Ref. [38]].	14
Figure 2.3: The commonly used conjugated polymers structures and abbreviations. MEH-PPV: poly[2-methoxy-5-(2-ethylhexyloxy)-1,4-phenylenevinylene]; MDMO-PPV: poly[2-methoxy-5-(3',7'-dimethylhexyloxy)-1,4-phenylenevinylene]; P3HT: poly(3-hexylthiophene).	16
Figure 2.4: Formation steps of π bond in C_2H_4 molecule [re-drawn from Ref. [42]].	17
Figure 2.5: The commonly used fullerene derivative and abbreviation. PC ₆₀ BM: [6,6]-phenyl C ₆₁ -butyric-acid-methyl-ester; PC ₇₀ BM: phenyl C ₇₀ -butyric-acid-methyl-ester.	18

Figure 2.6: The absorbance of thin film of P3HT:PCBM on glass.	19
Figure 2.7: HOMO and LUMO energy diagram for both P3HT and PCBM [re-drawn from Ref. [11]].	20
Figure 2.8: The molecular structure for the PEDOT:PSS polymer.	21
Figure 2.9: Schematic illustration of the P3HT:PCBM BHJ device layers.	22
Figure 2.10: Charge transport mechanism in (a) Bi-layer OSC; (b) BHJ-OSC under illumination.	23
Figure 2.11: Schematic diagram of the polymer: fullerene work function and the electron/hole movement.	25
Figure 2.12: Exciton, polaron pair, and polaron [adapted from Ref. [53]].	26
Figure 2.13: Charge transport steps in polymer:fullerene BHJ-OSCs (a) Generation of exciton; (b) Diffusion of exciton to acceptor border; (c) Dissociation of exciton into polaron pair; (d) Dissociation of polaron pair into free polarons; and (e) Polarons transport to corresponding electrodes [adapted from Ref. [50]].	27
Figure 2.14: Schematic diagrams for the equivalent circuit of (a) An ideal solar cell connected to the load R_L ; (b) A real solar cell in which both R_{SH} and R_S are considered, $V_j = V + IR_S$ is the voltage across the junction [re-drawn from Ref. [51]].	28
Figure 2.15: Typical JV characteristic curves for solar cell in dark and under illumination conditions.	29
Figure 2.16: Ideal and practical curves of the EQE for Si-based solar cell. The causes of the deviation from the ideal curve are noted [adapted from Ref. [55]].	32

Figure 2.17: A fraction of the absorbed light by ~100 nm thick P3HT:PCBM film deposited on ITO-coated glass along with the AM1.5 global spectra. The solar radiation data is obtained from Ref. [59].	35
Figure 3.1: Interaction of an EM field with metallic nanosphere creates SPR localized in MNP. The induced dipole oscillates in phase with the <i>E</i> -field of the incoming light [re-drawn from Refs. [64,66]].	40
Figure 3.2: Micrographs of different shapes of MNPs: (a) Ag nanocubes; (b) Au nanostars; (c) Au nanorods; (d) Au nanodiscs; (e) Au nanorings; and (f) Au nanobipyramids [adapted from Ref. [67]].	41
Figure 3.3: Colloidal solutions of various shapes of MNPs [adapted from Ref. [68]].	42
Figure 3.4: Scattering, absorption, and extinction for a spherical particle [adapted from Ref. [67]].	44
Figure 3.5: Changing the color of the gold colloidal solution by reducing the particles diameter [adapted from Ref. [72]].	47
Figure 3.6: The absorption spectra of 5 nm Au NPs synthesized in our lab.	48
Figure 3.7: Extinction efficiency of silver nanoparticles with various shapes: cube , truncated cube (TC), cuboctahedron (CO), icosahedron (IH), and sphere [adapted from Ref. [65]].	50
Figure 3.8: Size confinement effects on the plasmon resonance band for Ag nanoparticles [adapted from Ref. [70]].	51
Figure 3.9: Absorption bands of Au NPs in water, calculated as a function of diameter. The numbers indicates $2R$. As we see, with increasing the particle size, various extinction	

peaks appear, and then peaks fade away until the bulk optical properties of metals remain [adapted from Ref. [74]]. 53

Figure 4.1: (a) A schematic presentation for the optical path length of the incident light through a thin absorber layer; (b) Increasing of the optical path length inside the absorber by using light trapping pyramidal surface texture. 55

Figure 4.2: Three ways to increase the light absorption of a constant thin film absorber using light trapping of MNPs via: (a) Scattering plasmon; (b) Absorbing plasmon; and (c) Plasmon polariton at semiconductor/metal interface [adapted from Ref. [9]]. 56

Figure 4.3: The fraction of light that is scattered to a semiconductor is very sensitive to the shape of MNPs. (a) Ag MNPs of cylindrical or hemisphere shape scatter the incident light more than the spherical one; (b) The optical path length inside the absorber is increased more using the hemisphere particle as compared to the spherical one [adapted from Ref. [69]]. 58

Figure 4.4: Calculation of the near field enhancement around Au nanorod on Si substrate using the Discrete Dipole Approximation method. The value $|E|^2$ is the enhancement in the local electric field. The position of the rod is indicated by the black line [adapted from Ref. [76]]. 60

Figure 4.5: Using a prism to couple the momentum of photon with SP. The prism is placed against a thin metal film in which the metal is the evanescent tunneling barrier. . 61

Figure 4.6: The fraction of the absorbed light inside different semiconductors (Si, GaAs, and PF10TBT:PCBM-termed as pol.) by exciting of the SPP at semiconductor/Al or Ag

interface. The inset shows the confined evanescent wave near the Si/Ag interface [adapted from Ref. [9]].	62
Figure 4.7: Colloidal solutions and the corresponding micrographs of Au NRs with different aspect ratios [adapted from Ref. [71]].	65
Figure 4.8: Elongating of the spherical Au NP along one axis produces rods with different aspect ratios and optical responses. The numbers at the bottom of each bottle indicate the resonance peak [adapted from Ref. [79]].	66
Figure 4.9: The resonance condition ϵ_m/ϵ_d versus the depolarization factor L according to Eq. 3-10 for a sphere ($\epsilon_m/\epsilon_d = -2$, corresponding to $L = 1/3$) and ellipsoids with different aspect ratio (a/b) for different E field polarizations (presented by the arrow next to the ellipsoid) [re-drawn from Ref. [60]].	68
Figure 4.10: SEM micrographs of gold nanorods deposited with various interparticle separations: 20.9, 72.3, and 286.7 nm. The aspect ratio of the rods is ~ 1.7 [adapted from Ref. [80]].	69
Figure 5.1: Schematic diagram of the final configuration of our manufactured OSC device, ITO-coated glass is the anodic substrate; PEDOT:PSS is the anodic buffer layer; P3HT:PCBM is the photoactive layer; and LiF/Al is the cathode.	71
Figure 5.2: An SEM image for a pre-cleaned ITO-coated glass.	73
Figure 5.3: The geometry of our used mask in the lithography patterning.	73
Figure 5.4: (a) SEM and (b) AFM micrographs of ~ 100 nm P3HT:PCBM film spin-coated on a glass substrate. The images show the phases of P3HT and PCBM. The surface roughness of the P3HT:PCBM is ~ 1.4 nm.	77

Figure 5.5: Schematically diagram for our designed substrate holder.	78
Figure 5.6: Our Al mask on a transparent and flexible film.	79
Figure 5.7: Schematic diagram for the final configuration of the Al shadow mask.	80
Figure 5.8: A substrate with eight devices is ready for characterization.	82
Figure 5.9: Pictures of the designed characterization box show the connecting probes, connecting wires, and the substrate fixer.	83
Figure 6.1: The JV curves for reference device along with devices incorporating LiF as an interfacial layer between organic/Al interface (a) Under illumination and; (b) In dark.	87
Figure 6.2: The absorbance spectra for P3HT:PCBM film before and after thermal annealing for 30 min at 130°C.	89
Figure 6.3: The JV curves for post/pre-annealed OSC devices under illumination and in dark conditions.	91
Figure 6.4: The JV curves for reference device along with devices that were post-annealed at 130, 150 and 170°C for 30 min (a) Under illumination and; (b) In dark.	94
Figure 6.5: The increase in the PCE of our OSC devices during the optimization process.	96
Figure 7.1: A TEM image showing Au NRs on glass.	98
Figure 7.2: The absorption modes of a P3HT:PCBM film (blue curve) and an Au NRs colloidal solution (red curve).	99
Figure 7.3: Location of Au NRs on top of the anode electrode.	100

Figure 7.4: Three approaches of depositing Au NRs on top of ITO-coated glass: (a) Spin-coating; (b) Drop-casting; and (c) Vertical deposition.....	102
Figure 7.5: SEM images for one layer of Au NRs deposited on ITO-coated glass using different methods: (a) Spin-coating; (b) Drop-casting; and (c) Vertical deposition.....	104
Figure 7.6: (a) UV-Vis spectra for one layer of Au NRs deposited on top of ITO-coated glass with various deposition techniques; (b) A comparison between the optical density of P3HT:PCBM with and without Au NRs on the ITO-coated glass with different deposition techniques of the rods.	105
Figure 7.7: The JV curves for devices without Au NRs (ITO/P3HT:PCBM/LiF/Al) and with Au NRs (ITO/AuNRs/P3HT:PCBM/LiF/Al) (a) Under illumination and; (b) In darkness.....	107
Figure 7.8: UV-Vis spectra for Au NRs vertically deposited on ITO-coated glass with various periods.....	109
Figure 7.9: OSC device structure with Au NRs embedded in the PEDOT:PSS layer. .	112
Figure 7.10: Schematic representation of the Au NRs solution percentages that were mixed with the PEDOT:PSS solution.	113
Figure 7.11: An SEM micrograph of PEDOT:PSS:AuNRs film made with 15% of Au NRs solution in the PEDOT:PSS solution. The bar in the inset indicates 300 nm.....	114
Figure 7.12: The JV curves for reference device along with devices incorporating Au NRs in the PEDOT:PSS layer (a) Under illumination and; (b) In dark.....	116
Figure 7.13: (a) A comparison between the absorption profiles of the P3HT:PCBM films made with three different conditions: thick-pristine (green- \diamond), thin-pristine (blue - Δ), and	

thick with AuNRs spin-coated on top of it (brown-O). The difference between the absorbance of thick and thin films is presented by the black+ curve, and the difference between the absorbance of pristine and Au NRs film is presented by the red-x one. The inset shows the absorbance of both black+ and red-x profiles alone; (b) A comparison between the absorption spectra of Au NRs solution and the difference between films (I) & (II). 119

Figure 7.14: (a) The EQE spectral response for reference device along with the 15% Au NRs one; (b) The increase in the EQE with 15% Au NRs device along with the absorbance of the Au NRs solution. The curve has been smoothed and the bars indicate the errors. 121

Figure 7.15: The energy band diagram of the used materials showing the good match of the Au NRs work-function with the HOMO of the polymer (P3HT_H) and the work-function of PEDOT:PSS. 123

Figure 7.16: OSC device structure with Au NRs embedded in the P3HT:PCBM photoactive layer. 125

Figure 7.17: Schematic representations of the volume percentages of Au NRs, P3HT:PCBM, and 1,2-dichlorobenzene that were used in our experiment for preparing the P3HT:PCBM: AuNRs solutions. 126

Figure 7.18: SEM image showing the toluene-based Au NRs on ITO-coated glass. The white droplet-like structures indicate the rods. 127

Figure 7.19: Spectra comparison between Au NRs toluene based and water based solutions along with the spectra of P3HT:PCBM film. 129

Figure 7.20: The JV curves for reference device along with devices incorporating Au NRs in the photoactive layer (a) Under illumination and; (b) In dark.....	131
Figure 7.21: Schematic representations of the volume percentages of Au NRs, P3HT:PCBM, and 1,2-dichlorobenzene that were used in preparing the P3HT:PCBM:AuNRs thin/thick films.....	133
Figure 7.22: The JV curves for reference thick/thin P3HT:PCBM devices along with devices incorporating 6.25% Au NRs in the photoactive layer (a) Under illumination and; (b) In dark.	135
Figure 7.23: (a) A comparison between the absorption of pristine thick/thin photoactive layer along with the corresponding ones that contain Au NRs; (b) The increase in the absorbance of the thick/thin films after incorporating Au NRs along with the NR toluene-based spectra. It is clear that the influence of the rods on the thin photoactive film is larger than that in the thick one.....	138
Figure 7.24: AFM micrographs for (a) Thick P3HT:PCBM film; (b) Thick P3HT:PCBM:AuNRs film; (c) Thin P3HT:PCBM film; and (d) Thin P3HT:PCBM:AuNRs film. The bars indicate 1.25 microns. While the surface roughness of the films, ~ 1.4 nm, did not change after incorporating the rods, the morphology of the films changed for both cases.....	140
Figure 7.25: OSC device structure with Au NRs deposited on top of the P3HT:PCBM photoactive layer.....	143

Figure 7.26: SEM images for various layers of Au NRs spin-coated on ITO-coated glass: (a) 1 layer; (b) 3 layers; and (c) 5 layers. The white droplet-like structures indicate the Au NRs. The bar indicates 2 microns. 145

Figure 7.27: UV-Vis spectra for 1, 3, and 5 layers of Au NRs spin-coated on top of ITO-coated glass. 146

Figure 7.28: The JV curves for reference P3HT:PCBM device along with devices incorporating 1, 3, and 5 layers of Au NRs on top of P3HT:PCBM (a) Under illumination and; (b) In dark..... 148

Figure 7.29: (a) The J_{sc} spectral response for pristine P3HT:PCBM device along with the P3HT:PCBM: AuNRs (1 layer) one; (b) J_{Re} / J_{NR} spectra (for 1 layer NRs) along with the absorbance of the Au NRs water-based solution. The curve has been smoothed and the bars indicate the errors. 151

List of Tables

Table 1: <i>The average PV parameters for reference device along with the ones incorporated LiF between P3HT:PCBM/Al interface. These values were obtained from at least five devices made under the same conditions.</i>	86
Table 2: <i>The average PV parameters for devices those were pre- and post-annealed. These values were obtained from at least five devices made under the same conditions.</i>	91
Table 3: <i>The average PV parameters for reference device along with devices that were post-annealed at 130, 150 and 170°C for 30 min. These values were obtained from at least five devices made under the same conditions.</i>	93
Table 4: <i>The PV parameters for pristine reference devices and devices in the presence of Au NRs on top of ITO-coated glass for different deposition methods.</i>	108
Table 5: <i>The PV parameters for pristine reference devices and devices in the presence of Au NRs on top of ITO-coated glass for different Au NR vertical deposition times.</i>	109
Table 6: <i>The average PV parameters for reference and PEDOT:PSS:AuNRs devices. The standard deviation is calculated for all parameters.</i>	115
Table 7: <i>The average PV parameters for reference and P3HT:PCBM:AuNRs devices, and the corresponding standard deviation.</i>	130
Table 8: <i>The average PV parameters for reference and P3HT:PCBM:AuNRs devices for thick and thin P3HT:PCBM layer, and the corresponding standard deviation.</i>	134

Table 9: <i>The area under the absorbance curves, figure 7.24a, of thin/thick films with/without Au NRs nanorods.</i>	137
Table 10: <i>The average PV parameters for pristine and P3HT:PCBM/AuNRs devices with 1,3, and 5 layers of the rods, and the corresponding stander deviation.</i>	147
Table 11: <i>The effect of using different approaches of incorporating Au NRs in BHJ-OSC devices in the PV parameters of the resulting devices.</i>	153

List of Acronyms

T	Absolute temperature
A	Absorbance
C_{abs}	Absorption cross section
Al	Aluminum
ϕ_{Al}	Aluminum work function
ABL	Anodic buffer layer
AFM	Atomic force microscopy
ATR	Attenuated total reflection
k_B	Boltzmann's constant
w_p	Bulk plasmon frequencies
CdTe	Cadmium telluride
N	Charge density
CIGS	Copper indium gallium selenide
JV	Current-voltage characteristics
DI-water	Deionized water
L	Depolarization factor
ϵ_d	Dielectric function of the medium
ϵ_m	Dielectric function of the metal
I_d	Diode current
E	Electric field
EM	Electromagnetic field
e	Electronic charge

<i>m</i>	Electronic mass
<i>E_g</i>	Energy gap
EQE	External quantum efficiency
<i>C_{ext}</i>	Extinction coefficient
fs	Femtosecond = 10^{-15} sec
FF	Fill factor
ϵ_0	Free space permittivity
GaAs	Gallium arsenide
GW	Gigawatt = 10^9 Watt
Au	Gold
Au NRs or AuNRs	Gold nanorods
HOMO	Highest occupied molecular orbital
h	Hour
PVDF membrane	Hydrophilic polyvinylidene fluoride membrane
ϵ''	Imaginary part of metallic dielectric function
IPCE	Incident photon to carrier efficiency
<i>P_{in}</i>	Incident power
ITO	Indium tin oxide
<i>I_i</i>	Intensity of incident radiation
<i>I_t</i>	Intensity of transmitted radiation
IQE	Internal quantum efficiency
J	Joule = Watt \times Second
kW	Kilowatt = 10^3 Watt

ϕ_{ITO}	ITO work function
LiF	Lithium fluoride
R_L	Load resistance
LSPR	Localized surface plasmon resonance
LUMO	Lowest unoccupied molecular orbital
J_{max}	Maximum current
V_{max}	Maximum voltage
MNP	Metallic nanoparticle
min	Minute
$\hbar k_{\text{SP}}$	Momentum of surface plasmon polariton
NP	Nanoparticle
NR	Nanorod
ns	Nanosecond
NREL	National Renewable Energy Laboratory
V_{os}	Open circuit voltage
OSCs	Organic solar cells
P_{out}	Output power
PCBM or PC₆₀BM	[6,6]-phenyl C ₆₁ -butyric-acid-methyl-ester
I_{ph}	Photogenerated current
h	Planck's constant
α	Polarizability of metallic particle
P3HT	Poly(3-hexylthiophene)
PEDOT	Poly(3,4-ethylenedioxythiophene) doped

PSS	Polystyrenesulfonic acid
PTFE membrane	Polytetrafluoroethylene membrane
PCE	Power conversion efficiency
R	Radius of metallic nanoparticle
ϵ'	Real part of metallic dielectric function
n	Refractive index of free space
I_s	Reverse saturation current
SEM	Scanning electron microscopy
C_{sca}	Scattering cross section
R_S	Series resistance
sec	Second
J_{sc}	Short circuit current
R_{SH}	Shunt resistance
Si	Silicon
Ag	Silver
c	Speed of light
RPM	Speed of spin-coater and centrifugator
STC	Standard test conditions
SP	Surface plasmon
w_{SP}	Surface plasmon frequency
SPP	Surface plasmon polariton
TW	Terawatt = 10^{12} Watt
TEM	Transmission electron microscopy

l	Travelling distance (optical path)
V	Voltage across the cell
U	Volume
λ	Wavelength
K_{photon}	Wave vector of photon

CHAPTER I

Introduction

The average changes in the patterns of the earth's weather, or climate change, has been recently related to the rapid increase in the greenhouse gases in the earth's atmosphere. Some of the greenhouse gases, namely water vapor and carbon dioxide, are naturally available in the atmosphere. Yet, as figure 1.1 illustrates, their level has been increased over the last hundreds years due to human activities such as deforesting and burning fossil fuel (coal, oil, and gas). Besides such activities, other kinds of greenhouse gases: methane, nitrous oxide and ozone are released. Normally, part of the Sun's heat is absorbed by the earth's atmosphere, while the rest is reflected back to the space. When the concentrations of the greenhouse gases in the atmosphere increase, probably more infrared radiation will get trapped in it, resulting in the increase of the earth's temperature. This greenhouse effect causes the global warming of the planet [1,2].

The change in the climate affects both global temperature and water precipitations. In addition, it plays a certain role in raising the sea level. These effects have various impacts on the nature of the life on earth, in the context of general health (air quality, illnesses, infectious diseases, heat-related death), agriculture, water recourses (quality and supply), wild life and coastal areas [1].

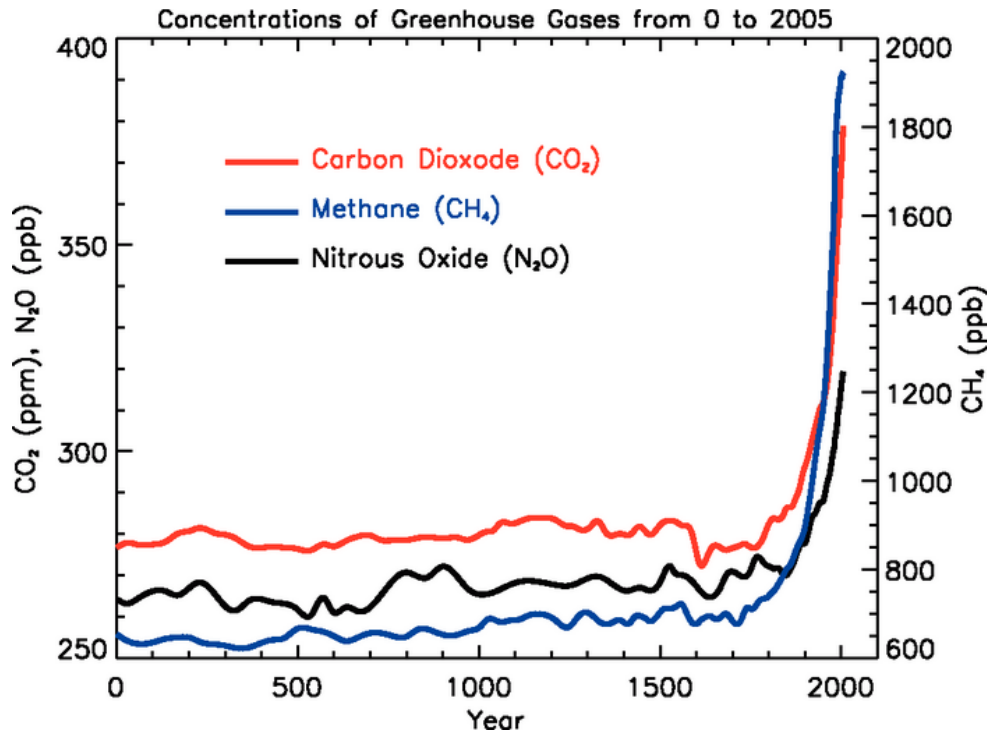


Figure 1. 1: The concentrations of the long-lived greenhouse gases, carbon dioxide, methane and nitrous, in the earth's atmosphere over the last 2,000 years. The concentration units ppm and ppb are parts per million and billion (the number of molecules of the greenhouse gas per million or billion air molecules, respectively, in an atmospheric sample) [adapted from Ref. [1]].

To reduce the emission of greenhouse gases, sources of the emission free greenhouse gases (also referred as green energy or renewable energy resources) have to be utilized wisely. The renewable energy technologies include the following: power of falling water (hydropower), wave and tidal power (ocean energy), wind energy, energy that is extracted from living and recently live organisms (biomass energy), and solar energy. Today, the total global power consumption is ~ 13.5 TW [3], in which ~ 85% comes from the fossil fuel, ~ 2% is generated from nuclear energy, while the rest, ~13%,

is extracted from green energy resources [2,4]. To stabilize the change in the climate, a 30 TW emission-free power has to be installed by the mid of this century [2].

1.1 Solar energy

A closer statistical look among the various types of renewable energy resources shows that sun energy is the most abundant one. Sun deposits around 4.3×10^{20} J/h, which is larger than the total global consumption of energy in one year [3]. To utilize this resource, solar energy radiation is converted into usable forms of energy, thermal energy as in heating water and warming houses, or electrical energy as in solar cells. Thermal energy is generated from the interaction of sunlight with matter. In fact, the low and non-uniform intensity of solar radiation on the earth's surface limits the used of this type of energy. According to Ref. [5], to serve one person using thermal energy, a large area ($\sim 40 \text{ m}^2$) of sunlight collector-plate is required. The second form of solar energy is electric energy that is provided by solar cells, which are devices that take the incident sunlight as an input and convert it into electrical energy through a process called the photovoltaic (PV) effect. In such effect, the absorbed photons generate free charge carriers that produce a current after being passed through an external load [6].

The discovery of the PV effect by French scientist Edmond Becquerel in 1839 took place when he noticed the increase in the generated electricity from two metallic electrodes that were placed in a conductive solution after being exposed to light. Then, other discoveries followed: the solar powered steam engines in 1860 by French mathematician August Mouchet, the photoconductive selenium in 1873 by Willoughby Smith, the first selenium solar cells in 1883 by American inventor Charles Fritts, and the

first published paper on photovoltaic effect by Albert Einstein in 1905. After five decades, particularly in 1954, photovoltaic technology was born when silicon photovoltaic cells were developed at Bell Labs in the United States by Daryl Chapin, Calvin Fuller, and Gerald Pearson. Since then, commercial solar cells have been developed rapidly [7].

A wide view to the solar cells technologies reveals that these technologies are based on two main categories: inorganic and organic solar cells. Figure 1.2 presents the evolution of the efficiency of various types of solar cells according to the National Renewable Energy Laboratory (NREL) in the USA. As figure 1.2 illustrates, there are various types of PV technologies that compete with each other. However, the best one is not always the one that produces the maximum efficiency. A balance between power conversion efficiency and production cost is a very important issue. It is also clear from figure 1.2 that since organic solar cell technologies have been only started in the beginning of the last decade, their efficiency has improved rapidly.

Generally, solar cell devices consist of three main elements: the photoactive layer, i.e. the electron donor and electron acceptor layer, the positive electrode (anode), and the negative one (cathode). The photoactive layer is confined between these two electrodes.

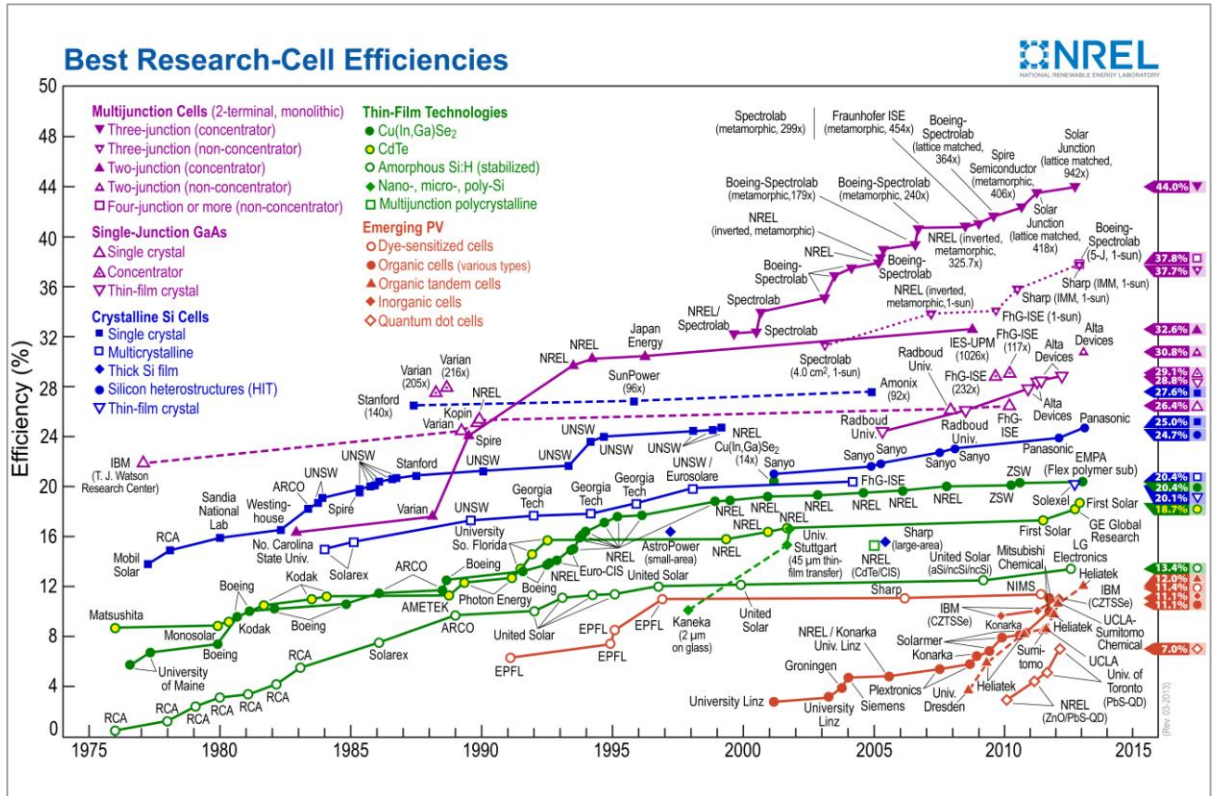


Figure 1. 2: Best research-solar cell efficiencies according to the National Renewable Energy Laboratory [adapted from Ref. [8]].

1.2 Inorganic solar cells

The best solar energy conversion cells so far are found in the traditional type of the inorganic solar cell, i.e. silicon-based solar cells. Basically, inorganic solar cells are comprised of two classes: crystalline solar cells (mono/poly-silicon or III-V semiconductor such as gallium arsenide (GaAs)) and thin-film solar cells such as amorphous silicon, cadmium telluride (CdTe) and copper indium gallium selenide (CIGS). In principle, highly efficient solar cells must have a thickness that is comparable to the charge carriers' diffusion length to limit their recombination, a condition that favors the technology of thin film [9]. At present, around 80% of the PV market is based

on Si wafer technologies, in which the efficiencies of the commercial module reach ~ 20% [10]. The market for Si-based solar cells involves small-scale devices such as calculators, road lamps, water heater, and house roofs. Around 50% of the cost of manufacturing Si-based PV cells is consumed in the preparation process of the Si wafer itself. As figure 1.3 illustrates, the process of producing Si wafer requires high temperature operations, ~1500°C, high vacuum and various steps of lithography [10]. The cost of the generated power from such cells is ~ 0.3/kWh in terms of 2007 American dollars [11].

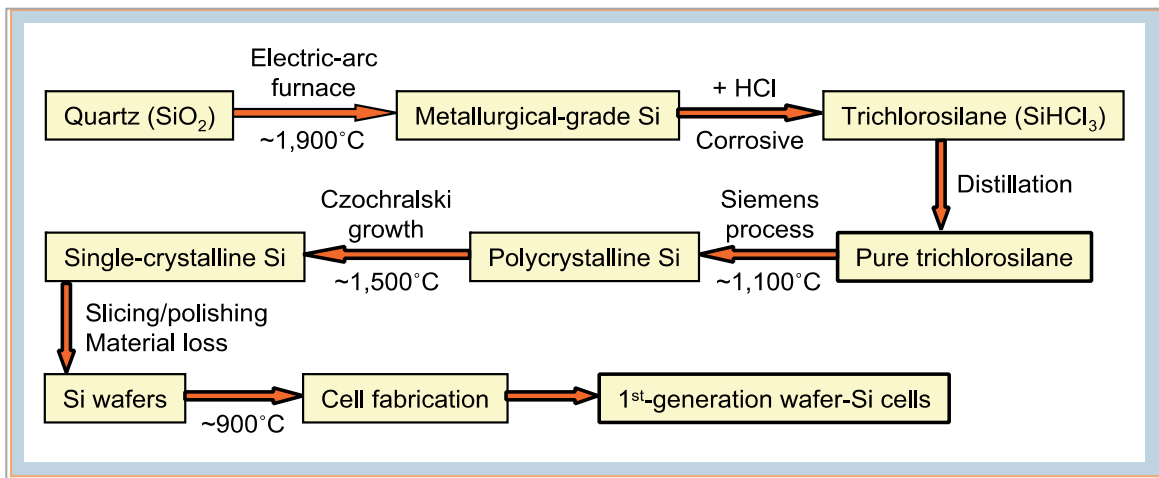


Figure 1. 3: A schematic presentation to the process of producing Si wafer quartz. The energy input for electric-arc furnace is ~100 kWh/kg [adapted from Ref. [12]]

1.3 Organic solar cells

Among the different types of solar cells, the exceptional features of organic solar cells (OSCs) make them most interesting for replacing the Si-based one. In fact, technologies of OSCs have captured the attention of green energy researchers over the

past decade. Because of their solubility in organic solvents, organic solar materials could be used as an ink, and thus produced easily by solution process techniques such as spin-coating, ink-inject printing and screen-printing. Such solution process techniques are characterized with low cost and low temperature operation. Theoretically, 1kWh of the produced electricity using organic solar cell costs ~ 0.01 - 0.02 in terms of 2007 American dollars [11]. Practically, it has been reported that a 1 m^2 of OSC could be produced at a cost that is lower than the monocrystalline Si-based one by an order of 100 times [13]. Furthermore, organic materials are characterized by a large absorption coefficient, above 10^7 cm^{-1} [14], which leads to a good absorption yield. Hence, a very thin organic photoactive layer, i.e. $\sim 100 \text{ nm}$ [14], can absorb a sufficient amount of the sunlight for operation. This in fact lowers the amount of materials that is required to make such cells, which is in favor of this new solar cell technology. In addition, OSCs are flexible, portable and lightweight, which allow them to be simply transported by rolling up into compact cylinders, and easily installed in large areas [15,16].

Generally, OSCs are classified into three categories: a hybrid organic:inorganic structures such as dye sensitized solar cells, small organic molecules solar cells, and conjugated polymer:fullerene derivative solar cells. In our work, we deal with the conjugated polymer solar cells technology since it is a new, promising, and challenging field that has emerged at the beginning of this century, and grown fast over the last decade [17].

1.4 Motivation

The running out of fossil fuels besides ongoing environmental issues associated with these have stimulated scientific research to develop inexpensive, renewable, and efficient energy sources to respond to the global needs of energy. Lewis estimated, in 2006, that the continuous growth in the global population and the economic requests would enlarge the global energy demand from 13.5 TW to ~ 40.8 TW by 2050 [3]. Therefore, improving resources of energy that are environmentally friendly and renewable is one of the essential demands for our society today. Since solar energy is one of the most abundant global green energy resources, converting light energy directly into electricity by means of solar cells has become one of the most pertinent research topics nowadays. During the last decade, the PV industries have grown rapidly with a yearly average growth exceeding 40% [10]. The original goal of the global PV researchers remains to develop a cost effective solar cells that could compete with the conventional fossil energy. Since Si-based PV technologies are facing cost and environmental issues, with an efficiency of commercial module becoming very close to the theoretical predicted limit, i.e. $\sim 30\%$ [18], improving efficient PV devices based on other new technologies, such as organic solar cells that are of smaller thicknesses and lower costs, as a replacement of Si-based one, is a very desirable goal.

Despite the attractive features of polymer solar cells, their low efficiency, $\sim 5\%$ [19,20], remains a main obstacle for their commercialization. Unlike inorganic solar cells, the absorption of light in organic materials creates bounded electron-hole pairs called excitons rather than the free charge carriers as in the inorganic ones. Excitons have to dissociate into free charge carriers to contribute to the photogenerated current. In order

to limit the recombination of free charge carriers after being dissociated, the thickness of the electron donor:acceptor layer has to be in the range of a few hundreds nanometers. This very thin layer, as compared to the 180-300 μm one in Si-based solar cells [9], limits the absorption of the incident light.

Efficient absorption of the solar radiation is necessary for achieving a high performance organic PV device. The introduction of the bulk heterojunction concept has successfully achieved more efficient OSC devices by allowing the use of thicker photoactive films. In such devices, the distance between donor:acceptor interface is reduced, which facilitates the dissociation of excitons, and enhances the PV performance. The effective thickness reported for the photoactive layer used in bulk heterojunction OSCs is normally in the range of 100-300 nm [14]. This value is still low for a complete absorption of the incident light within the absorption range of the photoactive layer. Increase in the optical absorption of the photoactive layer could be achieved by enlarging its thickness. However, due to the fact that the charge carriers have low mobilities [21,22], an enlarging of the thickness of the photoactive layer will result in a recombination of charge carriers before their reaching of the electrodes, as well as the increase in the device series resistance. These factors negatively affect the overall power conversion efficiency (PCE) of the PV cell. Thus, one key issue for reaching a better PCE is to increase the absorption of the photoactive layer without increasing its thickness.

Intensifying the electromagnetic field of the incident light using localized surface plasmon resonance (LSPR) phenomenon in metallic nano-particles/structures is an accessible way for improving the optical absorption of a constant thickness of the photoactive layer [23]. LSPR occurs when the frequency of the electric field of the

incident light resonates with oscillations of the free conduction electrons in metallic nanoparticles (MNP). Consequently, the illuminated particles are excited and strongly absorb/scatter the incident light. This produces a large enhancement, up to a factor of 100 [24], in the local electric field surrounding the particles [25]. Since the resonance frequencies of noble MNPs are located mostly in visible or near infrared region of the spectra [26], incorporating such metallic nanoparticles into OSCs layers could lead to an enhancement in their total absorption of light.

Lots of metallic nano-particle/structures, e.g. gold and silver MNPs, have been incorporated into solar cells to enhance their absorption of light by utilizing the light trapping phenomenon of LSPR [27,28,29,30,31,32,33,34]. The effect of incorporating non-spherical metallic nanoparticle into polymer solar cell layers has not been studied widely whereas all of the earlier studies were performed using relatively spherical particles [29,31]. The facts that the LSPR absorption mode is a shape-dependent property and there are two plasmon modes present motivate the use of gold nanorods in the current work. The choice of gold particularly is due to their photostability in air environment, large scattering cross section, and rich chemistry for the surface functionalization [35]. Besides, the resonance peaks of gold nanorods are situated around the absorption features of our polymer:fullerene photoactive layer.

In this work, we focus on studying the effect of incorporating gold nanorods layer into different locations of our polymer:fullerene bulk heterojunction OSC. We expect that the dwell time of the incident photon inside our organic layer will increase by incorporating gold nanorods into the cells, which increases the absorption of the incident light in the organic layer, and hence enhance their efficiency. Different ways for inserting

nanorods into our solar cells have been considered: embedding them in the photoactive layer, depositing them on the anode, and using them to form a layer on the cathode.

1.5 Thesis flow

This dissertation consists of 7 chapters:

Chapter 2: This chapter highlights some main aspects regarding bulk heterojunction organic solar cells including their operation principal, characterization parameters and challenges that are facing them.

Chapter 3: This chapter describes the origin of the polariton and the localized surface plasmon resonance with an emphasis on the optical characteristics of the latter one.

Chapter 4: This chapter presents the idea of plasmonic solar cells by highlighting some possible approaches that would help in trapping light inside thin film solar cells using plasmonic particles.

Chapter 5: This chapter presents the fabrication processes of our bulk heterojunction polymer:fullerene organic solar cells.

Chapter 6: This chapter presents the optimization processes for the fabrication conditions of P3HT:PCBM solar cell in terms of optimizing lithium fluoride thickness, and the thermal annealing treatment.

Chapter 7: This chapter presents our work in incorporating gold nanorods into different locations in polymer solar cells layers.

CHAPTER II

Bulk Heterojunction Organic Solar Cells-Overview

This chapter highlights some aspects regarding organic solar cell architectures in the context of the idea of single and double layer(s) organic solar cells, followed by the concept of bulk heterojunction solar cells as the best approach so far to increase the efficiency of polymer solar cells. The materials required for processing such solar cells are presented. Then, the charge transport mechanism in such solar cells is explained as well as their characterization parameters. At chapter end, the loss factors during the photovoltaic steps and hence the challenges that are facing the bulk heterojunction polymer solar cells are described.

2.1 Single and double layer solar cell

The first manufactured OSC device had the form of Schottky devices, with a single absorbing layer that is confined between two metallic electrodes, figure 2.1a. This configuration produced devices with a very low efficiency (less than 1%).

In 1985, Tang succeeded in reaching 1% efficiency using a bilayer heterojunction configuration that was comprised of an electron donor layer placed in contact with an electron acceptor one, figure 2.1b. The bilayer configuration was the major breakthrough in the OSCs architecture, which opened the way to the recently developed technology for the current organic PV manufacturing [36].

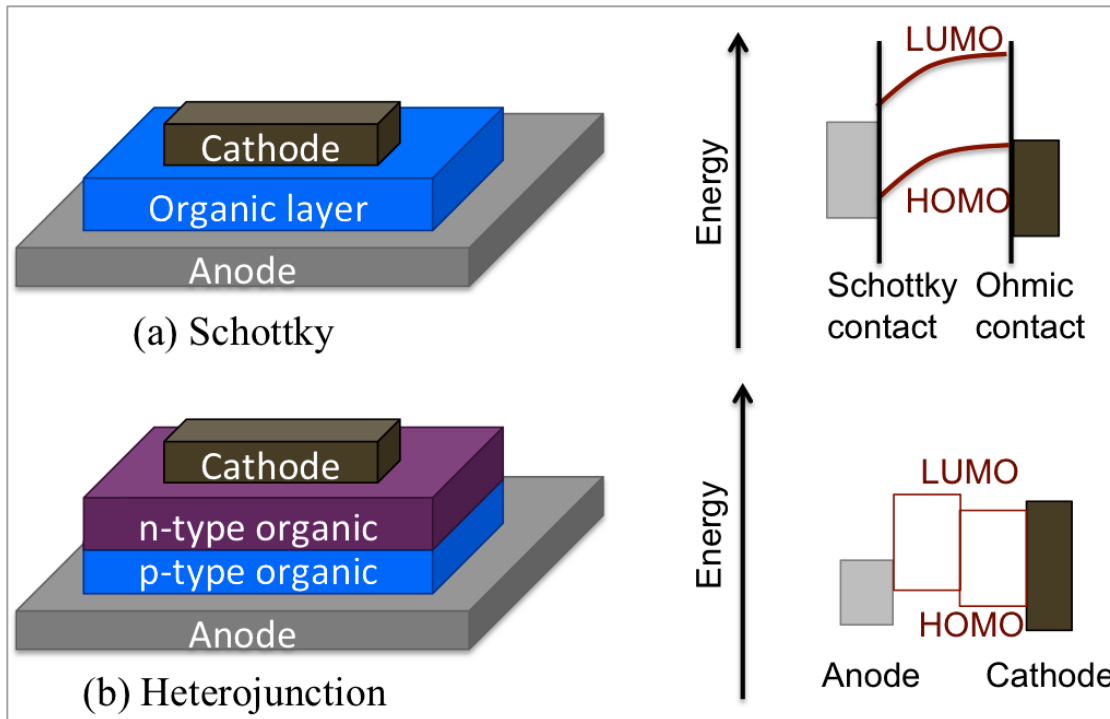


Figure 2. 1: OSCs architectures and corresponding energy diagrams (a) Schottky; and (b) Heterojunction devices. HOMO: the highest occupied molecular orbital. LUMO: the lowest unoccupied molecular orbital [re-drawn from Ref. [36]].

The low efficiency of heterojunction OSC is due to the short diffusion length of the photogenerated charge carriers (the excitons) that is in the range of $\sim 10\text{-}20$ nm. The short diffusion length of exciton increases the possibilities of recombination of free charge carriers, which limits their numbers at electrodes.

2.2 The concept of bulk heterojunction OSCs

In the early nineteen, most of the excitons dissociation problems were circumvented by fabrication of the first efficient bulk heterojunction (BHJ) OSCs. For the BHJ architecture, conjugated polymer (the electron donor) is blended with the fullerene

derivative (the electron acceptor) to form a photoactive layer in OSC devices. In this polymer:fullerene blend, both donor and acceptor exhibit phase separation around 10-20 nm [36].

The BHJ architecture has demonstrated its potential for enhancing the PCE of OSCs due to the facilitation of the excitons dissociation process through a self-assembled interpenetrating network between electron donor and electron acceptor materials [37].

Figure 2.2 depicts the constructed morphology of BHJ-OSCs.

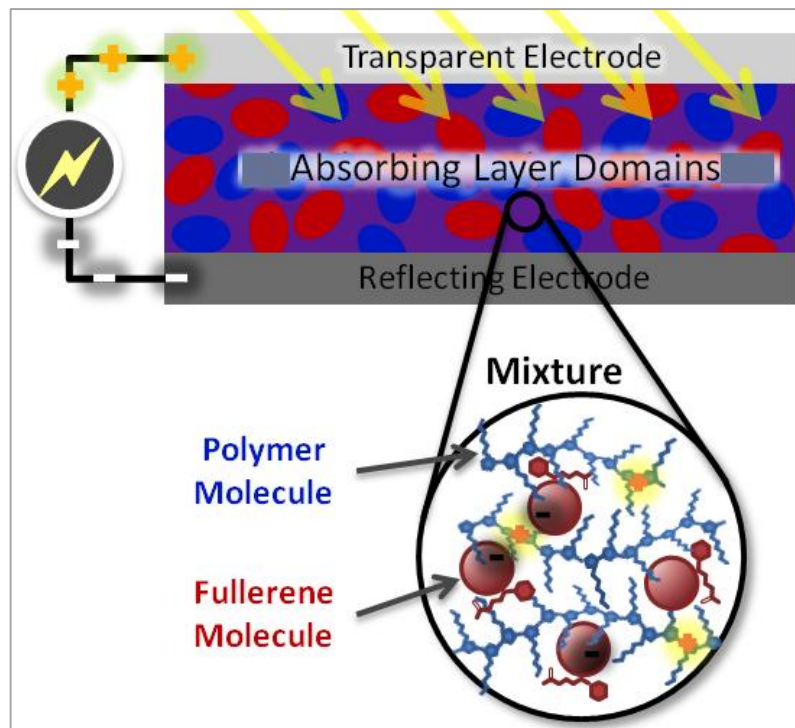


Figure 2. 2: The morphology of BHJ-OSC [adapted from Ref. [38]].

2.3 BHJ-OSC materials and architecture

A typical BHJ-OSC consists of a photoactive layer, a layer of polymer:fullerene blend, that is sandwiched between a transparent positive anode and a metallic negative

cathode. The most commonly used polymer in BHJ-OSCs is the poly(3-hexylthiophene) (P3HT), and the most commonly used fullerene derivative is the [6,6]-phenyl C₆₁-butyric-acid-methyl-ester (PCBM). The PCE of the BHJ-OSC that consists of P3HT:PCBM blend has reached 5% [19].

In contrast to a bilayer OSC device, BHJ device has a lack of symmetry, which results in no net direct movement for the generated free electrons and holes. Therefore, electrodes with different work function are required to overcome the asymmetry breaking condition. Otherwise, the diffusion will act as a driving force on the free charge carriers, in which their recombination will be enhanced [39]. The properties of the materials used in our BHJ-OSCs research are described in the following:

2.3.1 Electron donors (conductive polymer)

Conductive polymers have a conjugated structure, which means that the bonds between carbon atoms are alternatively single or double. In such polymers, the delocalized electrons of the π bonds have the ability to create photogenerated charge carriers upon the absorption of light, making the polymer electrically conductive. The conductive polymer conduct holes, so it works as a *p*-type or electron donor material. Generally, the conductive polymers are considered as a wide bandgap intrinsic semiconductors with energy gap (E_g) above 1.4 eV and below 3 eV. The E_g value of conjugated polymers makes most of them suitable for the optoelectronic applications [39]. Figure 2.3 illustrates the structures of some commonly used conjugated polymer.

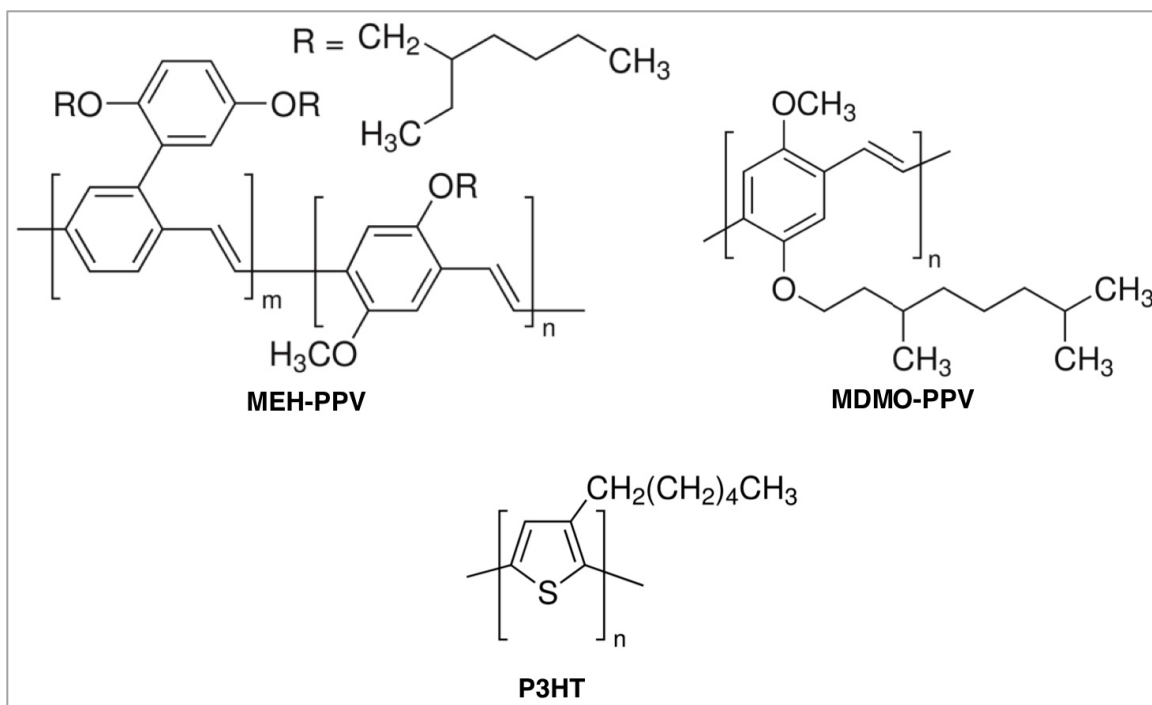


Figure 2. 3: The commonly used conjugated polymers structures and abbreviations. MEH-PPV: poly[2-methoxy-5-(2-ethylhexyloxy)-1,4-phenylenevinylene]; MDMO-PPV: poly[2-methoxy-5-(3',7'-dimethylhexyloxy)-1,4-phenylenevinylene];P3HT: poly(3-hexylthiophene).

Formation of π bond: to form a π bond between carbon atoms in a conjugated molecule, three hybrid sp^2 orbitals form three covalent bonds; two bonds are formed between each adjacent carbon atom, and the third one is formed between the carbon and another group next to it. The remaining electron occupies the p_z orbitals that overlap with each other creating π bonds along the conjugated backbone. The π electrons delocalize and are mobile along the conjugates path, which is the path between the HOMO and LUMO orbitals. The highest filled π orbital is the HOMO, and the lowest empty π^* orbital is the LUMO. The energy between the HOMO and LUMO is the E_g of the polymer [40,41]. Figure 2.4 illustrates the formation steps of π bond in ethylene C_2H_4 molecule.

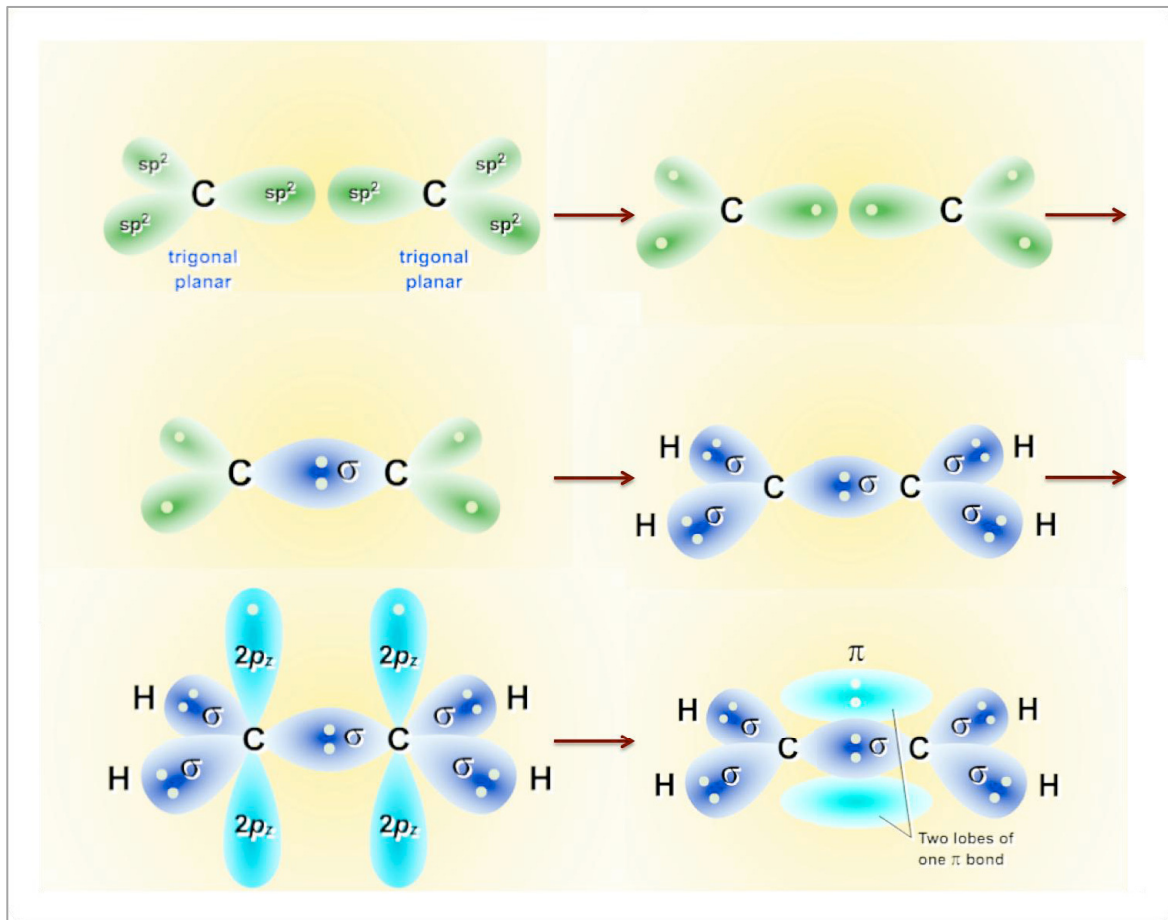


Figure 2. 4: Formation steps of π bond in C_2H_4 molecule [re-drawn from Ref. [42]].

P3HT: among the diversity of polymers, the optoelectronic properties of the P3HT polymer such as high mobility of holes (10^{-4} to 10^{-2} $cm^2 V^{-1}s^{-1}$) [43], chemical stability, high degree of crystallinity, and efficient light absorption (to 650 nm) have made it one of the most promising polymers in organic photovoltaic applications [37,43,44]. The P3HT is soluble in an organic solvent, thus it could be easily deposited using solution depositing techniques.

2.3.2 Electron acceptors (fullerene C₆₀ derivatives)

The buckminsterfullerene C₆₀ is the most used electron acceptor materials in the formation of BHJ-OSCs. It has the ability to conduct electrons, so it acts as an *n*-type material. This soccer-shaped fullerene consists of a one molecule that has 60 carbon atoms attached together with Van der Waals bonds. Figure 2.5 illustrates the chemical formulas of the fullerene C₆₀ and its widely used derivative [39].

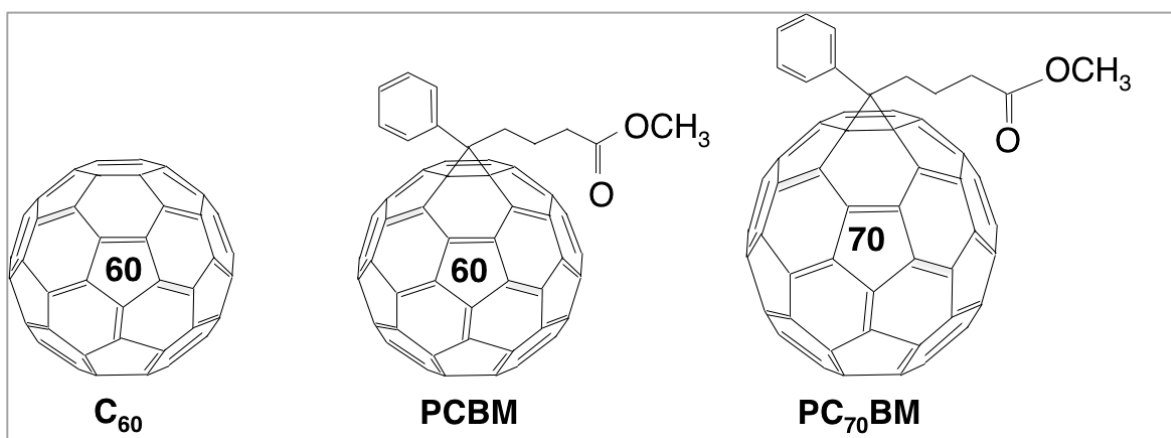


Figure 2. 5: The commonly used fullerene derivative and abbreviation. PC₆₀BM: [6,6]-phenyl C₆₁-butyric-acid-methyl-ester; PC₇₀BM: phenyl C₇₀-butyric-acid-methyl-ester.

PCBM: the most widely used fullerene derivative in polymer:fullerene OSCs is the PCBM due to its high solubility in organic solvents, which allows it to be deposited easily using solution process techniques.

In our work, the photoactive layer consists of the P3HT:PCBM blend, which has a light absorbance that ranges from 320 nm to 650 nm as illustrated in figure 2.6. The

absorbance of the PCMB film ranges from ~ 300 to 500 nm, and the absorbance of the P3HT film ranges from 370 to 650 nm.

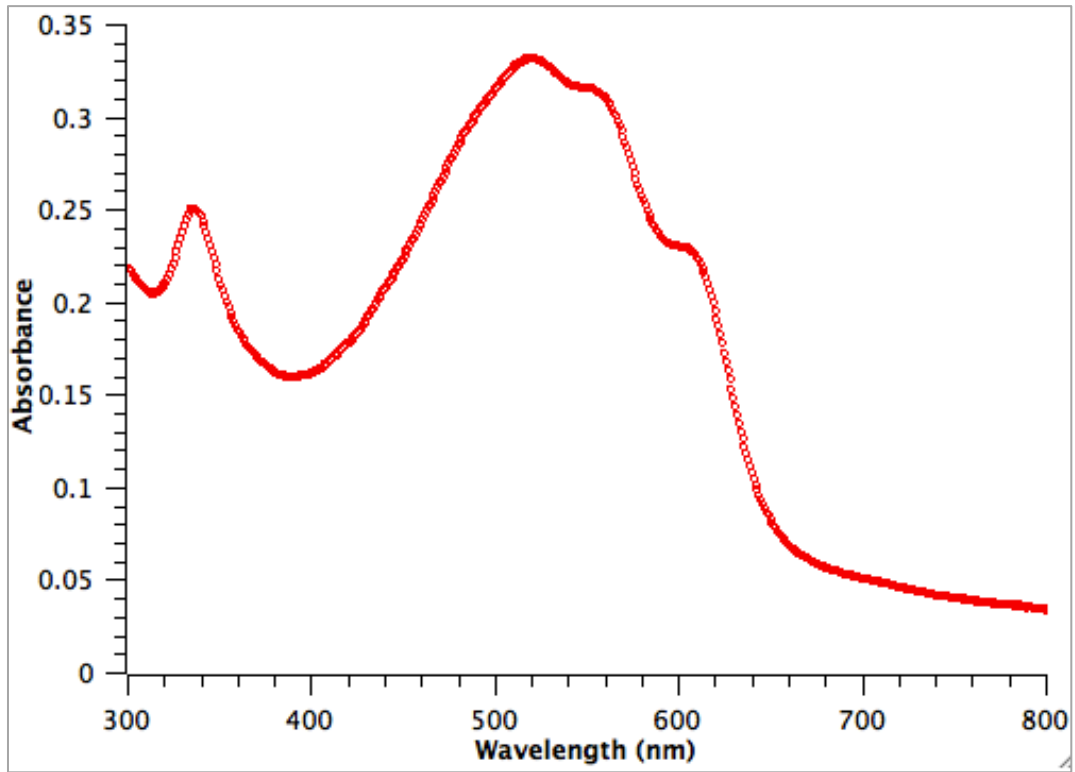


Figure 2. 6: The absorbance of thin film of P3HT:PCBM on glass.

In the P3HT:PCBM blend, the photoactive absorber material is the P3HT polymer, where the efficient excitons are generated. The part of light that is absorbed in the PCBM is not considered in the PCE of the device as the exciton diffusion length in the PCBM fullerene is very small (~ 5 nm) [45]. Figure 2.7 illustrates the energy diagram for both P3HT and PCBM.

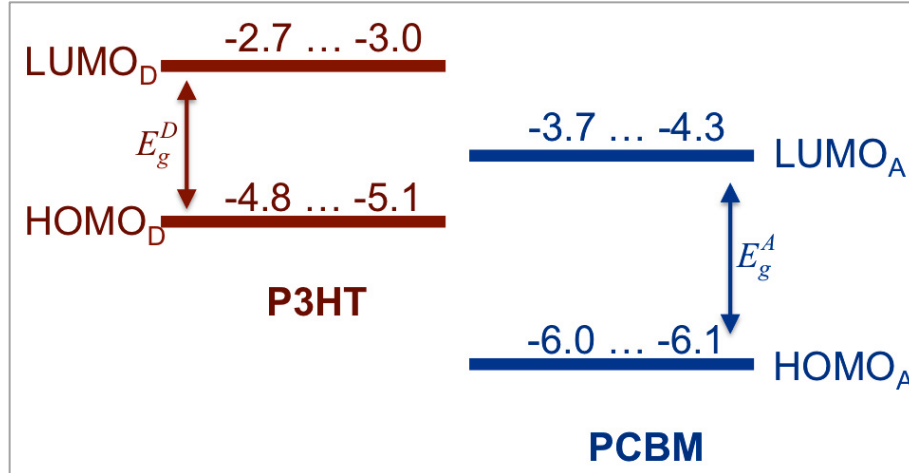


Figure 2. 7: HOMO and LUMO energy diagram for both P3HT and PCBM [re-drawn from Ref. [11]].

2.3.3 Anode materials

Since the anode of the OSC is the part of the cell that is facing the incident light, it has to be transparent or semi-transparent. In OSCs, the anodic electrode collects holes after being dissociated from excitons. Hence, the work function of anode has to be suitable for this function.

ITO: Indium tin oxide (ITO) is commonly used as an anode in OSCs due to its high transparency as well as high conductivity (the sheet resistance is low $\sim 30 \Omega/\text{sq}$) [39]. The ITO work function (ϕ_{ITO}) is $\sim 4.7 \text{ eV}$ [15]. ITO is commercially available and coated on top of a hard or flexible transparent substrate. In our work, the ITO-coated glass is used.

PEDOT:PSS layer: to enhance the interface between the organic layer and the anode, and for further modification in the polarity of ITO to collect holes [46], an ohmic-buffer contact is used. For that purpose, the transparent and conductive polymer

PEDOT:PSS is simply deposited on top of the ITO layer by using a spin-coater. The PEDOT:PSS compound, figure 2.8, consists of the poly(3,4-ethylenedioxythiophene) (PEDOT) that is doped with the polystyrenesulfonic (PSS) acid. The PEDOT:PSS polymer is a water-based solution that is commercially available and widely used in the PV applications. It helps to improve the quality of the ITO electrode by reducing its roughness, which reduces the probability of the short circuit condition between the front/back electrodes. The work function of PEDOT:PSS is ~ 5 eV [47], thus it helps also to enhance the work function of the ITO to better facilitating extraction and injection of holes [19,39].

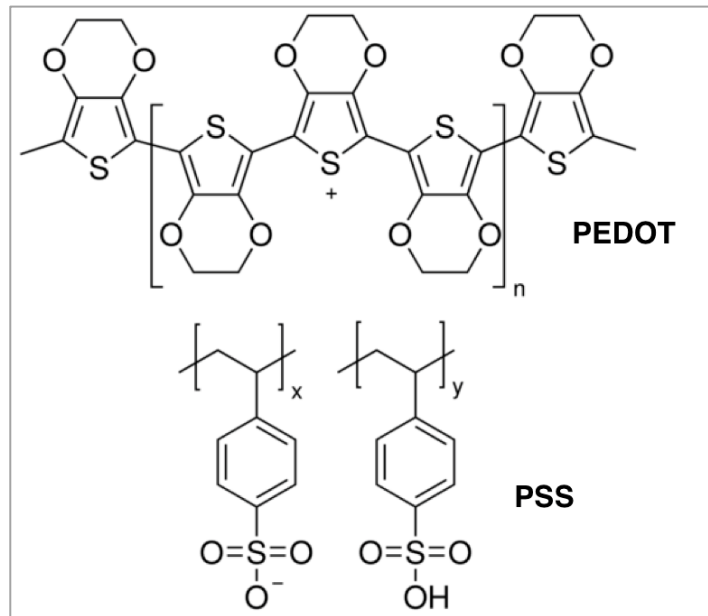


Figure 2. 8: The molecular structure for the PEDOT:PSS polymer.

2.3.4 Cathode materials

Elements with a lower work function as compared to the ITO are used on top of the photoactive layer to form the cathode. Aluminum (work function $\phi_{Al} \sim 4.3$ eV) is usually used in the OSC fabrication due to its stability and wide availability. Raw Al is commercially available in the form of a wire, and is deposited on top of the photoactive layer using thermal evaporation technique.

LiF: a nano-layer of lithium fluoride (LiF) usually is thermally evaporated before the Al cathode to enhance the overall performance of OSC devices. It has been reported that LiF enhances the ohmic contact at the organic/metal interface, lowers the work function of the Al electrode, and enhances the electrons movement to the cathode. Yet, the origin of the enhancement via inserting the LiF layer is not really clear [15,48]. More details about the LiF role are presented in chapter 6. The typical structure of our BHJ-OSC is illustrated in figure 2.9.

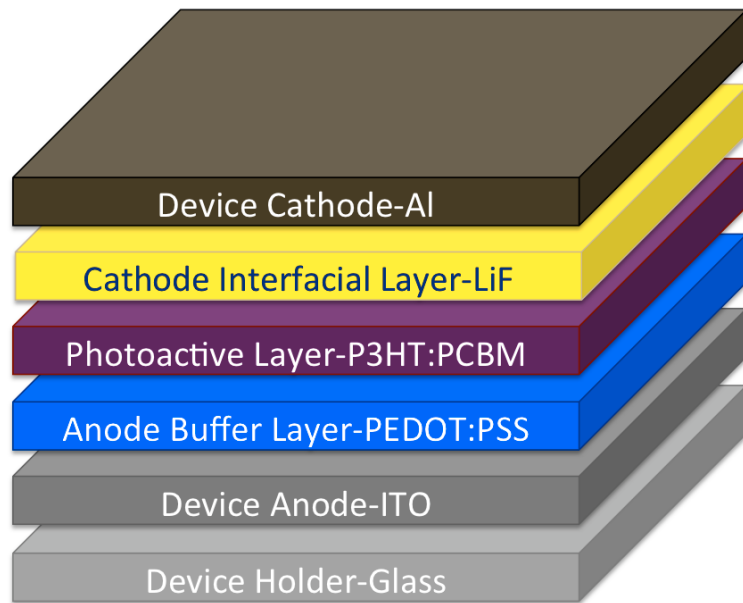


Figure 2. 9: Schematic illustration of the P3HT:PCBM BHJ device layers.

2.4 Photogeneration mechanism in polymer solar cells

Figure 2.10 schematically illustrates the charge transport mechanism in OSCs under illumination. Generally, organic solar cells are operated through six steps:

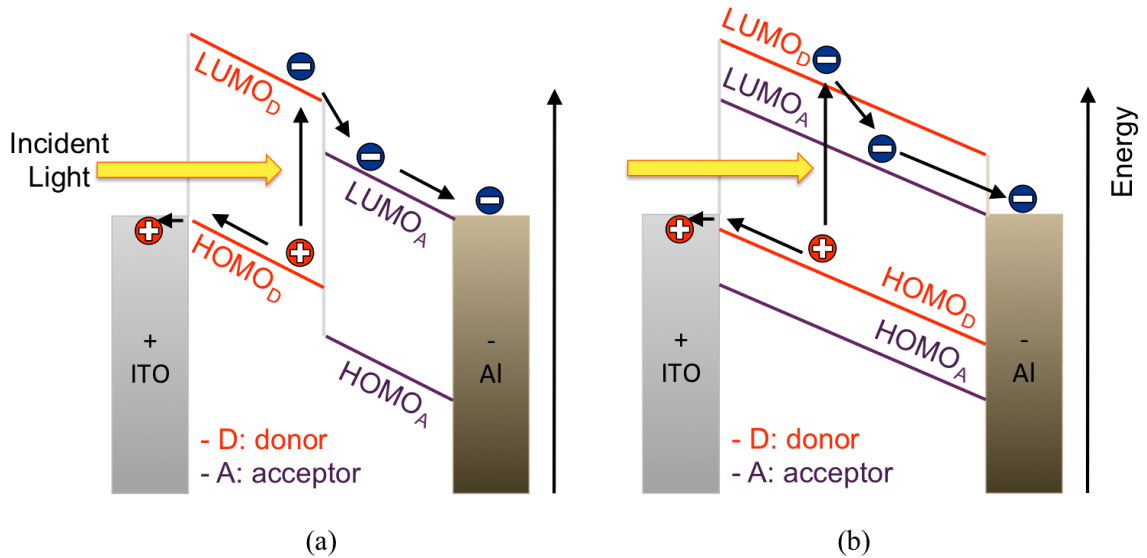


Figure 2. 10: Charge transport mechanism in (a) Bi-layer OSC; (b) BHJ-OSC under illumination.

2.4.1 Absorption of the incident photon

Incident light with energy equal or more than the E_g of the polymer is absorbed in the donor material. Due to the high bandgap of the organic polymers, a small portion of the incident light is absorbed (33% as compared to the Si in which the percentage reaches 77%). However, the high absorption coefficient of organic polymer, $> 10^7 \text{ cm}^{-1}$ [14], allows for a thin film of the photoactive layer, $\sim 100\text{-}300 \text{ nm}$ [14], to absorb most of the incident radiation within the absorption range of the polymer. Yet, this thickness is still larger than the exciton diffusion length (10-20 nm) [15,49,50]. For P3HT, the bandgap is nearly 1.8 eV, thus the longest absorbed photon has a wavelength around 650 nm [49].

The absorption spectra of the P3HT:PCBM blend is illustrated in figure 2. 6

2.4.2 Generation of excitons

Upon light illumination of the photoactive layer with a sufficient incident energy, Frenkel excitons are generated in the polymer chain. Frenkel exciton is an excited quasiparticle - a neutral electron-hole pair that is tightly bounded together by coulombic force. In organic materials, the binding energy of the photogenerated excitons is high, ~ 0.5 eV [14], due to their small dielectric constant that ranges between 3 and 4 [14]. The incident energy that is required to create these excitons is less than the energy gap of the polymer by the amount of exciton binding energy. [15,50,51].

2.4.3 Diffusion of excitons

The strongly coulombic bounded exciton in organic materials exhibits a very short lifetime ~ 1 ns [14], and moves through the polymer only by the diffusion mechanism with a very short diffusion length, ~ 10 -20 nm. To dissociate excitons into free charges, an electron acceptor material has to be located within the exciton diffusion length. Otherwise, radiative recombination occurs [50,52].

2.4.4 Dissociation of excitons

Generally for a heterojunction between two materials with different work functions, the internal electric field allows electrons to flow to the lower work function material until the Fermi level of the two materials meets. In our case, there is an internal electric field between the polymer/fullerene borders, thus electrons flow to the acceptor (fullerene) domain, figure 2.11.

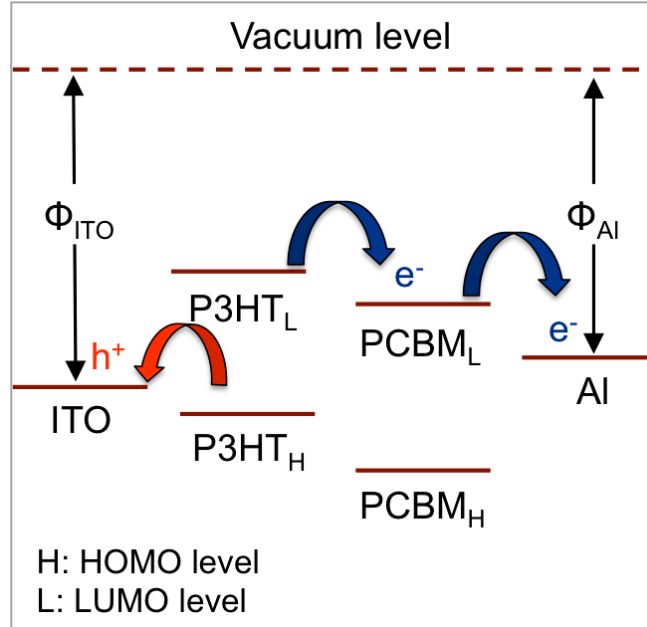


Figure 2. 11: Schematic diagram of the polymer: fullerene work function and the electron/hole movement.

The dissociation of excitons means the separation of excitons into polaron pairs. The polaron is the coupling between a charge (electron or hole) and a lattice phonon, or simply is “a charge plus a distortion in the charge’s surroundings” [53]. The polaron pair is a Coulomb bounded pair of positive and negative polarons that are located on different molecules. When an exciton diffused to the donor/acceptor boundary, negative polaron moves from the $LUMO_D$ to the $LUMO_A$, and the positive polaron remains in the polymer. This positive-negative polaron pair is Coulomb bounded also, and is called polaron pair. The exciton dissociation to polaron pair is an intermediate step from a bounded electron-hole pair to a free polaron pair that is not bounded any more. This dissociation is a very fast transition in polymer solar cells as it occurs within 100 fs [15,49,50,53]. Figure 2.12 schematically illustrates the difference between exciton, polaron pair and polaron.

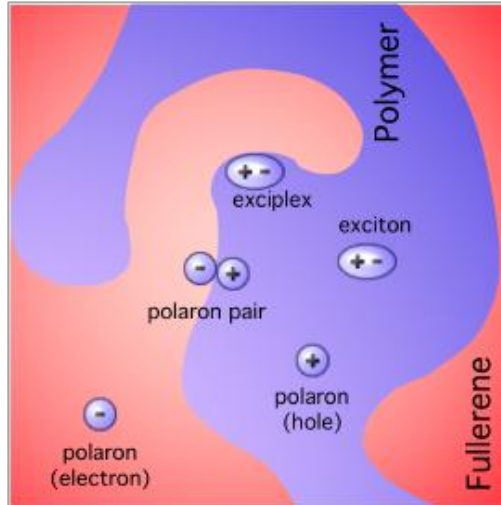


Figure 2. 12: Exciton, polaron pair, and polaron [adapted from Ref. [53]].

2.4.5 Dissociation of polarons

The dissociation of the polaron pairs into free polarons (free electron-hole pairs) depends strongly on the applied electric field, which is the external electric field that is induced from electrodes with different work functions. Thus both electrodes have to be chosen carefully according to their work functions [50,52].

2.4.6 Transport of charges

After the polaron dissociation into free electron-hole pairs, the electric field drives both electron and hole to their corresponding electrodes. The transition of the free charges to their corresponding electrodes is a hopping mechanism, which is very slow. By polarons hopping to their corresponding electrodes, a photocurrent is then generated. The recombination of free polaron pairs with other mobile charges or with traps

decreases the photogenerated current. Figure 2.13 depicts the steps of the charge transport mechanism in BHJ polymer:fullerene OSCs [15,49,50,52].

In bulk heterojunction, the asymmetrical discontinuous network between the acceptor/donor phases leads to trapping states that lower the carriers mobility, by a factor of 1000 less than in crystalline Si-based solar cells [50].

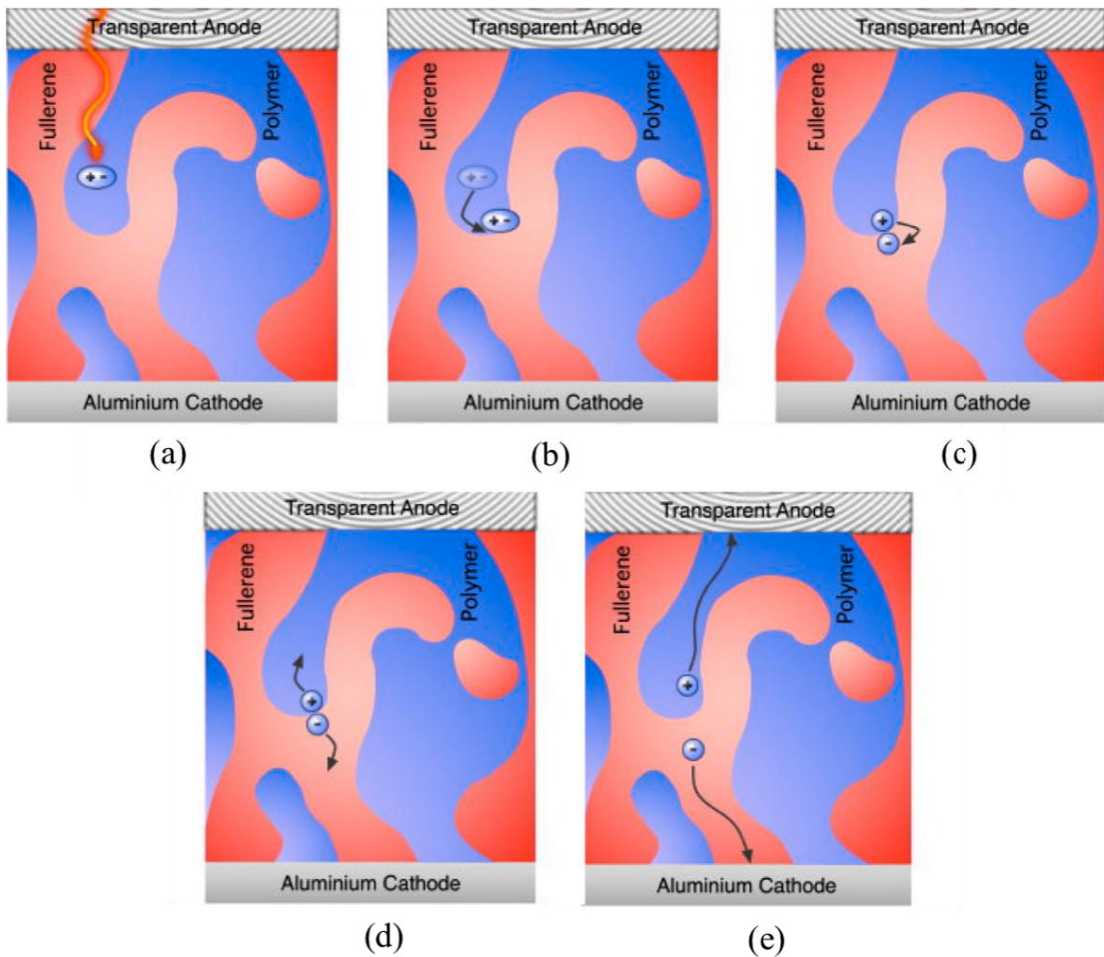


Figure 2. 13: Charge transport steps in polymer:fullerene BHJ-OSCs (a) Generation of exciton; (b) Diffusion of exciton to acceptor border; (c) Dissociation of exciton into polaron pair; (d) Dissociation of polaron pair into free polarons; and (e) Polarons transport to corresponding electrodes [adapted from Ref. [50]].

2.5 Current-voltage characteristics and photovoltaic parameters of OSCs

The total current (I) through the load resistance (R_L) that is connected to an ideal solar cell, figure 2.14a, is given from the Schottky diode equation¹ as:

$$I = I_{ph} - I_d = I_{ph} - I_s \left[\exp\left(\frac{eV}{k_B T}\right) - 1 \right] \quad (2-1)$$

where I_d is the diode current, I_{ph} is the photogenerated current, I_s is the reverse saturation current, e is the electronic charge, V is the voltage across the cell, k_B is the Boltzmann's constant, and T is the absolute temperature [6].

In a real cell, figure 2.14b, the shunt (R_{SH}) and series (R_S) resistances result in non-negligible resistances with respect to the R_L . Hence, the general equation for the current-voltage characteristic through the cell becomes [51]:

$$I = I_{ph} - I_s \left[\exp\left(e \frac{V + IR_S}{k_B T}\right) - 1 \right] - \frac{V + IR_S}{R_{SH}} \quad (2-2)$$

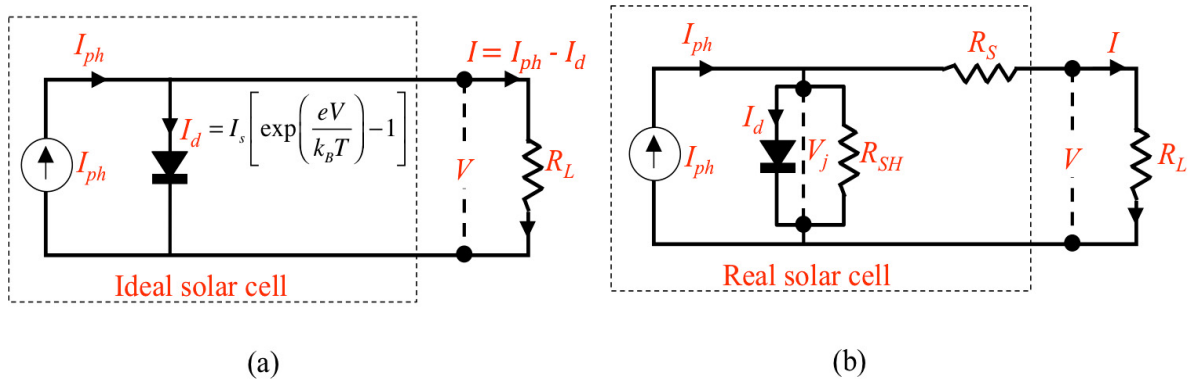


Figure 2. 14: Schematic diagrams for the equivalent circuit of (a) An ideal solar cell connected to the load R_L ; (b) A real solar cell in which both R_{SH} and R_S are considered, $V_j = V + IR_S$ is the voltage across the junction [re-drawn from Ref. [51]].

¹ Although the Schottky diode equation is derived for inorganic devices, it is applicable in OSC too [14].

For a good PV behavior, low value of R_S and high value of R_{SH} are required. The R_S is related to the sheet resistance of the cell. In another word, it is the resistance of the cell material to the current flow. This includes the ohmic loss that could be through the photoactive layer, metal/organic interface, or electrodes. R_{SH} is related to the leakage of the current between the electrodes as it deflects the current away from them [19,51].

The overall response of the solar cell under illumination and in dark conditions is described by the current-voltage (JV) characteristic curves given in figure 2.15. Most of figure of merit parameters of the PV cell is extracted from this curve. The output power (P_{out}), which is the rectangular area that is confined by maximum current (J_{max}) and maximum voltage (V_{max}), is the maximum power delivered to the load. The maximum desirable power of the cell is the rectangular area that is confined by the open circuit voltage (V_{oc}) and the short circuit current (J_{sc}) [6,51,54].

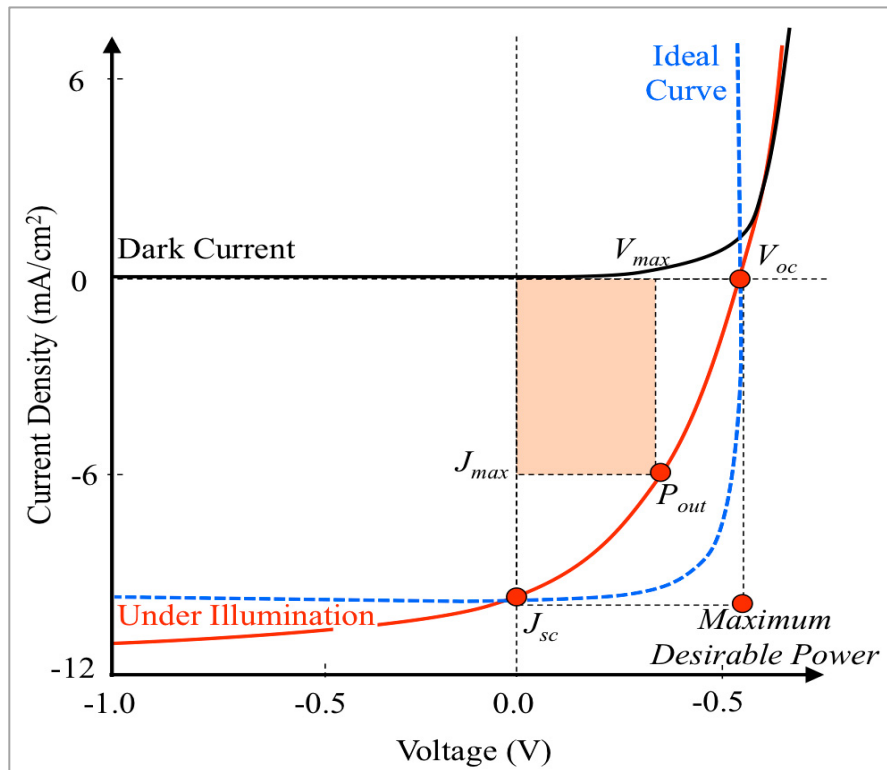


Figure 2. 15: Typical JV characteristic curves for solar cell in dark and under illumination conditions.

2.5.1 Open circuit voltage

The open circuit voltage is the forward bias of the pn junction due to the photocurrent. For BHJ-OSCs, the magnitude of V_{oc} is obtained from the difference between the acceptor LUMO_A and the donor HOMO_D levels, and would not exceed the difference between the work function of electrodes. By setting $I = 0$ in Eq. 2-1, the theoretical value of V_{oc} is:

$$V_{oc} = \frac{k_B T}{e} \ln \left(\frac{I_{ph}}{I_s} \right) \quad (2-3)$$

Experimentally, V_{oc} is given from the JV curve at zero current, and its value is ranging between $\sim 0.6-0.7$ V, which is usually less than the theoretical one due to the ohmic loss at the organic/electrode interface [11]. The large value of V_{oc} is required to facilitate the transition of electrons to the cathode.

2.5.2 Short circuit current

The short circuit current J_{sc} is the current of the device when the voltage is zero, and it is affected by the light intensity. Theoretically, the ideal I_{sc} is given by the product of the density of the photogenerated charge carrier in the OSC with its mobility:

$$I_{sc} = eN\mu E \quad (2-4)$$

where N is the density of the charge carriers, μ is their mobility, and E is the electric field [39]. For BHJ-OSCs, J_{sc} is in the range of 4-12 mA/cm². To absorb a large portion of the incident light, low bandgap materials are required.

2.5.3 Fill factor

The fill factor (FF) of solar cells pictures how much the JV curve is close to the maximum desirable shape of the power. It depends on the structure of the device, as well as the device's material. FF is given by:

$$FF = \frac{I_{max} V_{max}}{I_{sc} V_{oc}} \quad (2- 5)$$

The ideal value of the FF is unity. However, the typical value ranges from 70% to 85% for silicon solar cells [6,54], and 50-65% for organic ones [23,30].

2.5.4 Power conversion efficiency

The power conversion efficiency PCE of solar cell is the ratio between the maximum obtained power, P_{out} , to the incident power intensity P_{in} . The PCE is measured under the standard test conditions (STC); in which the P_{in} is 100 mW/cm², the spectral distribution of the light AM1.5G (Air Mass 1.5 global) at room temperature 25°C. The AM1.5G is defined as the global spectrum of the sunlight that passes through 1.5 thickness of the earth's atmosphere at an incident angle of 48.2° [32,39]. The PCE is given by:

$$PCE = \frac{P_{out}}{P_{in}} \times 100 = \frac{I_{max} V_{max}}{P_{in}} \times 100 = \frac{I_{sc} V_{oc} FF}{P_{in}} \times 100 \quad (2- 6)$$

The PCE is a function of the material properties, device structure, ambient conditions such as temperature, and the location of the cell with respect to the sun [6,54].

2.5.5 External quantum efficiency

The external quantum efficiency EQE, or sometimes referred as the incident photon-to-current efficiency (IPCE), is the ratio between the number of the charge carriers that are collected by electrodes to the number of the incident photon on the solar cell at a given wavelength [51]. Figure 2.16 illustrates the EQE curve in ideal and real Si-based solar cell. The EQE is calculated from the relation:

$$\begin{aligned} \text{EQE}(\lambda) &= \frac{\text{electrons/sec}}{\text{photons/sec}} = \frac{\text{current/charge of electron}}{\text{total power of photons/energy of one photon}} \\ &= \frac{I_{sc}/e}{P_{in}/(hc/\lambda)} \end{aligned} \quad (2-7)$$

Where h is the Planck's constant, c is the speed of light. Both I_{sc} and P_{in} are function of the wavelength λ .

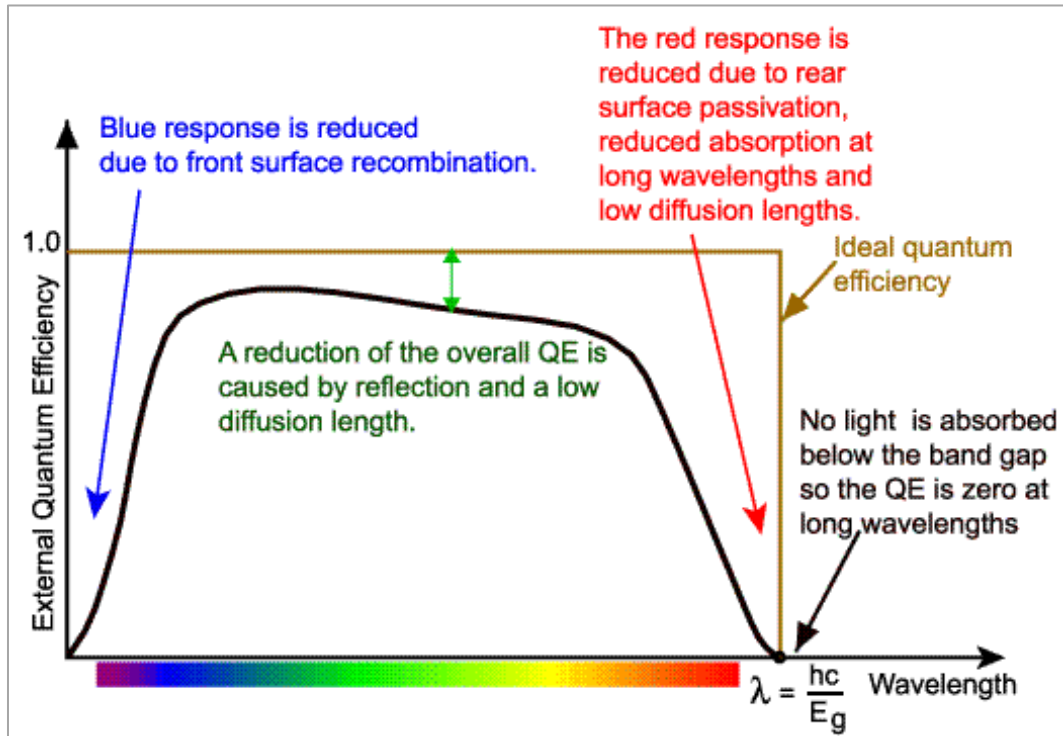


Figure 2. 16: Ideal and practical curves of the EQE for Si-based solar cell. The causes of the deviation from the ideal curve are noted [adapted from Ref. [55]].

2.5.6 Internal quantum efficiency

The internal quantum efficiency IQE for a solar cell is the ratio between the number of the charge carriers that is collected by electrodes to the number of the absorbed photons, not reflected or transmitted, by the photoactive layer. The formula for IQE is:

$$\text{IQE}(\lambda) = \frac{\text{EQE}(\lambda)}{1 - R(\lambda) - T(\lambda)} \quad (2- 8)$$

where $R(\lambda)$ and $T(\lambda)$ are the fraction of the reflected and transmitted light, respectively.

The maximum value of quantum efficiency is one or 100% [56].

2.6 Loss factors during the PV steps

As figure 2.16 indicates, not all of the incident solar radiation contributes to the photovoltaic effect. This is due to losses during photogeneration mechanism:

2.6.1 Optical loss

Interface reflection loss: which is the loss due to electromagnetic wave that is reflected from the air/glass/ITO/organic interface. For BHJ-OSC, the low reflection coefficient of organic materials, ~ 4%, limits this factor.

Un-absorbed photon loss: photon with energy less than energy gap is not absorbed. Such loss in energy is called a transmission loss.

Inappropriate thickness loss: with too thin photoactive layer, part of the incident radiations passes through the sample rather than gets absorbed. In contrast, if the

photoactive layer is too thick, the R_S increases, which reduces the exciton dissociation [51,57,58].

2.6.2 Nanostructure scale loss

Excitons have to reach the acceptor border within the exciton diffusion length to dissociate into free charges, otherwise the recombination occurs [51].

2.6.3 Electrical mechanism loss

After the free polarons are generated in both donor and acceptor materials, they are transported to the electrodes through the bulk organic materials. During the transition, charge carriers could be trapped for a finite time, which affects their mobility, or infinite time², in which they get lost and not contribute to the electrical current. At the organic/inorganic interfaces, however, surface state could play a role to pin Fermi level, resulting in trapping states for the charge carriers [51].

2.7 Challenges in organic solar cells

Theoretically, organic solar cell based on conjugated polymer should have power conversion efficiency similar to the Si-based one [15]. So far, however, the highest achieved efficiency of P3HT:PCBM BHJ solar cell is around 5% [19,20]. As it has been discussed previously, the low efficiency of polymer solar cells resulted from several

² By reaching an impurity such as an oxygen atom.

³ Retardation effect: the phase shifts of the electrodynamic field.

factors or challenges. The first challenge is the mismatch between the absorbance of the photoactive layer and the incident solar radiation. As figure 2.17 illustrates, the P3HT:PCBM blend has a very narrow absorbance band with respect to the AM1.5G solar spectra. Thus, a reasonable part of the infrared radiation will not get absorbed. Add to that, the inappropriate thickness of the thick/thin photoactive layer affects its absorptivity.

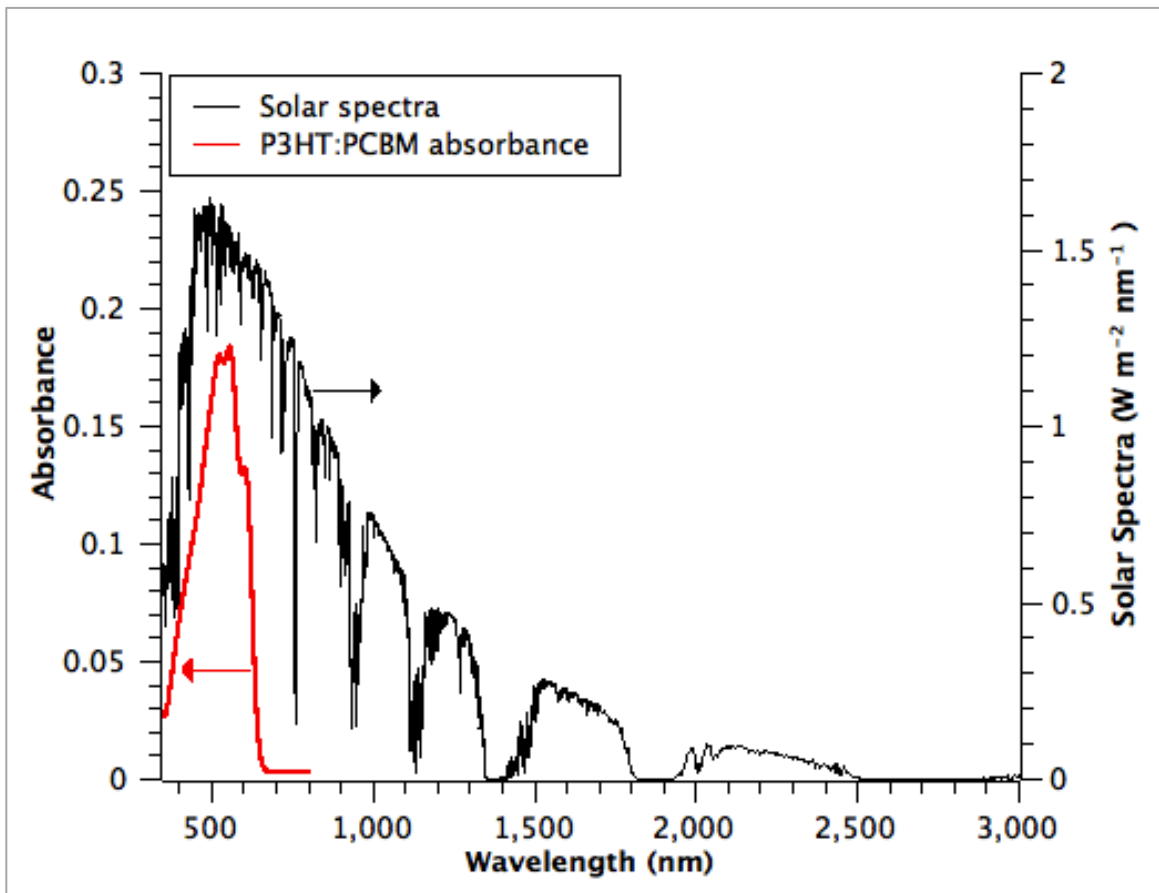


Figure 2. 17: A fraction of the absorbed light by ~100 nm thick P3HT:PCBM film deposited on ITO-coated glass along with the AM1.5 global spectra. The solar radiation data is obtained from Ref. [59].

As has been mentioned earlier, the effective thickness reported for the photoactive layer used in BHJ-OSCs is too thin (100-300 nm [14]) for a complete absorption of the

incident light, since part of the incident radiation will get transmitted. This promotes the use of thicker photoactive layers. However, enlarging the thickness of the photoactive layer is a critical point also, which results in another challenge related to the mobility of charge carriers. In polymer solar cells, the charge carriers mobility is around $\sim 10^{-2}$ - 10^{-4} $\text{cm}^2\text{V}^{-1}\text{sec}^{-1}$. This value is lowered by a factor of several hundreds as compared to the value of 10^4 $\text{cm}^2\text{V}^{-1}\text{sec}^{-1}$ for Si-based solar cells [15]. The low mobility factor results in an inefficient charge collection by electrodes due to the recombination of free charge carriers before reaching electrodes, which limits their numbers at the electrodes. This also results in the increasing of the device series resistance, which negatively affects the overall device performance.

Another challenge for organic solar cells is related to their instability in the ambient atmosphere. It is well known that the polymer solar cells materials are very sensitive to oxygen and water. In such condition, a rapid photo-oxidation/degradation on a polymer solar cell occurs as a function of humidity, and limits its lifetime to several hours [15,39].

The issue regarding the insufficient absorption of a thin film of photoactive layer would be dealt with increasing the absorption of the photoactive layer without increasing its thickness. This could be achieved by inserting metallic nanoparticles in OSCs layers, in which the localized surface plasmon resonance would play a role in increasing their absorption of light. In the following chapters, an overview of localized surface plasmon resonance in metallic nanoparticles, and hence the concept of plasmonic solar cell is presented.

CHAPTER III

Surface Plasmon Resonance in Metallic Nanoparticles

This chapter describes the origin of plasmonic studies in the context of propagated surface plasmon polaritons and localized ones. Theoretical considerations of the localized surface plasmon resonances in both isotropic and anisotropic sphere are presented. The chapter ended with the illustration of the optical properties of metallic nanoparticles and the parameters that influence such properties.

3.1 Plasma, plasmon, and surface plasmon

Free electrons in metals behave like a plasma wave, that is a wave of a longitudinal electromagnetic charge density. The quantized excitation of the plasma waves is called plasmon (quasiparticle-boson). Metals have a certain bulk plasmon frequency (ω_p) arising naturally from the long term coulombic interaction between negative electrons and positive ionic cores inside the metals. In SI unit, ω_p is given by:

$$\omega_p = \frac{Ne^2}{\epsilon_0 m} \quad (3-1)$$

where N is the charge density, e is the electronic charge, ϵ_0 is the space permittivity, and m is the electronic mass. The bulk plasmon frequency for metals lies either in the visible or the ultraviolet region of the spectra, i.e. $\hbar\omega_p$ ranges from 3 to 20 eV, which makes them shiny and reflective in the visible region [60].

The electromagnetic properties of metals are determined by their dielectric function ($\epsilon_m(\omega)$) that is negative, complex, and frequency dependent in nature:

$$\varepsilon_m(\omega) = \varepsilon'(\omega) + i\varepsilon''(\omega) \quad (3- 2)$$

The complex part, ε'' , of ε_m corresponds to the absorption in the metal [61,62]. The Drude-Sommerfeld model of free electron gas in metal gives the dielectric function of the metal, after neglecting the damping force, as:

$$\varepsilon_m(\omega) = 1 - \frac{\omega_p^2}{\omega^2} \quad (3- 3)$$

This implies that for illuminating metals with an incident light of frequency ω lower than ω_p , the ε_m is negative, which means that the refractive index, $n = \sqrt{\varepsilon_m}$, takes a purely imaginary value. The imaginary value of the refractive index means that the light cannot propagate in the metal, i.e. the plasma wave will screen it out. On the other hand, if $\omega > \omega_p$, the dielectric function ε_m is positive, which means that the incident light will get transmitted. The electrons (or plasma) response in this case is very slow; not fast enough to screen the light out. The plasma wave at the metal/dielectric interface is called surface plasmon, with plasmon frequency (energy) ω_{sp} lower than that of bulk material, $\omega_{sp} = \omega_p / \sqrt{2}$. The excitation of plasmons at the interface of two materials with opposite dielectric constants creates the surface plasmon polariton (SPP) [60,62,63].

3.2 Localized surface plasmon resonance

Noble metallic nanoparticles; e.g. gold and silver nanoparticles (NPs) react strongly with the incident light. The excitation of surface plasmon in such particles creates the particle plasmon or localized surface plasmon resonance (LSPR). While normal light cannot excite plasmon in a planar metal as the momentum of both surface

plasmon (SP) and photon has to be matched, the excited plasmon in MNPs is localized to the particle, and not characterized by a wave vector. Hence, the incident light is absorbed with no need for any geometry for momentum coupling. For such LSPR, the absorbed light has to have a specific wavelength called a plasmon band [64].

Figure 3.1 schematically shows the creation of surface plasmon resonance in a spherical MNP upon applying an electromagnetic (EM) field. The electric field (E) induces polarization in the conduction electrons with respect to the heavier positive core. Assuming that the positive charges are immobile, the conduction electrons oscillate under the influence of the applied field. As a consequence of the coherent oscillations of the conduction electrons, the electronic cloud gets displaced from the positive ionic core, giving a chance to a net charge difference at the nanoparticle boundaries, which results in a linear restoring force, coulombic attraction, that leads to the dipolar oscillations of the electronic cloud with respect to the positive ionic core. Such oscillation is known as surface plasmon resonance or oscillation. The term “surface” comes from the point that the restoring force that causes the resonance comes from the surface polarization. Hence, the surface of the MNPs plays a major role for observing the LSPR [64,65].

The localized mode of SP occurs when the frequency of the electric field of the incident light resonates with the oscillation of the free conduction electrons of MNPs. Consequently, the illuminated MNPs are excited and strongly absorb/scatter the incident light, producing a large enhancement, up to a factor of 100 [24], in the local electric field surrounding them [25]. The enhancement in the local field is given by the sum of the incident electric field and the one that is induced by SP in MNPs [35].

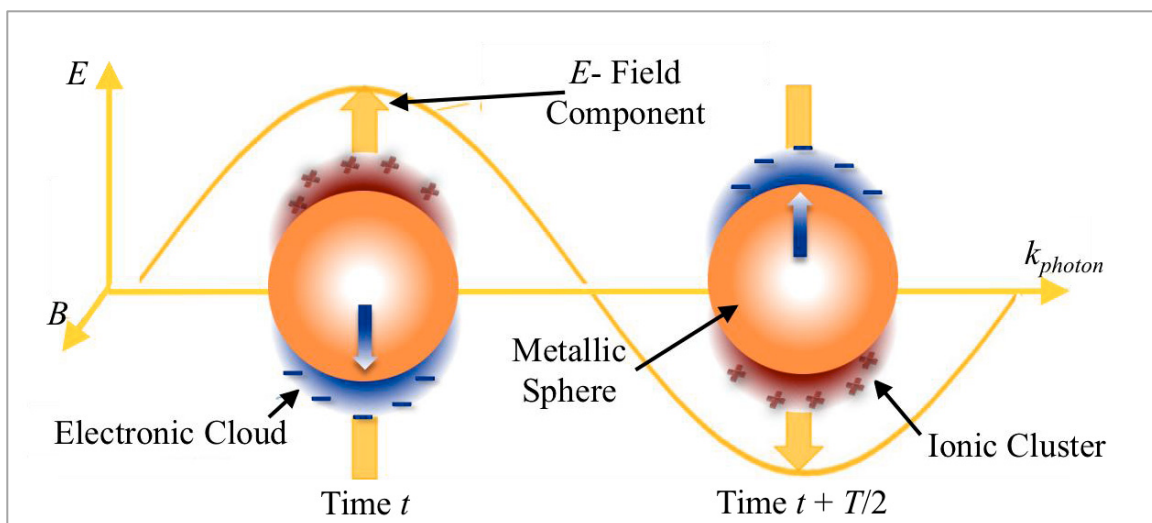


Figure 3. 1: Interaction of an EM field with metallic nanosphere creates SPR localized in MNP. The induced dipole oscillates in phase with the E -field of the incoming light [re-drawn from Refs. [64,66]].

A wide range of metallic nano-structures/particles supports the LSPR excitation mode. Metallic nanoparticles are easily synthesized using wet-chemical synthesis process, and are usually kept stable in the form of colloidal solutions. They can have any shapes; e.g. spheres, discs, rods, stars, cubes, rings... etc. as illustrated in figure 3.2. Since the resonance condition of MNPs occurs in optical frequencies, their colloidal solutions exhibit fascinating colors due to their interaction with the incident light. Figure 3.3 shows colloidal solutions of different shapes of MNPs [62].

In terms of synthesis, for example, reproducible Au NPs could be synthesized with a uniform diameter by the reduction of the Au using sodium citrate. This method produces negatively charged Au NPs, which makes them stable in the solution. Adjusting the concentration of the reagent controls the size of the particles. Yet, Au NPs could be aggregated by the addition of more salt or evaporating the solvent. In contrast,

synthesizing NPs using capping ligands stabilizes them and prevents the aggregation. The capping also makes the size-tuning possible, it also produces anisotropic particles [67].

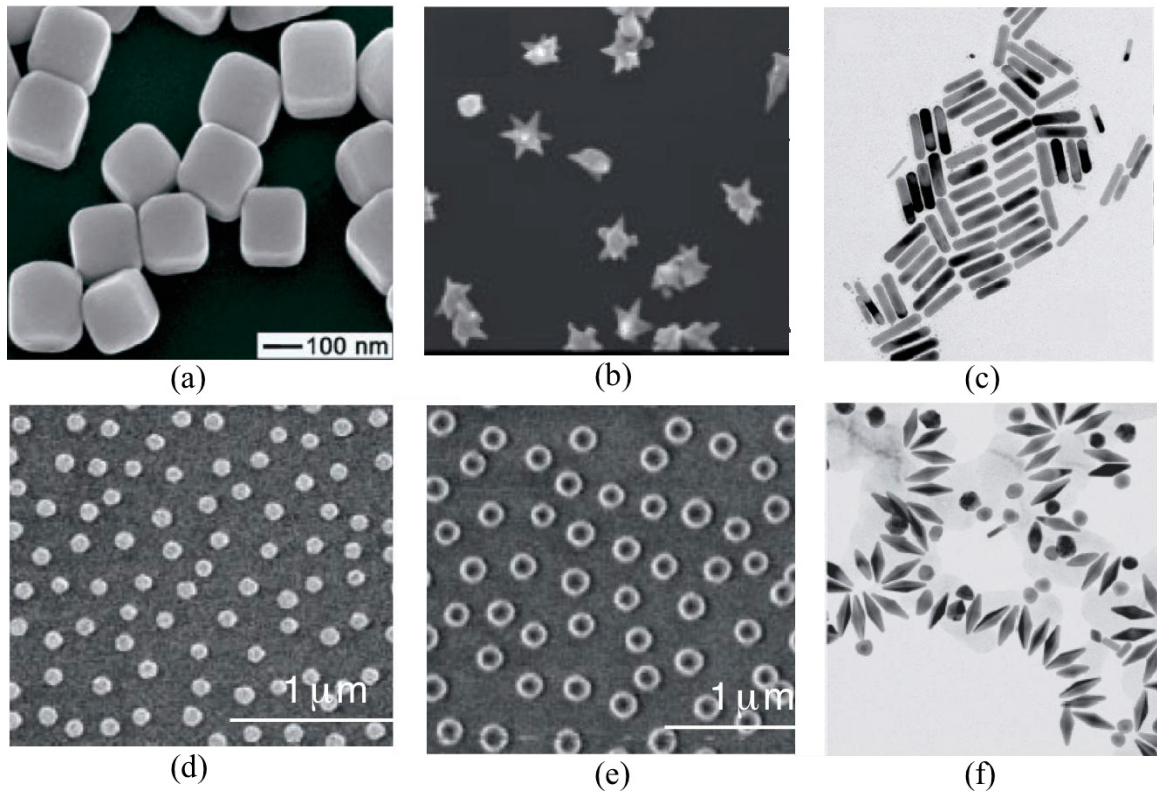


Figure 3. 2: Micrographs of different shapes of MNPs: (a) Ag nanocubes; (b) Au nanostars; (c) Au nanorods; (d) Au nanodiscs; (e) Au nanorings; and (f) Au nanobipyramids [adapted from Ref. [67]].



Figure 3. 3: Colloidal solutions of various shapes of MNPs [adapted from Ref. [68]].

3.3 Theoretical considerations of LSPR

When we treat the interaction of light with very tiny particles, ~ 50 nm in diameter, we deal with the quasi-static approximation, in which the incident light interacts with MNPs that have a diameter $2R$ (R denotes the radius) significantly much smaller than the wavelength of the applied light. In such case, the E field component of the incident light is considered uniform (constant) for the entire particle; i.e. the retardation effect³ is neglected. Thus, the interaction of light with the particle is treated using electrostatics rather than electrodynamics, and both ϵ_d and ϵ_m are given using electrostatic theories [64].

³ Retardation effect: the phase shifts of the electrodynamic field.

3.3.1 Extinction of the incident light

As aforementioned above, MNP is a good scatterer and absorber of the incident light at wavelength near the plasmon resonance. The scattering is a result of the re-radiation of the incident E field in all direction by the accelerated charges after the charges being radiated by an EM field at the resonance frequency. In contrast, the absorption occurs if part of the incident radiations is not re-radiated but stored in the particle (as a non-radiative near field effect) or transferred to thermal energy. By placing a detector in the path of an electromagnetic beam downstream from a particle, the detector then receives the transmitted energy. If the transmitted energy is less than the incident one, we say that the particle causes an extinction of the incident energy. This extinction is the sum of both absorption and scattering. The extinction coefficient (C_{ext}) is determined by the ratio between the transmitted (I_t) and incident (I_i) radiation as:

$$\frac{I_t}{I_i} = \exp(-C_{ext}NI) \quad (3-4)$$

where l is the travelling distance through a medium and N is the particles' density. Although scattering and absorption are not independent processes as they occur simultaneously, one of them has a chance to be dominant [60]. Figure 2.4 presents scattering, absorption, and extinction for a spherical particle.

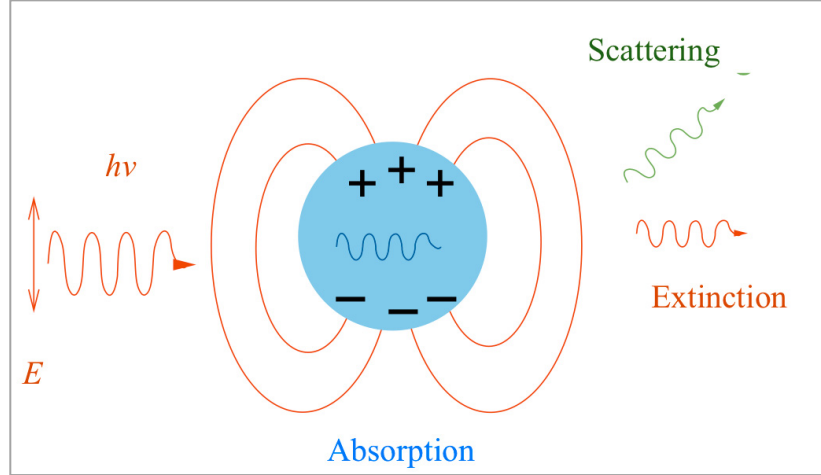


Figure 3. 4: Scattering, absorption, and extinction for a spherical particle [adapted from Ref. [67]].

In quasi-static approximation, the scattering and absorption cross section, (C_{sca}) and (C_{abs}), respectively, for irradiated MNP is given by:

$$C_{sca} = \frac{1}{6\pi} \left(\frac{2\pi}{\lambda} \right)^4 |\alpha|^2 \quad (3-5)$$

$$C_{abs} = \frac{2\pi}{\lambda} \text{Im}[\alpha] \quad (3-6)$$

since

$$\alpha = 3U \left[\frac{\varepsilon_m - \varepsilon_d}{\varepsilon_m + 2\varepsilon_d} \right] \quad (3-7)$$

where α is the static polarizability of the MNP that is given by solving Laplace's equation, U is the volume of the MNP, $\varepsilon_m = \varepsilon' + i\varepsilon''$ and ε_d are the dielectric function for MNP and the hosted medium, respectively. It is clear from the above equations that the optical properties of SPR depend on the shape and size (on the volume U) of the MNPs as well as the surrounding medium. From Eq.3-7, the strongest response of the MNP happens when the particle polarizability α becomes very large, which occurs if the

denominator becomes closest to zero. This is the LSPR condition ($|\varepsilon_m + 2\varepsilon_d| = 0 \Rightarrow \varepsilon_m = -2\varepsilon_d$), and is achieved when $\varepsilon'(w) = -2\varepsilon_d$ and $\varepsilon''(w) \ll 1$. By applying Eq.3-3 to Eq. 3-7 at low damping and low interband transition conditions, the resonance condition for MNP in air ($\varepsilon_d = 1$) is given by [67,69]:

$$w_{SP} = w_p / \sqrt{3} \quad (3- 8)$$

The plasmon frequency w_{SP} given by the Drude model is not precise for most of metals due to the interband transitions between the d and s orbitals, which produce an additional electronic excitation (susceptibility) at optical frequencies. The produced electronic excitation couples with the response of the free electrons, resulting in a large change in both $\varepsilon'(w)$ and $\varepsilon''(w)$. It also causes a significant relaxation in the plasmon decay, which affects its optical response. For example, in the Ag case, the Drude value is $w_{Drude} = 5.6$ eV which is different than the experimental one, $w_{SP} = 3.6$ eV. Furthermore, the free electron model cannot be applied to Au and Cu metals since the $\varepsilon''(w)$ is not negligible at the optical frequencies [70].

3.3.2 Isotropic sphere: Mie theory

Mie applied Maxwell's equations to describe the light extinction for small MNPs. He found a general solution for a diffraction problem of a single sphere in spherical coordinates. Under the condition of the quasi-static approximation, Mie assumed that both particle and its surrounding medium are homogeneous and can be described by their bulk optical dielectric functions. In addition, at the quasi-static limit only the electric

dipole term contributes to the extinction cross section. Thus the extinction cross section for a spherical particle is reduced to:

$$C_{ext} = \frac{9w\epsilon_d^{3/2}}{c} U \left| \frac{\epsilon''(w)}{[\epsilon'(w) + 2\epsilon_d(w)]^2 + \epsilon''^2} \right| \quad (3-9)$$

The resonance condition is applied when $\epsilon'(w) = -2\epsilon_d$, and ϵ'' is very small or weakly dependent on w . The above equations succeeded to give the extinction for small spherical MNPs, ~ 50 nm, where the scattering is significant. Since the dipole resonance depends on the size of the particle, the dipole approximation is no longer valid for larger particles [64]. For very small particle, $\sim 5-10$ nm, the dielectric function $\epsilon_m(w)$ changes, and hence the optical properties. This point will be further explained in section 3.4.4. Equation 3-9 also shows that there is no absorption when $\epsilon''=0$ and $\epsilon''=\infty$. The former case is for non-absorbing particle, while the latter one corresponds to the reflection of all the incident radiation [71].

3.3.2 Anisotropic sphere: Gans formula

When the shape of the particles deviates from the spherical shape, the optical properties of the MNPs are no longer given by Mie formula. This is due to the non-equivalent resonance components that are produced from the longitudinal and transverse dipolar polarizability. Gans modified Mie formula for ellipsoidal gold nanoparticles to have the axes-polarizability dependent ($\alpha_{x,y,z}$) as: [64,71]

$$\alpha_{x,y,z} = \frac{4\pi abc(\epsilon_m - \epsilon_d)}{3\epsilon_m + L_{x,y,z}(\epsilon_m - \epsilon_d)} \quad (3-10)$$

where a , b , and c are the ellipse lengths along x , y , and z axes, $a > b = c$, and $L_{x,y,z}$ is a depolarization factor for the corresponding axis [71].

3.4 Optical properties of metallic nanoparticles

The interesting optical properties of MNPs arise from the large ratio of their surface area with respect to their volume. This characteristic makes the optical properties of MNPs different from the usual bulk ones [35]. For instance, the bulk gold exhibits the familiar yellowish color. Yet, its color tends to change gradually by subdividing it into nano-size dimension, until it becomes ruby red, figure 3.5 [64].

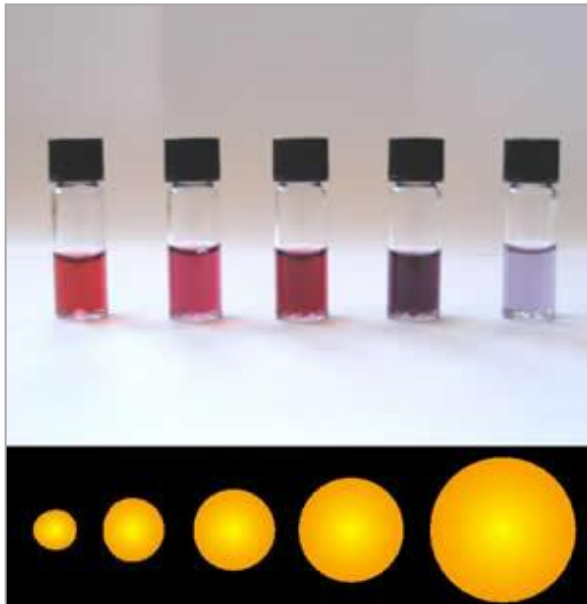


Figure 3. 5: Changing the color of the gold colloidal solution by reducing the particles diameter [adapted from Ref. [72]].

The absorption spectra of colloidal solutions of MNPs with dimensions less than the incident wavelength are characterized with a broad and intense peak in the visible region of the spectra, which causes their unique colors [66]. The spectral measurements

of Au NPs colloidal solution, figure 3.6, reveal that their ruby red color is due to their absorption of the green light at 520 nm [64].

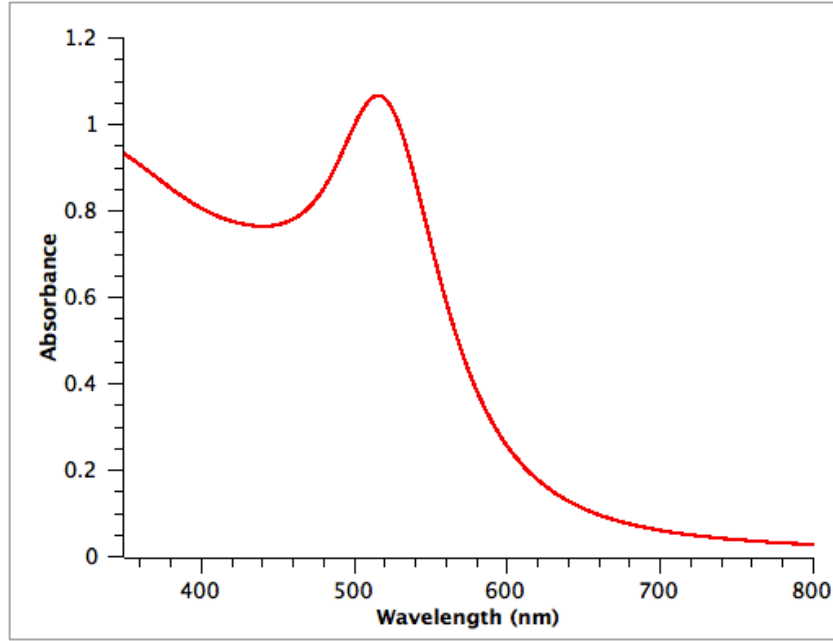


Figure 3. 6: The absorption spectra of 5 nm Au NPs synthesized in our lab.

The spectrophotometer measures the attenuation in the intensity of the incident light I_o , which occurs after the light passes through a colloidal solution of MNPs with a density N , in which the optical path length l is in cm unit. The rate $dI(l)/dl$ is the attenuation rate (the loss of photon), and is given by [71]:

$$\frac{dI(l)}{dl} = -NC_{ext}I(l) \quad (3- 11)$$

Integration of Eq.3-11 gives the UV-Vis absorption spectra, A , for a diluted homogenous MNPs solution in a typical experimental set up as:

$$A = \log_{10} \frac{I_o}{I(l)} = \frac{NC_{abs}l}{\ln 10} = \frac{NC_{abs}l}{2.303} \quad (3- 12)$$

since both I_o and $I(l)$ have the same unit, the absorption A is a unit-less quantity.

As has been stated previously, the peak position, height, shape, and bandwidth of MNPs spectra could be tuned by changing the particle's size and shape as well as the dielectric function of the surrounding environment [66]. Some details regarding the factors that affect the optical response of the MNPs are as follows:

3.4.1 Frequency of the incident light

The dielectric function (or refractive index) of metals $\epsilon_m(\omega) = n^2$ is a frequency or wavelength dependent quantity. From Eq. 3-7, the strongest response of the MNPs with the incident light happens when the denominator is zero, which corresponds to $\epsilon_m(\omega) = -2\epsilon_d$. Thus, the optical properties of MNPs are governed by the frequency of the incident light that satisfies the resonance condition [62].

3.4.2 Local dielectric function

It is clear from the resonance condition $\epsilon_m(\omega) = -2\epsilon_d$ that the optical response of MNPs is influenced as well by the local dielectric function ϵ_d of the surrounding medium. The change in the ϵ_d results in a change in the ϵ_m at which the resonance occurs. For instance, the relative permittivity of a glass in the visible region is $(1.5)^2 = 2.25$. This implies that the resonance occurs at $\epsilon_m = -2 \times 2.25 = -4.5$. Therefore, the resonance happens at the visible (520 nm) and violet (420 nm) for Au and Ag NPs, respectively [62]. It has been reported that the resonance peak of spherical MNPs is red shifted as the dielectric constant of the surrounding medium increased [73].

3.4.3 Anisotropic effect

The optical responses of MNPs are also remarkably sensitive to the shape and geometry of the particles. In case of completely symmetrical particles, as in nanospheres, there is only one dipolar plasmon resonance. However, by elongating a spherical particle in one dimension, as in nanorods, a second dipolar resonance band in the longitudinal direction is possibly formed. For more complex shapes, the optical absorption becomes even more complex since more non-degenerated dipolar modes arise. In addition, for less symmetrical particles, higher multipolar charge distributions exist. The locations of the higher multipolar surface plasmon resonances are always at the longer wavelengths with respect to the dipolar ones (red-shifted) [65]. Figure 3.7 shows the extinction efficiency of various shapes of silver nanoparticles.

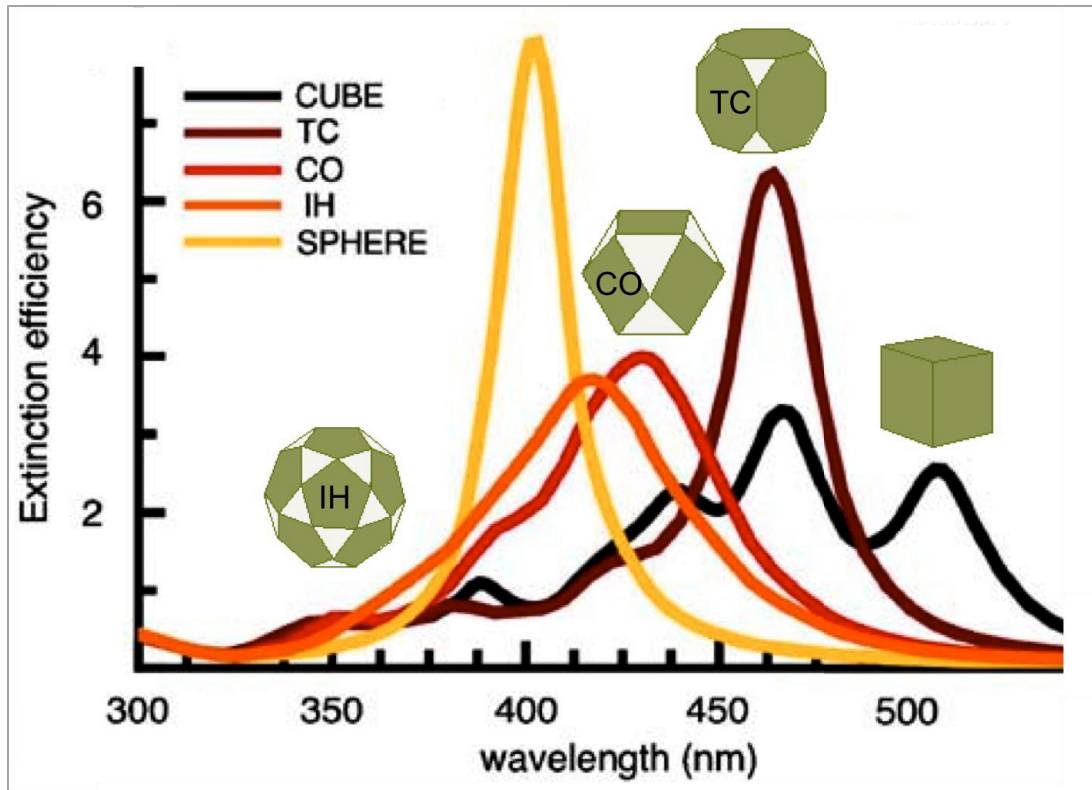


Figure 3. 7: Extinction efficiency of silver nanoparticles with various shapes: cube , truncated cube (TC), cuboctahedron (CO), icosahedron (IH), and sphere [adapted from Ref. [65]].

3.4.4 Size effect

At nano-sized regime, the ratio of particle radius to the incident wavelength becomes very important, and the optical functions become size-dependent. For very small particles, < 10 nm, the diameter of the particles becomes comparable or less than the mean free path of the electron. This results in electrons collisions with the surface of the nanoparticles. Therefore, the effective mean free path of electrons decreases linearly with the diameter to a value lower than that in the bulk materials. Hence, the metal dielectric function changes from the bulk dielectric function. This affects the plasmon resonance band to be broadened as illustrated in figure 3.8 [65,70].

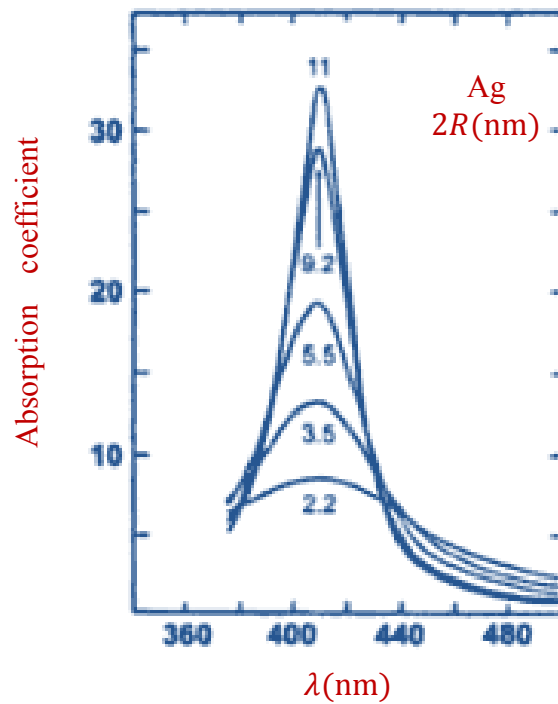


Figure 3. 8: Size confinement effects on the plasmon resonance band for Ag nanoparticles [adapted from Ref. [70]].

For particles of sizes $\sim 2R < 30$ nm, the excitation of the conduction electrons occurs in-phase with the incident EM radiation, resulting in a dipolar oscillation. Hence, the scattering becomes negligible and the absorption will be the dominant contributor to the extinction cross section. As the nanoparticles size increases, the amount of the absorption and scattering increases too, and scattering becomes dominant (for 100 nm diameter or larger). In addition, light cannot polarize large particles homogeneously; i.e. the field across the particle is not uniform (the retardation effect becomes significant), which makes the higher order dipolar modes important. This results in more than one peak in the LSPR spectra. In addition, the peaks appear broadened, less intense, and red-shifted.

As the size of the particles becomes larger and larger, a split in the energy levels is reduced until they merge into the quasi-continuous band structure for bulk solid. Figure 3.9 shows the extinction properties of spherical Au NPs in water calculated as a function of diameter [35,64,65,70].

Since MNPs are good scatterer and absorber of the incident light, they have been used in many optical applications, including sensors and PV devices. In the following chapter, we will present the possibility of using plasmonic structure to trap the incident light in thin film solar cells as a way to enhance the power conversion efficiency of such cells.

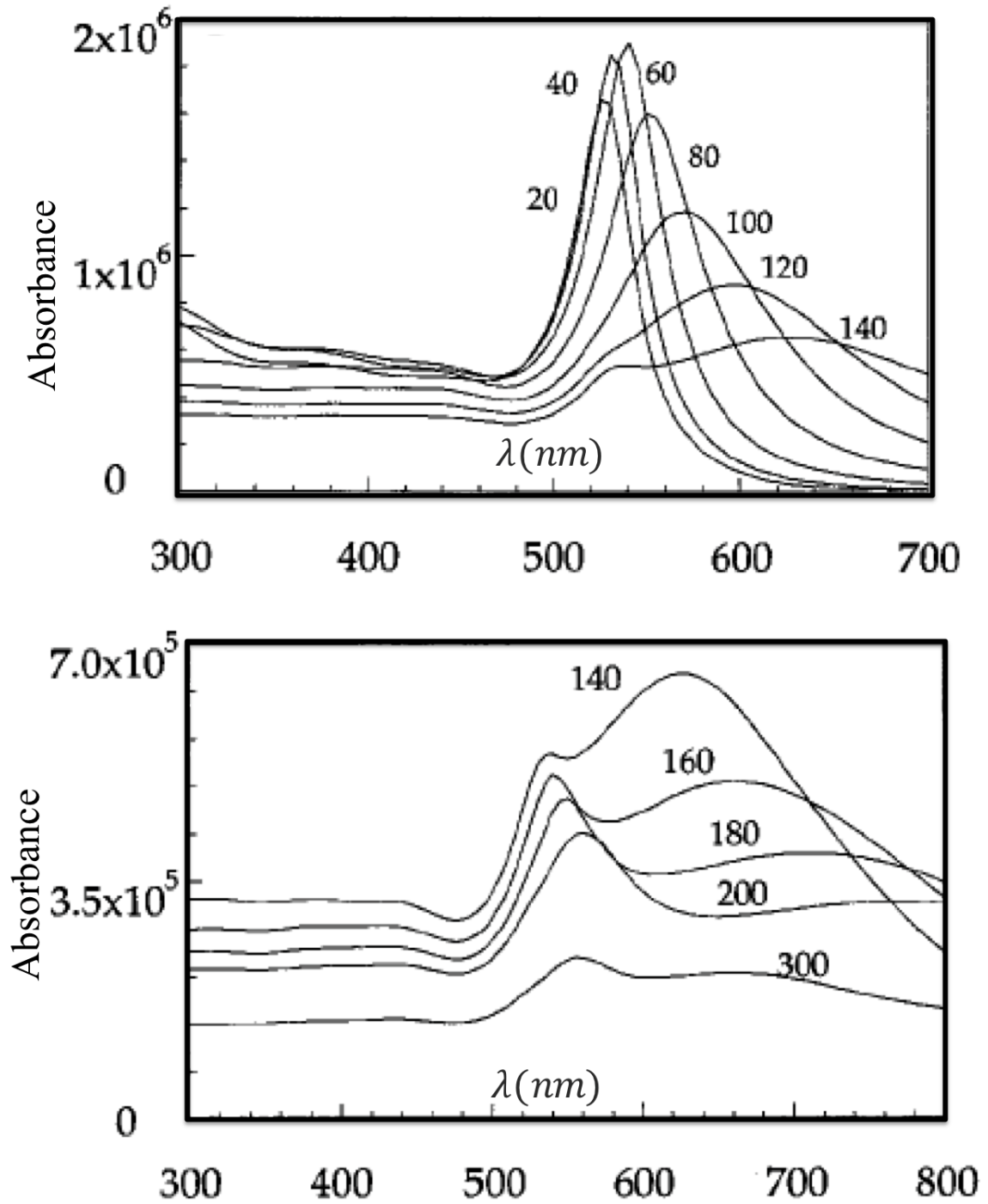


Figure 3. 9: Absorption bands of Au NPs in water, calculated as a function of diameter. The numbers indicates $2R$. As we see, with increasing the particle size, various extinction peaks appear, and then peaks fade away until the bulk optical properties of metals remain [adapted from Ref. [74]].

CHAPTER IV

Plasmonic Solar Cells

This chapter presents the idea of plasmonic solar cells by highlighting some possible approaches that help in trapping light inside thin film solar cells using plasmonic structures, in which the dwell time of the incident light inside the absorber is increased. Then, our objective to increase the absorption of a constant thickness of polymer:fullerene solar cells is illustrated. The chapter ended with the properties of gold nanorods, and the motivation behind their use in the current work.

4.1 Light trapping approaches inside a thin absorber

It is clear from figure 2.17 that a large fraction of solar radiation is not absorbable using a thin film, ~ 100 nm, of the P3HT:PCBM photoactive layer. A thin photoactive absorber layer is not only required for polymer solar cell, it is also a strong demand for all kinds of solar cells to overcome the charge carriers recombination issue. However, when a thin photoactive layer is used, the optical path length l of the applied light inside the photoactive layer has to be enlarged to reduce the loss in the absorbance of the incident radiation. The optical path length could be increased by the light trapping mechanism using pyramid surface texturing as illustrated in figure 4.1 [56]. Yet, such approach is not applicable for thin film absorber technologies since the absorber thickness is much smaller than the pyramids surface texture that is in the range of 10 microns [75]. In addition, such pyramid geometry has larger surface area, which would increase the recombination of the minority carriers at the texture/junction interface [9,26].

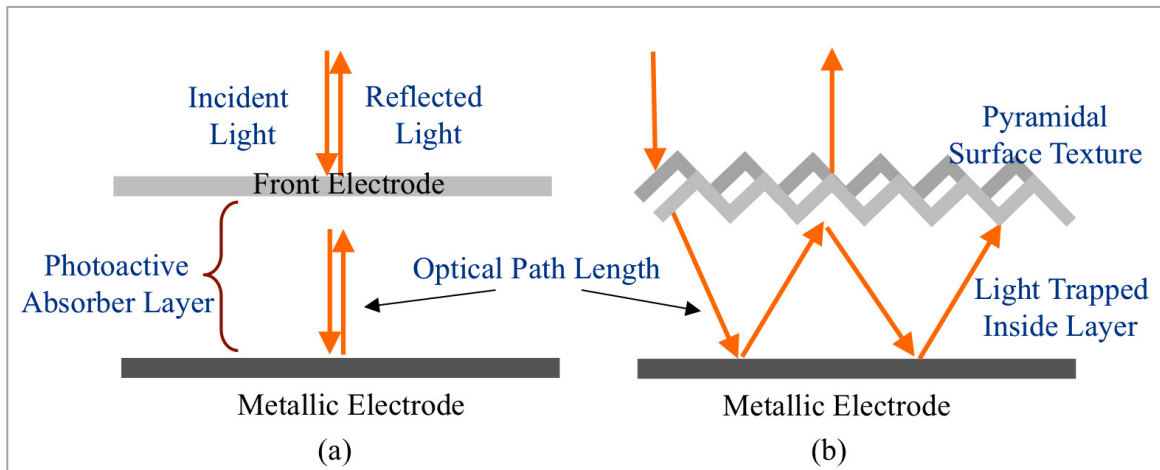


Figure 4. 1: (a) A schematic presentation for the optical path length of the incident light through a thin absorber layer; (b) Increasing of the optical path length inside the absorber by using light trapping pyramidal surface texture.

For thin film technologies, it is applicable to utilize the light trapping phenomenon associated with the excited MNPs after being illuminated. As figure 4.2 illustrates, metallic nanoparticles could improve light trapping and hence increase the light absorption for a constant-thickness absorber film by three possible approaches: far field effect (scattering using the particle plasmon), near field effect (absorption using the particle plasmon), and by coupling of the incident light to the SPP mode at semiconductor/metal interface [26].

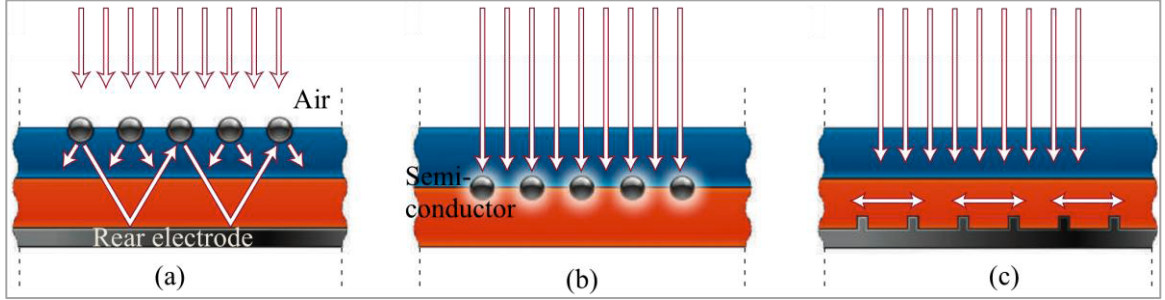


Figure 4. 2: Three ways to increase the light absorption of a constant thin film absorber using light trapping of MNPs via: (a) Scattering plasmon; (b) Absorbing plasmon; and (c) Plasmon polariton at semiconductor/metal interface [adapted from Ref. [9]].

4.1.1 Light trapping using plasmonic scatterers

The far field effect (or scattering) that is associated with MNPs is a good approach for enhancing the absorption of a thin absorber film. The scattering efficiency (Q_{sct}) for small MNPs is given by:

$$Q_{sca} = \frac{C_{sca}}{C_{sca} + C_{abs}} \quad (4- 1)$$

At resonance frequency, the scattering and absorption cross sections, C_{sca} and C_{abs} , of MNPs are much larger than their geometric cross section. For example, 100 nm Ag particles have C_{sct} that is ten times more than their geometric cross section [26]. Hence, covering $\sim 10\%$ of the solar-cell body with such particles would be sufficient to couple most of the incident light into excited plasmons [9].

When small MNPs are placed at the interface between two materials with different permittivity, the forward scattering toward a larger permittivity medium becomes favorable. By considering figure 4.2a in which the absorber film has larger

permittivity than air, the scattered light will acquire an angle rather than being normal, which increases its optical path length inside the absorber, resulting in an increase of its absorption of the incident light. In the case of having a reflected metallic rear electrode, the scattered light is trapped inside the absorber. Hence, it gets coupled with the MNPs and re-scattered again [9,26]. It is also reported that MNPs deposited on the front electrode could act as an antireflection coating in the visible region, since more light is scattered at the higher refractive index medium rather than being reflected back into the air, which is the function of the antireflection coating [75].

Trapping of the incident light inside an absorber using scatterer MNPs is influenced very much by the MNPs sizes and shapes. It has been reported that cylindrical and ellipsoid Ag MNPs scatter more light into the substrate as compared with particles with spherical shape. This is illustrated in figure 4.3a. As a consequence, the optical path length of the incident light inside the absorber is enhanced by 30-fold by using ellipsoid particles, figure 4.3b [69].

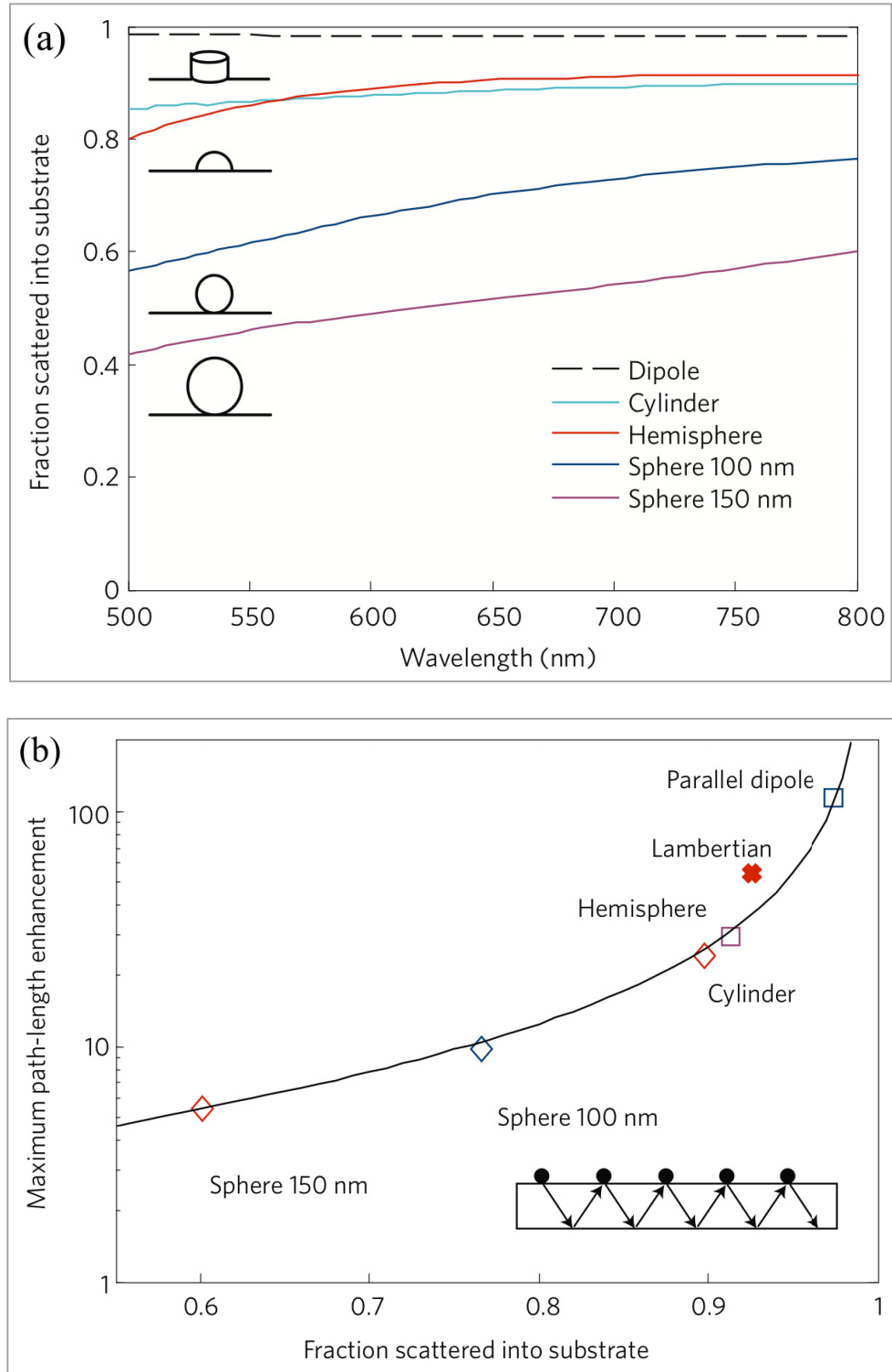


Figure 4.3: The fraction of light that is scattered to a semiconductor is very sensitive to the shape of MNPs. (a) Ag MNPs of cylindrical or hemisphere shape scatter the incident light more than the spherical one; (b) The optical path length inside the absorber is increased more using the hemisphere particle as compared to the spherical one [adapted from Ref. [69]]

4.1.2 Light trapping via absorbing plasmon

Besides the scattering plasmon approach, the near field effect surrounding the tiny excited MNPs could be used to enhance the absorption of a thin photoactive film. In such case, MNPs act as an antenna or a concentrator lens that intensifies and stores the incident light in the form of LSPR [9]. The conventional way for concentrating light or enlarging the intensity of the local electric field is with the use of dielectric lenses. However, Bragg's law of diffraction⁴ reveals that the dielectric lenses are not capable to focus the incident light (of wavelength λ) to a spot that is less than $\sim \lambda/2$. This in fact raises the importance of using MNPs as a light concentrator in thin film applications over their dielectric counterpart [73]. At the resonance frequency, the LSPR in MNPs allows for intensifying the incident electric field many orders of magnitude, and localizing it to a few tens of nanometer surrounding the particles [26]. Figure 4.4 shows that the near field enhancement around gold nanorod (of dimensions 27 nm \times 77 nm) is extended to ~ 40 nm in the surrounding area [76].

The near field effect around MNPs is mostly supported by tiny particles, ~ 5 - 40 nm, in which the absorption is dominant. If such particles are placed near to or embedded in a semiconductor, as in figure 4.2b, the number of the generated electron-hole pairs inside the photoactive layer will increase as a consequence of increasing the film absorption of the incident light, which in turn enlarges the photogenerated current in the cell. Since the absorption rate of organic semiconductor is higher than the plasmon decay time, light trapping using such approach is applicable for OSCs [9].

⁴ $2d\sin\theta = n\lambda$, where d is the inter-plane distance, n is integer representing the order of the diffraction peak, and θ is the scattering angle.

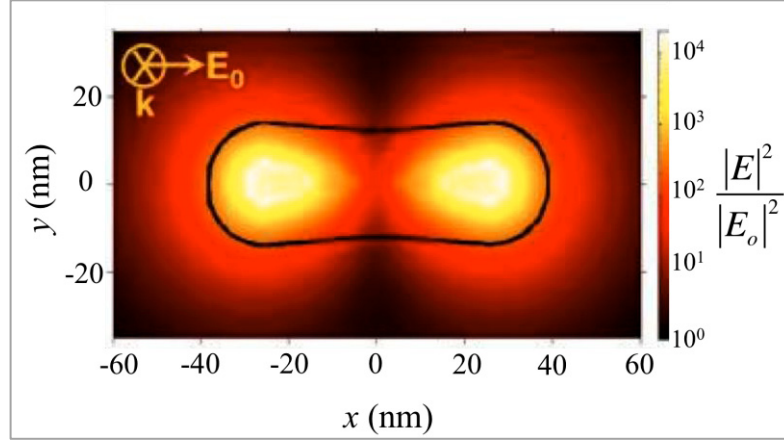


Figure 4. 4: Calculation of the near field enhancement around Au nanorod on Si substrate using the Discrete Dipole Approximation method. The value $|E|^2$ is the enhancement in the local electric field. The position of the rod is indicated by the black line [adapted from Ref. [76]].

4.1.3 Light trapping inside a thin absorber film via plasmon polaritons

The third way to improve the light absorption of a thin film is by taking the advantage of SPP. Surface plasmon polariton is a coupling between plasmon and photon, which results in the excitation of surface plasmons at the interface between two materials with opposite permittivities; i.e. metal/semiconductor interface. In SPP, the strength of the E field component of the incident light drops exponentially with a distance from the surface, leading to confining the plasmon (evanescent wave) to the surface at dimensions much smaller than the incident wavelength. The inset of figure 4.6 pictures such confinement. The evanescent wave will then propagate into the low reflective index medium, i.e. metal, until it decays as an absorption in the metal [60,63]. The momentum $\hbar k_{SP}$ of SPP is obtained from solving Maxwell's equations as:

$$\hbar k_{SP} = \hbar k_{photon} \sqrt{\frac{\epsilon_m \epsilon_d}{\epsilon_m + \epsilon_d}} \quad (4- 2)$$

where k_{SP} is the wave vector of the SP, and $k_{photon} = \omega/c$ is the wave vector of the incident light. It is clear from Eq. 4-2 that the momentum of the SPP is greater than the one of the free photon at the same frequency. Hence, normal light cannot give the right frequency and momentum to simultaneously excite surface plasmons [61,62,63]. To excite SPP, the momentum of the incident light has to be enhanced to match the one for SPP. This could be done by reaching the attenuated total reflection (ATR) condition using certain geometry such as a prism as in figure 4.5 [61].

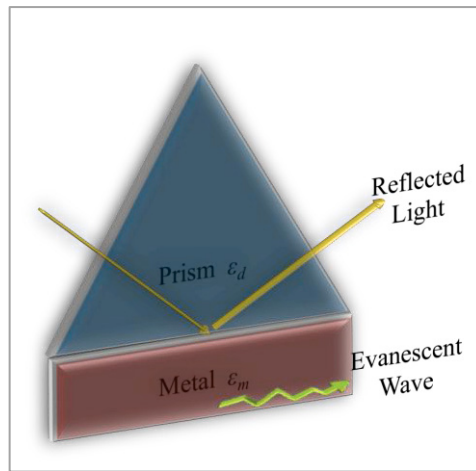


Figure 4. 5: Using a prism to couple the momentum of photon with SP. The prism is placed against a thin metal film in which the metal is the evanescent tunneling barrier.

It is not suitable to use such prism geometry to excite SPP in thin film applications. Alternatively, a chain of MNPs those are deposited near each other on the metallic rear electrode of thin film solar cells, figure 4.2c, could support the SPP mode. In such case, the LSPR for each particle will couple to the adjacent one near to it, and propagate from one particle to another along the metallic electrode [77]. Hence, the incident light is absorbed along the lateral direction of the solar cell, giving a chance of

increasing the optical path length inside the absorber. It has been reported that the excited SPP at metal/semiconductor interface of solar cell successfully traps the incident light inside the semiconductor film. As it is depicted in figure 4.6, the absorbed light inside a semiconductor that is in contact with Ag or Al is influenced by both metal and dielectric material [9].

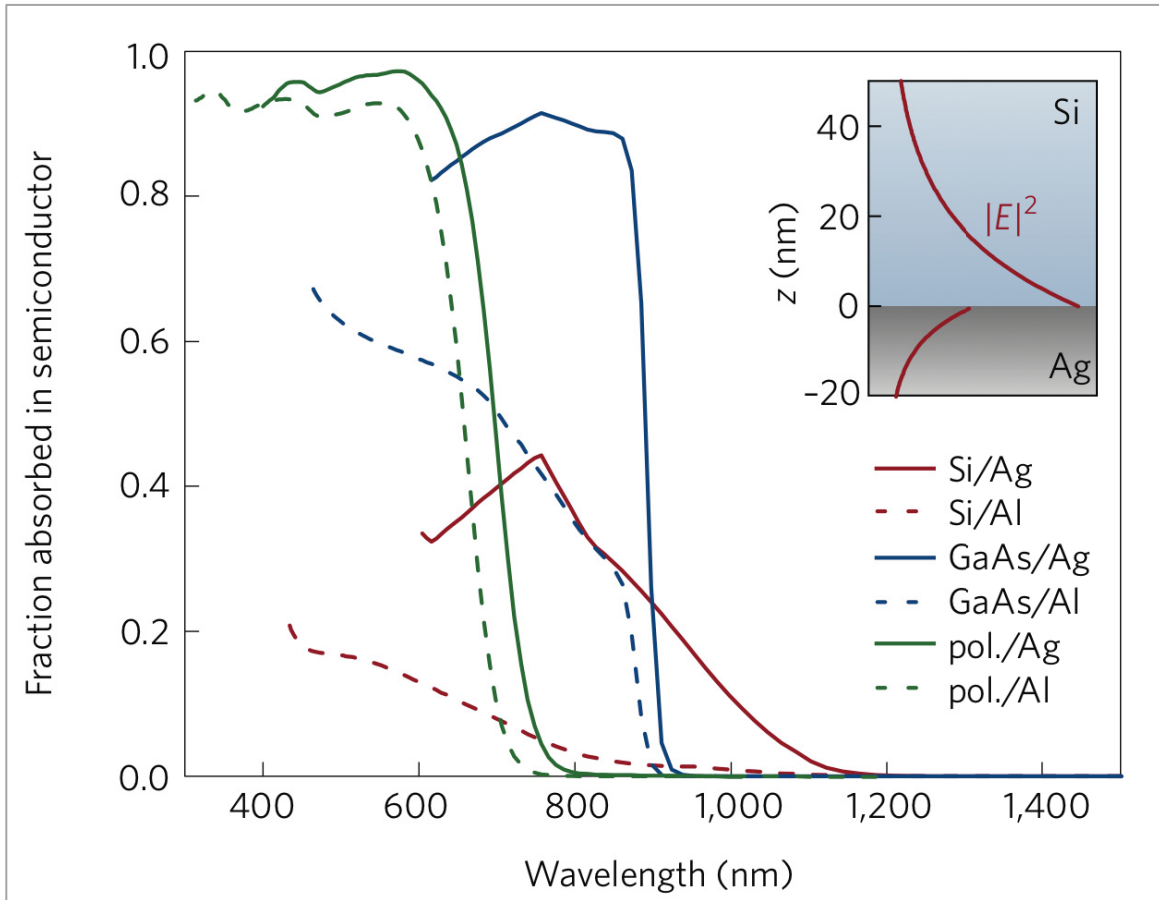


Figure 4. 6: The fraction of the absorbed light inside different semiconductors (Si, GaAs, and PF10TBT:PCBM-termed as pol.) by exciting of the SPP at semiconductor/Al or Ag interface. The inset shows the confined evanescent wave near the Si/Ag interface [adapted from Ref. [9]].

4.2 Plasmonic in polymer solar cell, a literature review

A study done by Kim et. al. (2008) showed that silver nanoparticles with diameter ~ 13 nm on the top of ITO-coated glass enhanced the PCE of the organic solar cell by 20% [29]. Another study done by J. H. Lee et. al. (2009) showed that by depositing many layers of 30 nm gold nanodots on ITO-coated glass substrate, the PCE of the resulting device was improved by 20% [30].

A Study done by F.C. Chen and his coworkers (2009) showed that when a 20% of gold nanoparticle colloidal solution, ~ 30 -40 nm, was blended with PEDOT:PSS solution, the solar cell efficiency enhanced by 20% [31]. Woo-Jun Yoon et. al. (2009) deposited silver nanoparticles (~ 4 nm diameter) on the top of PEDOT:PSS buffer layer before spin-coating the polymer photoactive layer. The short circuit current of the resulting device was increased by 12% [23].

D. H. Wang et. al. (2011) mixed 5% of gold nanoparticles, ~ 70 nm, colloidal solution with the photoactive layer solution. The resulting device shows an enhancement in the PCE by 23% [33]. Chen X. and his group (2008) showed that when gold nano layer was thermally evaporated on the P3HT:PCBM blend before depositing the LiF/Al electrode, the PCE of the device was improved by 30% as compared with a device only having LiF/Al electrode [34].

4.3 Our objective

Our objective from the current study is to enhance the PCE of P3HT:PCBM bulk heterojunction solar cell by incorporating gold nanorods into different locations in the cells. We expect to increase the light absorption of a constant film of P3HT:PCBM by

inserting such MNPs. We used gold nanorods that have 40 and 10 nm long and short axes diameters, respectively. Up to our knowledge, there were no previous studies on the effect of incorporating gold nanorods into BHJ-OSC layers. Besides, the rod shape of Au nanoparticle has a broad absorbance band that is located near the absorption profile of the P3HT:PCBM photoactive layer, which motivates the use such particles in the present work. Another important point is the small volume of rods, which is good for keeping the flat morphology of our device layers away from disturbance. According to an analytical reported study [69], using cylindrical particles in solar cells is favored than spherical one, since the possibility of having higher fraction of the forward-scattered light is increased as compared to using the particles with spherical shape. The optical properties of gold nanorods are very interesting subject to be illustrated:

4.4 Gold nanorods properties

As has been stated in chapter three, the optical response of MNPs can be tuned easily by changing their morphology. One of the simplest geometries that have optical response over a broad spectral range is the nanorods (NRs) shape, which occurs by elongating the spherical particle along one axis. The optical response of gold nanorods is one of the hottest topics that have been studied widely [35,64,67,71,78]. The colloidal solutions of gold nanorods with different aspect ratios (defined as the ratio of the rod's long axis to the short one) exhibit different colors, i.e. optical response, as in figure 4.7.

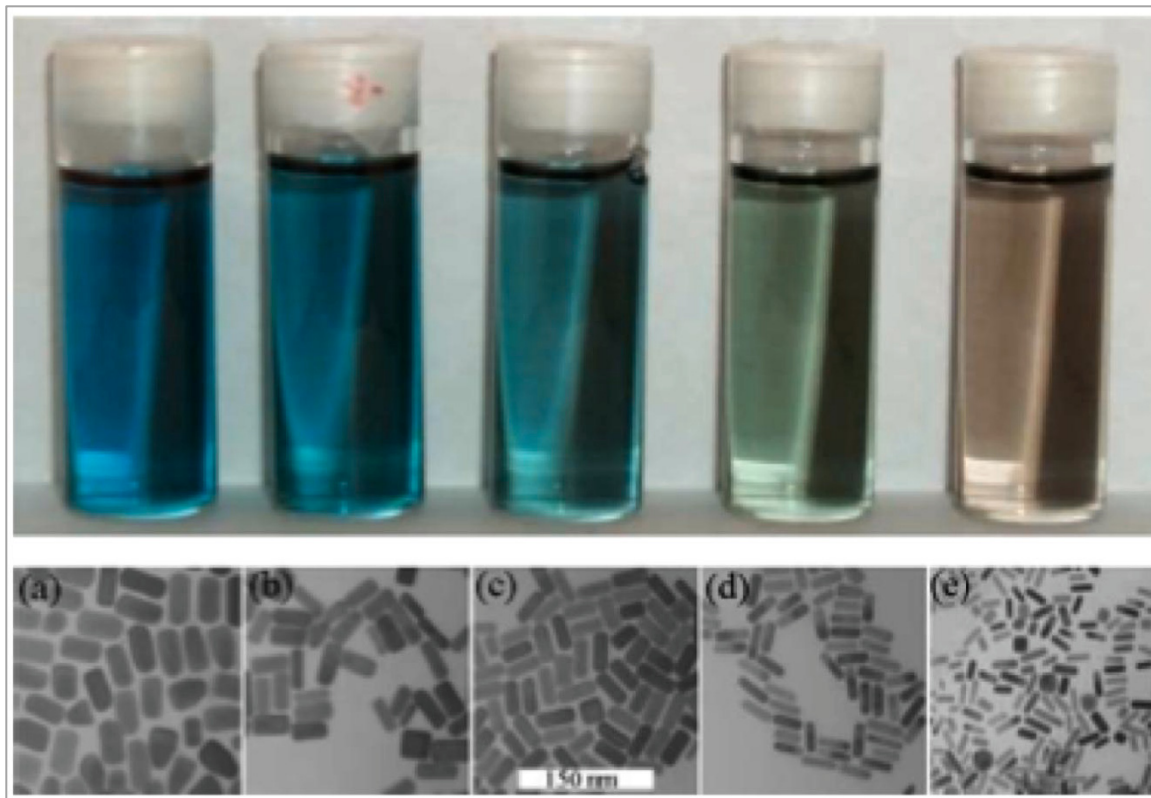


Figure 4. 7: Colloidal solutions and the corresponding micrographs of Au NRs with different aspect ratios [adapted from Ref. [71]].

Based on Gans theory, short Au NRs display two absorption bands in the visible-near IR region of the spectra. These bands are a result of the oscillation of conduction electrons with respect to the rod axes. The first band is the transverse absorption mode that occurs due to the oscillation of the conduction electrons along the rod's short axis. This mode exhibits almost as same wavelength as the spherical NP, $\sim 520\text{-}530\text{ nm}$. The other absorption mode is the longitudinal one, which is corresponding to the oscillation of free electrons along the rod's long axis. The longitudinal absorption peak appears broadened, and exhibits a shifting of the peak maxima toward longer wavelengths with

increasing the aspect ratio of the rods [35,64,67]. Figure 4.8 illustrates the changing in the absorption peaks for Au NP by elongating it along one axis.

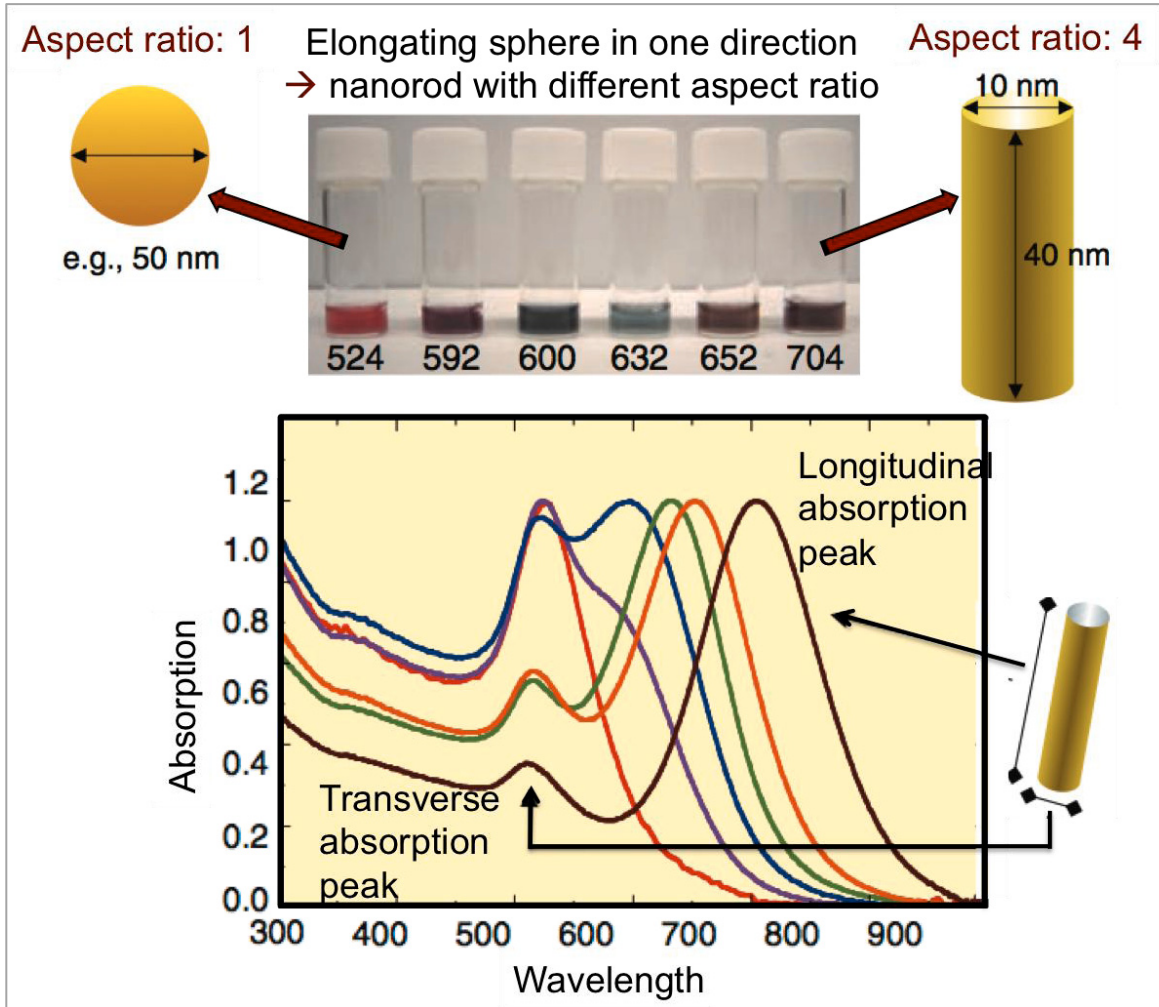


Figure 4. 8: Elongating of the spherical Au NP along one axis produces rods with different aspect ratios and optical responses. The numbers at the bottom of each bottle indicate the resonance peak [adapted from Ref. [79]].

To calculate the extinction coefficient of Au NRs analytically, the shape of the rods has to be revealed microscopically. Transmission electron microscopes (TEM) of various NRs research show that the rods' shapes appear more likely cylinders or sphero-

capped cylinders rather than ellipsoids. Yet, finding the solution for such shapes is not possible analytically. Therefore, the NRs have been treated as ellipsoids and the Gans formula, Eq. 3-10, is applied to explain their optical responses [71].

For small ellipsoids embedded in the same medium, the variation in the absorption peak position with respect to their aspect ratio could be predicted from Gans formula, by plotting the value of the resonance condition, ϵ_m/ϵ_d , versus the depolarization factor (or aspect ratio parameter) L as illustrated in figure 4.9 [60]. For spherical shape, one resonance peak appears regardless the polarization of the incident electric field. By elongating the sphere and increasing the aspect ratio, two branches of the resonance appears: when the electric field of the incident light is perpendicular to the rod's long axes (transverse mode), the resonance condition move up toward the zero. On the other hand, if the electric field is parallel to the rode's long axes (longitudinal mode), the resonance condition moves down toward $-\infty$. The transverse absorption mode is approaching $L = 1.0$, which is corresponding to $\epsilon_m/\epsilon_d = 0$, means that $\epsilon_m = 0$. The curve of figure 4.9 implies that for Au NRs in water, the transverse mode occurs at 510 nm (as compared to 520 nm for spheres). Thus, it is slightly blue-shifted as the rods grow. In contrast, the longitudinal mode is red-shifted to more negative values of the ratio ϵ_m/ϵ_d [60,71].

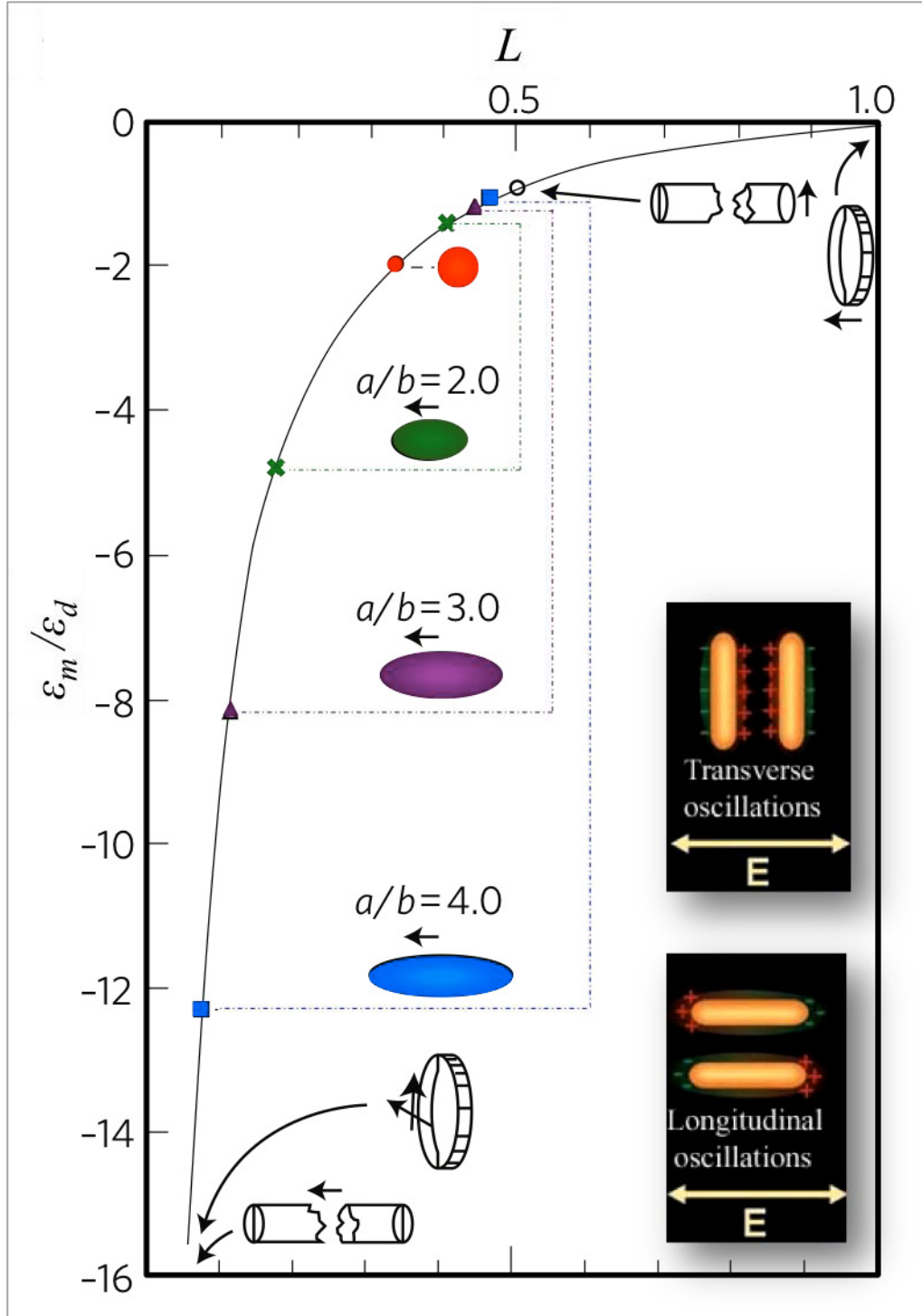


Figure 4. 9: The resonance condition ϵ_m/ϵ_d versus the depolarization factor L according to Eq. 3-10 for a sphere ($\epsilon_m/\epsilon_d = -2$, corresponding to $L = 1/3$) and ellipsoids with different aspect ratio (a/b) for different E field polarizations (presented by the arrow next to the ellipsoid) [re-drawn from Ref. [60]].

It is important to mention that the longitudinal and transverse absorption modes of the NRs are independent to each other. Thus, only one resonance mode appears by aligning the rods on one direction, as in the case of depositing them on a substrate [71]. The shape and position of the resulted peak deviate from the corresponding one in the colloidal solution since the substrate effect will appear in the former case as well as the effect of both orientation and coupling between rods.

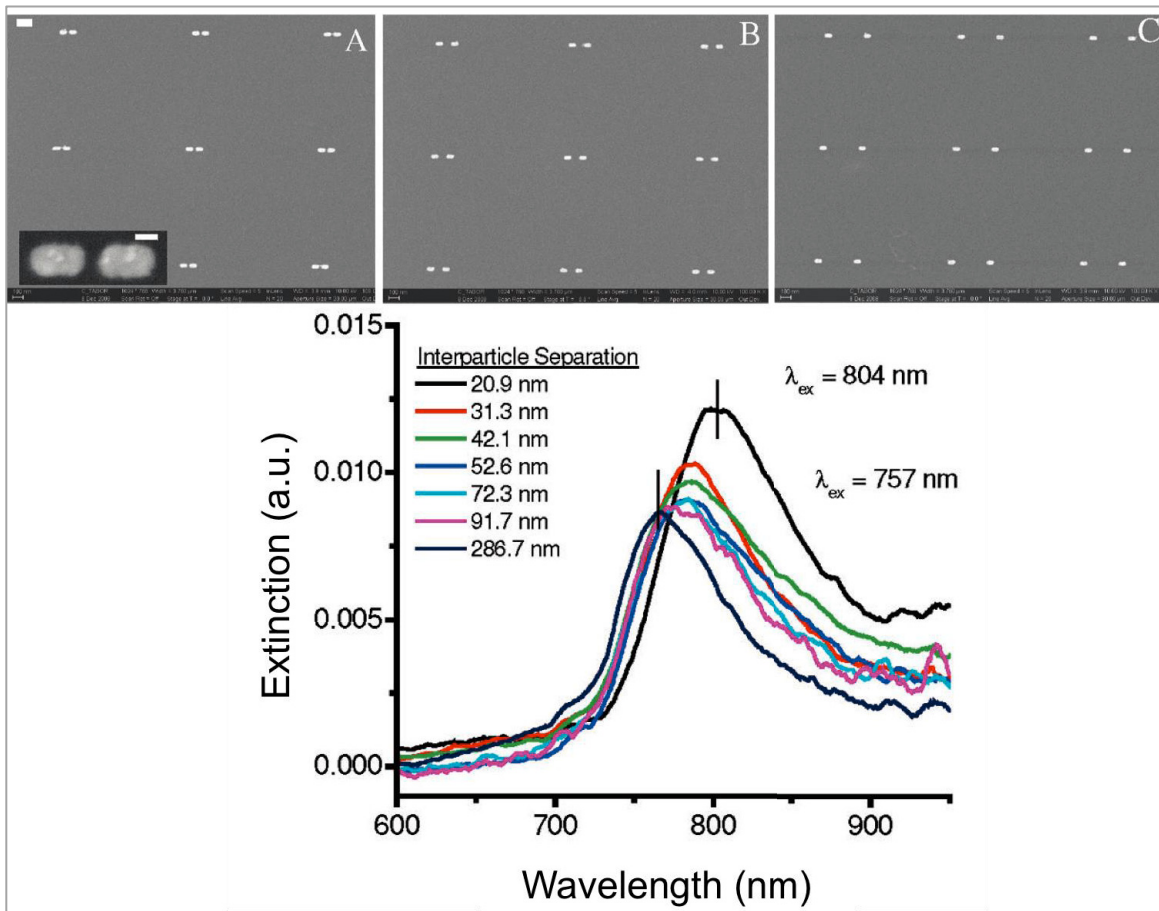


Figure 4. 10: SEM micrographs of gold nanorods deposited with various interparticle separations: 20.9, 72.3, and 286.7 nm. The aspect ratio of the rods is ~ 1.7 [adapted from Ref. [80]].

Figure 4.10 shows the effect of the interparticle separation between two rods, aligned with their long axes parallel to the substrate, on the absorption peak of their spectra. As it is presented in the absorption profile, only one absorption mode appears, that is the longitudinal one [80]. The coupling between two rods affects the peak position as well as intensity. Less intense, broadened and red-shifted peak occurs with increasing the interparticle distance from ~ 30 nm to 287 nm.

In the coming chapters, the processes of fabricating and optimizing the performance of organic solar cells are presented, following by the experimental results of incorporating gold nanorods into organic solar cell layers.

CHAPTER V

Fabrication Process of Bulk Heterojunction Solar Cell

Before presenting the work of incorporating Au NRs into our BHJ-OSC devices, we will cover, in this chapter, the fabrication process of our P3HT:PCBM BHJ-OSC in details.

Most of the fabrication steps of our devices were performed inside a cleanroom. Generally, the device fabrication process comprises three stages: preparation of the anodic substrate, preparation and deposition of the photoactive solution, and thermal evaporation of the cathode materials. For device fabrication, we followed the method that was reported in Ref. [81] with modifications. All designed and fabricated tools that were used in the manufacturing of BHJ-OSC devices were done by the author herself unless it mentioned otherwise. Figure 4.1 illustrates the final configuration of the BHJ-OSC device that was fabricated and examined in our study.

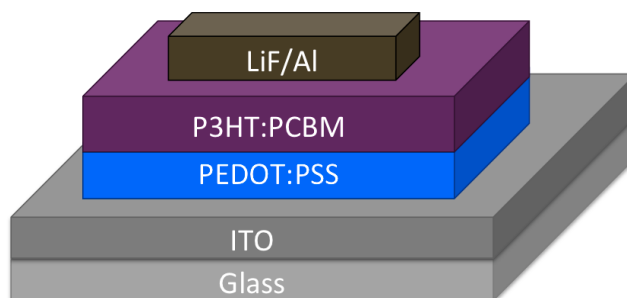


Figure 5. 1: Schematic diagram of the final configuration of our manufactured OSC device, ITO-coated glass is the anodic substrate; PEDOT:PSS is the anodic buffer layer; P3HT:PCBM is the photoactive layer; and LiF/Al is the cathode.

5.1 Preparation of the ITO-coated glass substrate

This step involves the processes of cutting, patterning, and etching the glass substrate that is coated with the anodic electrode, ITO.

5.1.1 Preparing the substrate for patterning

To prepare our ITO-coated glass substrate that carries eight devices simultaneously, a board of ITO-coated glass is first cut into 2.6 cm × 3.7 cm using diamond cutter, and cleaned. The lithography technique is then used to pattern the substrate before etching the ITO areas to a certain geometry.

Cleaning the substrate: prior the patterning process, the ITO-substrate has to be cleaned well. The first cleaning step is done using detergent and deionized (DI)-water. Then the substrate is passed through a cleaning process by immersing it sequentially in ultrasonic bathes of acetone, isopropyl and DI-water for 20 min each. After that, the substrate is dried with a nitrogen flow, and placed on top of a hot plate for 20 min to be dehydrated at 150°C. Figure 5.2 presents the SEM micrograph of a pre-cleaned ITO-coated glass substrate.

5.1.2 Patterning the ITO

An ultraviolet lithography patterning is performed using the optical mask-aligner machine (OAI model 200). For the patterning process, first a mask with a certain geometry is designed, then it is used to cover the ITO-substrate during its exposure to the ultraviolet lamp.

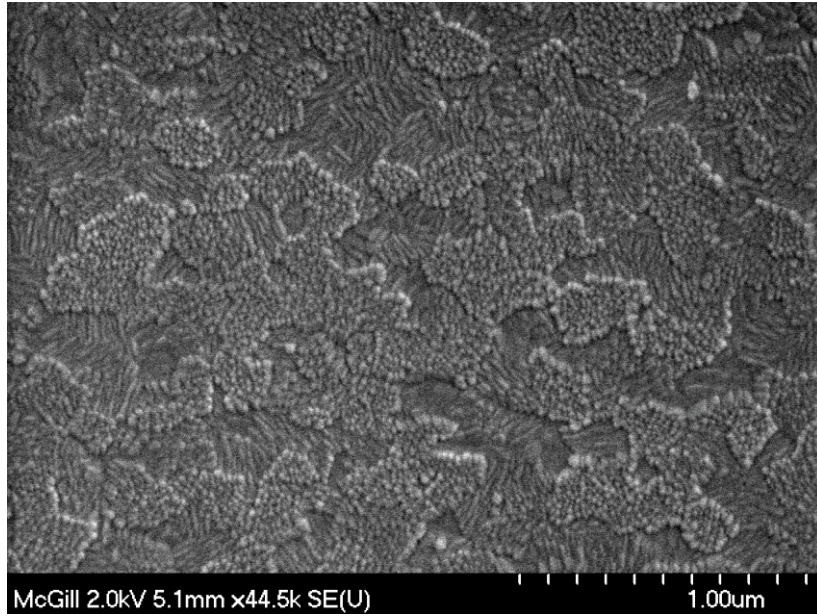


Figure 5. 2: An SEM image for a pre-cleaned ITO-coated glass.

Designing the lithography mask: a schematic presentation of the mask is shown in figure 5.3. The eight rectangular areas present the only spots that will be covered with ITO by the end of the etching procedures, and hence will carry our eight devices. This designed geometry is then printed in a flexible/transparent film.

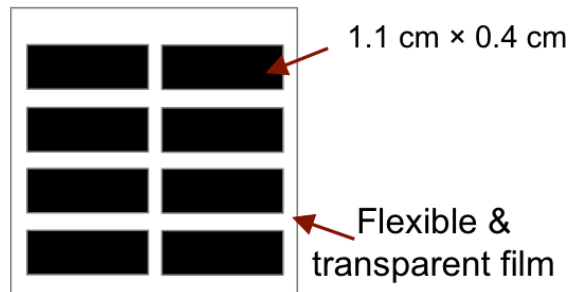


Figure 5. 3: The geometry of our used mask in the lithography patterning.

Exposing the substrate to the ultraviolet lamp: on top of the previously cleaned ITO-substrate, a photoresist (S1811, ROHM and HAAS electronic materials) was spin-coated for 30 sec at 4000 RPM, and then baked at 115°C for 1 min. After that, the substrate is fixed on the substrate-holder available in the mask-aligner machine. The previously designed mask has also to be fixed to the mask-aligner machine covering the ITO-substrate. The substrate is then exposed to the ultraviolet lamp for 6 sec. The lamp intensity during the exposure is $\sim 20 \text{ mW/cm}^2$. Afterward, the substrate is immersed in a developer (MFTM-319, ROHM and HAAS electronic materials) for 45 sec to develop the photoresist, followed by washing with DI-water, and then drying with nitrogen flow. At this step, the photoresist is removed from the ITO-substrate except for the eight rectangular areas that were protected, by the mask, from being exposed to the ultraviolet lamp. The substrate is then placed on top of a hot plate and baked at 130°C for 3 min.

5.1.3 Etching ITO

To remove ITO from the undesired areas in our substrate (the areas that are not covered with the photoresist), the previously patterned substrate is immersed in a bath of a hydrochloric acid for ~ 6 min, then it is washed with DI-water. The hydrochloric acid acts in removing the ITO, however, the eight ITO areas that are covered with the photoresist will be protected from the acid reaction. To remove the remained photoresist, the substrate is immersed in an acetone bath, washed with DI-water, and dried with a nitrogen flow. To ensure that the ITO is totally removed from the substrate except for the eight areas that were covered with the photoresist during the etching process, a voltmeter is used to check that there is no contact between the remained ITO areas on the glass

substrate. Afterward, the substrate is cleaned again following the same cleaning process mentioned in section 5.1.1. For dehydrating, the substrate is dried with a nitrogen flow and annealed at 120°C for 20 min.

5.2 Deposition of the PEDOT:PSS anodic buffer layer

The previously patterned and cleaned ITO-substrate is treated with an oxygen plasma for 35 sec. The purpose of this treatment is to enhance (increase) the work function of the ITO [82], and to activate its surface. Immediately after the oxygen plasma treatment and under an ambient environment, a 30 nm thick layer of the PEDOT:PSS (CLEVIOS™ P VP Al 4083, purchased from HC Stark) is deposited by a direct spin-coating of the PEDOT:PSS aqueous solution, as received, after being passed through a 0.45 μm PVDF filter. The spin-coating speed is 4000 RPM for 30 sec, with the acceleration of 10 sec to 1100 RPM. The Glass/ITO/PEDOT:PSS substrate is then baked at 120°C for one hour in an ambient condition to be dehydrated. Afterward, the substrate is transferred to a nitrogen filled glove-box for the deposition of the photoactive layer, P3HT:PCBM.

5.3 Preparation and deposition of the photoactive solution

The photoactive solution is prepared inside a nitrogen filled glove-box with a pressure of 3 mbar and a humidity level less than 0.1 ppm. For the solution preparation, 20 mg of P3HT (98% regioregularity, <50,000MW, average molecular weight, purchased from Rieke Metals) and 16 mg of PCBM (>99.5%, purchased from Sigma-Aldrich) are

separately dissolved in 1 ml of 1, 2-dichlorobenzene (99%, anhydrous, Sigma-Aldrich). After that, equal volumes of P3HT and PCBM solutions are mixed together to yield a blend of the polymer:fullerene solution with a ratio of 1:0.8. This ratio was chosen among several others (1:2 and 1:1) since it has been used to produce devices with a high performance [11]. The P3HT:PCBM blend is then vigorously stirred overnight at room temperature to yield a more homogeneous solution. Afterward, a layer of P3HT:PCBM, ~ 100 nm, is deposited using spin-coating approach on top of the ITO/PEDOT:PSS modified electrode after passing the P3HT:PCBM blend through a 0.45 μm PTFE filter. We experimentally developed our own spin-coating recipe to deposit the active solution. The recipe consists of three steps: first at low speed of 200 RPM for 5 sec, then at 500 RPM for 5 sec, and then at 1000 RPM for 60 sec. The ITO/PEDOT:PSS/P3HT:PCBM film was then left to dry in a covered petri-dish for 30 min inside the glove-box. The surface structure of the resulting photoactive film was characterized using a scanning electron microscopy (FEG-SEM Hitachi S-4700), and the scanning mode of atomic force microscopy (AFM NanoInk's DPN 5000). The SEM and AFM micrographs of the P3HT:PCBM film deposited on a glass substrate are presented in figures 5.4a and b, respectively.

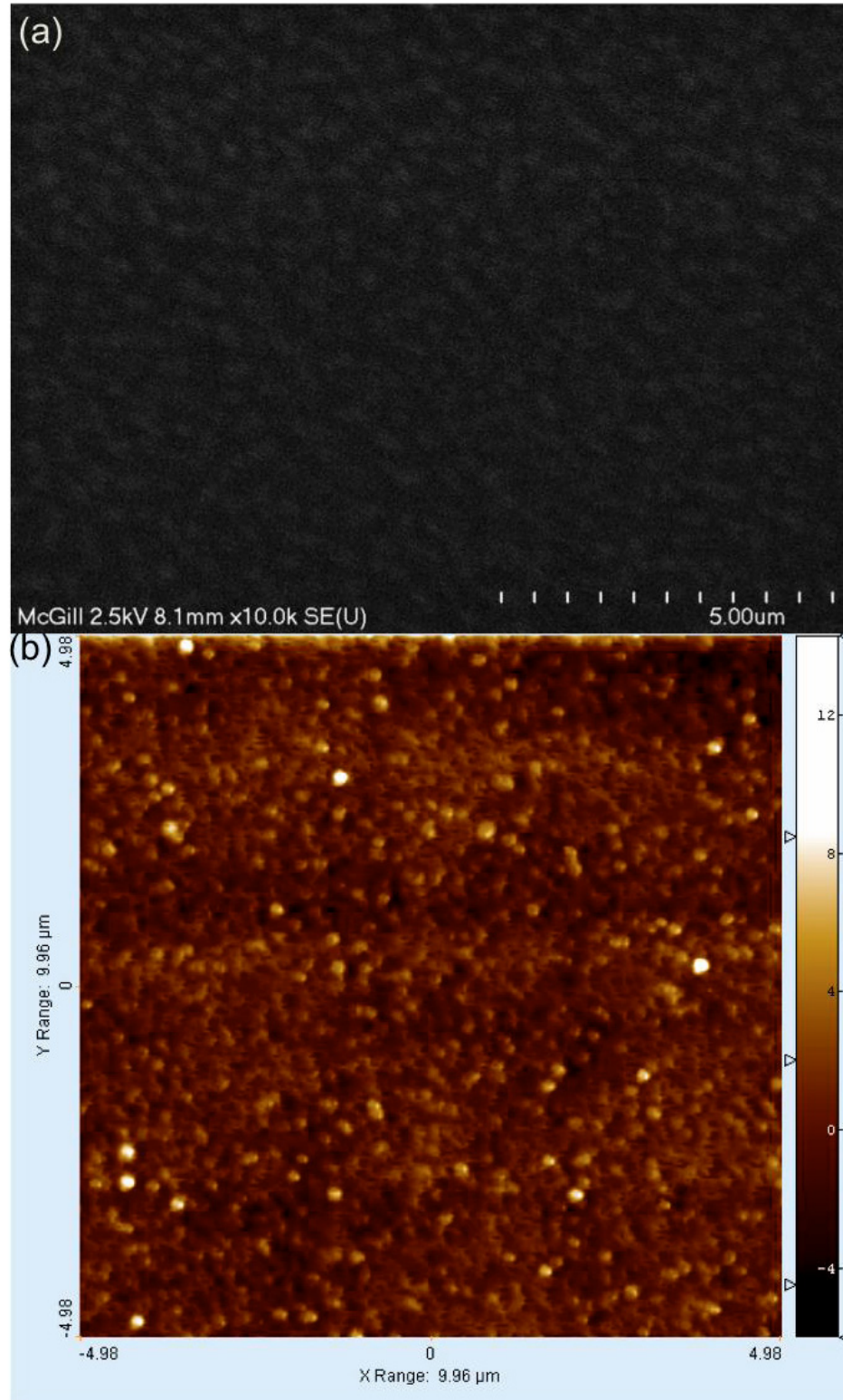


Figure 5. 4: (a) SEM and (b) AFM micrographs of ~ 100 nm P3HT:PCBM film spin-coated on a glass substrate. The images show the phases of P3HT and PCBM. The surface roughness of the P3HT:PCBM is ~ 1.4 nm.

5.4 Thermal evaporation of the cathode materials

After spin-coating the photoactive layer, samples are then transferred to the evaporator for evaporating the cathode materials. During samples transferring to the evaporator, the photoactive layer is exposed to the air, which affected their PCE. The thermal evaporation of the cathode materials is performed through an Al shadow mask. The Al shadow mask consists of two parts: the substrate holder and the Al mask.

Preparation of the substrate holder: the substrate holder is made of stainless steel material and designed to carry four substrates simultaneously. This holder has a special geometry that is carefully chosen to fit with the dimensions of our substrates. Figure 5.5 presents the designed substrate holder.

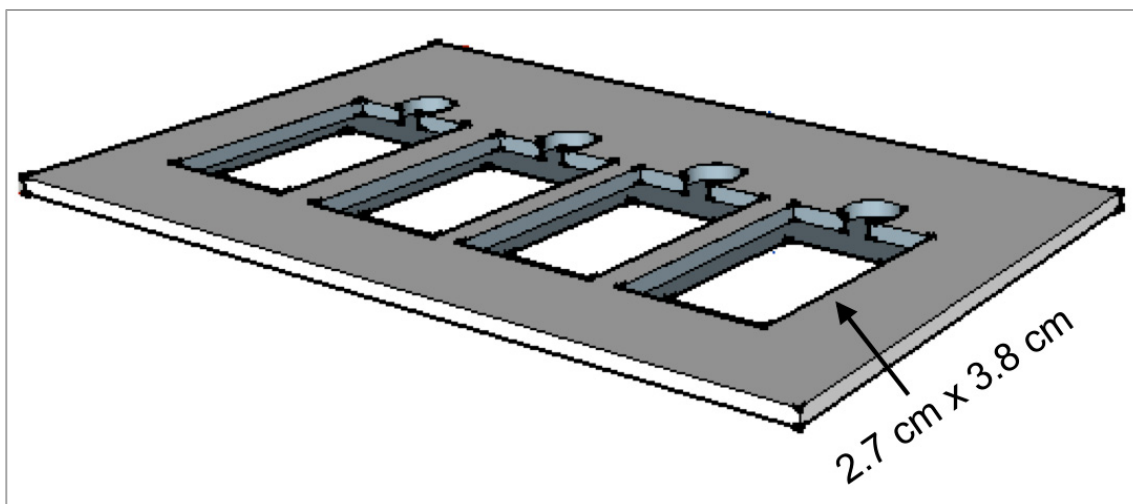


Figure 5. 5: Schematically diagram for our designed substrate holder.

An Al mask is then fabricated and fixed in the substrate holder. The fabrication of the Al mask is as follows:

Preparation of the Al mask: an Al foil-baking tray with a thickness of 0.16 mm is used as an Al board. The preparation process of the Al mask is similar to the one for preparing the ITO mask. First, an Al board has to be cut into 3 cm × 4 cm. Then it is cleaned and patterned using the lithography technique before being etched to a specific geometry. For the Al patterning, a mask with the proper geometry, depicted in figure 5.6, is designed and printed on a flexible/transparent film.

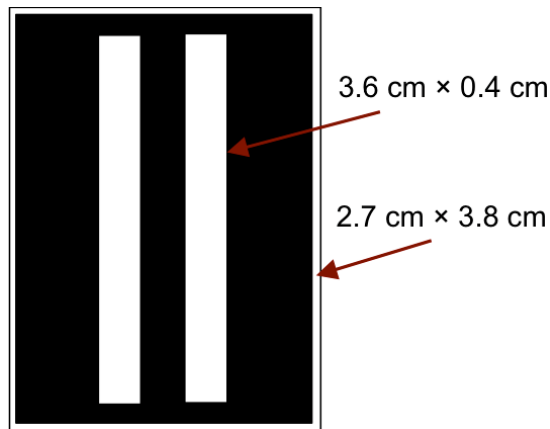


Figure 5. 6: Our Al mask on a transparent and flexible film.

After cutting the Al film, it is cleaned and patterned following the same processes of cleaning and patterning of the ITO-substrate. After developing and baking the Al/photoresist film, an extra layer of the photoresist is spin-coated at 2000 RPM for 30 sec on the other face of the Al film, and then baked for 2 min. Afterward, the undesired Al is removed from the Al film by immersing it in a bath of a hydrochloric acid for ~ 10 min until the Al areas that are not exposed to the ultraviolet lamp get dissolved. The photoresist is then removed using acetone. After that, the Al substrate is washed with DI-water and cleaned as mentioned previously. By completing this step, the Al mask

becomes ready. The Al masks are then fixed on the substrate holder. By finishing this step, the Al shadow mask becomes ready. Figure 5.7 illustrates the final configuration of the fabricated Al shadow mask.

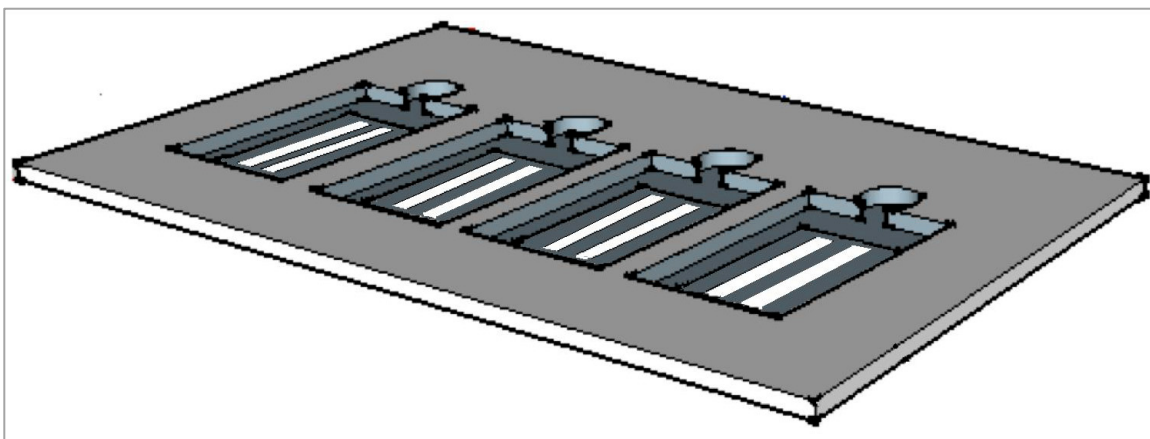


Figure 5. 7: Schematic diagram for the final configuration of the Al shadow mask.

After fixing the Al shadow mask inside the thermal evaporator, Glass/ITO/PEDOT:PSS/P3HT:PCBM substrates are then placed on the Al shadow mask inside the evaporator. The substrates active faces are directed downward and exposed to the cathode material.

Evaporation of the cathode materials: the used cathode materials in our cells are LiF and Al (purchased from Alfa Aesar). Both of them are deposited on top of the photoactive film using thermal evaporation technique. The thickness of the evaporated Al film is ~ 90 nm. The optimized thickness of the evaporated LiF layer, as presented in our next chapter, is ~ 0.6 nm. The material thicknesses were determined using a mechanical profilometer (Veeco Dektak150). The evaporation of the cathode materials is performed

under a pressure less than 10^{-6} torr, in which the evaporation rates are $\sim 1 \text{ \AA /sec}$ and $\sim 2.5\text{-}5 \text{ \AA /sec}$ for the LiF and Al, respectively. By completing this step, eight devices with a photoactive area of $\sim 0.16 \text{ cm}^2$ /each will be produced on each ITO-substrate. The photoactive area of the device is defined by the area that is confined between the ITO anode and the Al cathode.

5.5 Device annealing

The manufactured OSC devices are placed on top of a hotplate inside the nitrogen filled glove-box for the thermal annealing treatment. The annealing process (pre or post) and the annealing temperature are determined by optimization procedures as presented in the next chapter. A surface thermometer (Extech 392052) was used to calibrate the hotplate temperature. After the annealing treatment, devices are placed in contact with a metal block in order to cool-down before being characterized under ambient conditions without any encapsulation.

5.6 Characterization of the device

The resulting devices are characterized in air using a solar simulator (xenon lamp-Oriel instruments) that is equipped with AM 1.5G filter. The output intensity of the lamp is adjusted to 100 mW/cm^2 using a Si photodiode (LI-200 Pyranometer). The current-voltage JV measurements under illumination and in dark conditions are carried out using a Keithley 2400 programmable voltage source-meter and a Keithley 617 programmable electrometer. The PV parameters are extracted using the labView computer program. In our devices, the obtained values of the PCE were generally low due to the devices

exposure to the air at a certain point during evaporation and characterization processes.

Figure 5.8 schematically shows how our devices are connected for characterization.

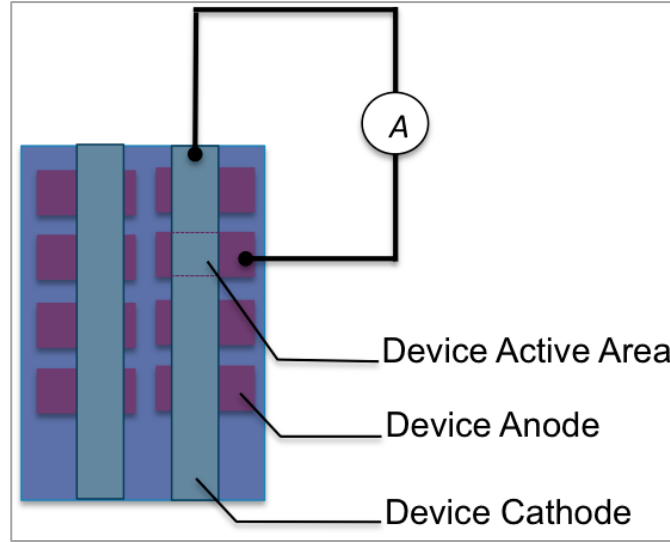


Figure 5. 8: A substrate with eight devices is ready for characterization.

EQE measurements: the EQE measurements of our fabricated devices are carried out by varying the wavelengths of the incident light from 400 to 800 nm using a Newport 74000 monochromator. As the cut-off wavelength for our monochromator is around 400 nm, the EQE response is not measurable below that wavelength. The power intensity of the incident light is calculated using a calibrated Si photodiode (Thorlabs FDS100).

Characterization box: for the characterization process, we designed and fabricated a special characterization box. The box was made precisely to be suitable for carrying one substrate each time. Each one of the eight devices in the substrate is able to be fixed and connected easily to the conducting probes that are connected to the source-

meter equipment. Pictures for our fabricated characterization box are presented in figure 5.9.

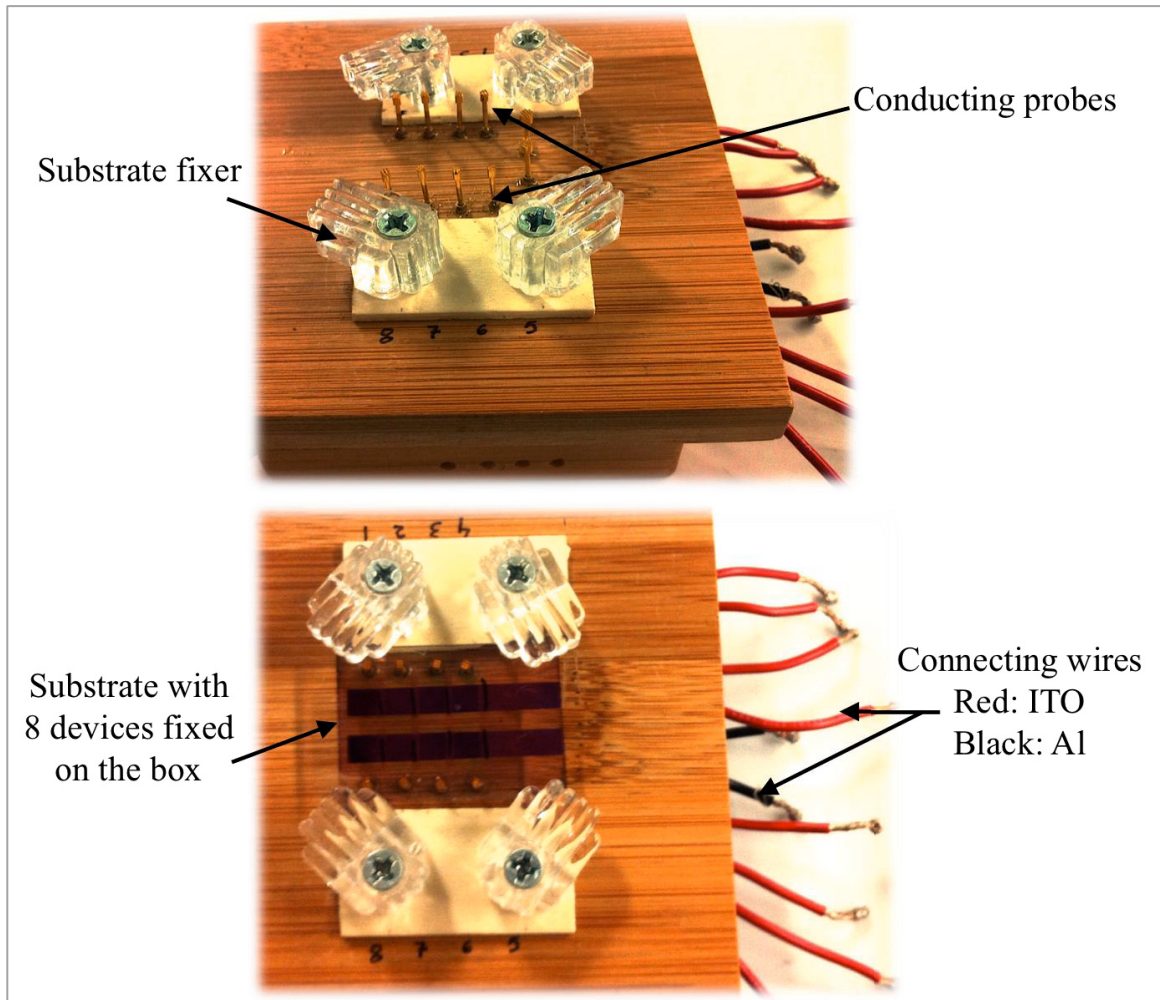


Figure 5. 9: Pictures of the designed characterization box show the connecting probes, connecting wires, and the substrate fixer.

Next chapter presents the optimization process of the fabrication conditions of our P3HT:PCBM bulk heterojunction solar cells.

CHAPTER VI

Optimization of the Fabrication Conditions of P3HT:PCBM Solar Cell

So far, the best reported value of the power conversion efficiency for the P3HT:PCBM bulk heterojunction solar cell is around 5% [19,20]. The efficiency of BHJ-OSCs depends very much on the preparation conditions. This chapter presents the optimization processes of some important preparation parameters, which are the thickness of LiF layer and the suitable annealing treatment as well as the annealing temperature.

6.1 Optimizing the thickness of LiF

Inserting an interfacial layer of LiF in the boarder between the organic film and the metallic cathode is a well-known approach in the fabrication process of OSCs, which dramatically improves the properties of the organic/metal interface and results in enormous enhancement in all PV parameters [11,15,46,48]. In spite of that, there is no universal agreement on the real role of the LiF in enhancing the performance of OSC devices. However, it has been suggested that the LiF interfacial layer helps in [46,48]:

- Facilitating the tunneling of electrons to the Al cathode by lowering its work function;
- Acting as a blocking layer that minimizes the quenching of excitons at the organic/metal interface;
- Forming an interfacial barrier that pins Fermi level and minimizes the diffusion of the ionic metal into the organic layer.

- Preventing the organic layer from the hot Al atoms during the formation of the Al cathode by the thermal evaporation process.
- Acting as an optical spacer that redistributes the electric field inside the organic device, which shifts the absorbing region of the incident light from the metal interface to the organic film. This in turn results in an increase in the devices short circuit current.

The thickness of the LiF layer is a very important issue that affects the overall performance of the device. The reported LiF thickness varies from 0.6 to 1 nm [48,82]. Herein, we optimized the thickness of the LiF that would work well with our materials.

6.1.1 Procedures

The OSC devices were fabricated as has been mentioned earlier. After depositing the photoactive layer, substrates were transferred into the evaporator for thermal evaporation of the cathode. Before evaporating the Al, a nano-layer of LiF with two different thicknesses, 0.6 nm and 1 nm, were evaporated on top of the organic layer. The LiF evaporating rate was $\sim 1 \text{ \AA}/\text{sec}$. After evaporating the Al cathode, devices were characterized under ambient conditions.

6.1.2 Results and discussion

Table 1 summarizes the PV parameters for reference device (without LiF) and devices incorporating the interfacial layer of LiF between the organic/metal interface.

The corresponding JV characteristics for the resulting devices upon illumination and in dark conditions are presented in figures 6.1a and 6.1b, respectively.

Table 1: *The average PV parameters for reference device along with the ones incorporated LiF between P3HT:PCBM/Al interface. These values were obtained from at least five devices made under the same conditions.*

Device type	V_{oc} (V)	J_{sc} (mA/cm ²)	R_S (Ωcm^2)	FF%	PCE%
Reference-no LiF	0.38	-1.58	6.67	64.9	0.36
1 nm LiF	0.52	-2.19	5.56	68.9	0.68
0.6 nm LiF	0.49	-2.37	4.88	67.9	0.74

It is clear from table 1 that inserting a thin layer of LiF in the interface between the organic film and the Al cathode helped in enhancing the overall device PV parameters. The J_{sc} was increased by up to 50%, the V_{oc} by up to $\sim 37\%$, the FF by up to 6% and the PCE by up to $\sim 100\%$. We found that the optimal thickness of the LiF in our experiment was 0.6 nm. The series resistance of the devices (calculated from the slope invers of the dark JV characteristics at a voltage 0.8 V) were reduced by $\sim 27\%$ with incorporating the LiF layer, which explains the enhancement in the FF. We also studied the effect of too thick LiF layers on the device performance by preparing a set of devices with ~ 6 nm LiF layer on top of P3HT:PCBM film. In that case, we found that such thick LiF layers reduced dramatically the performance of the resulting device [15].

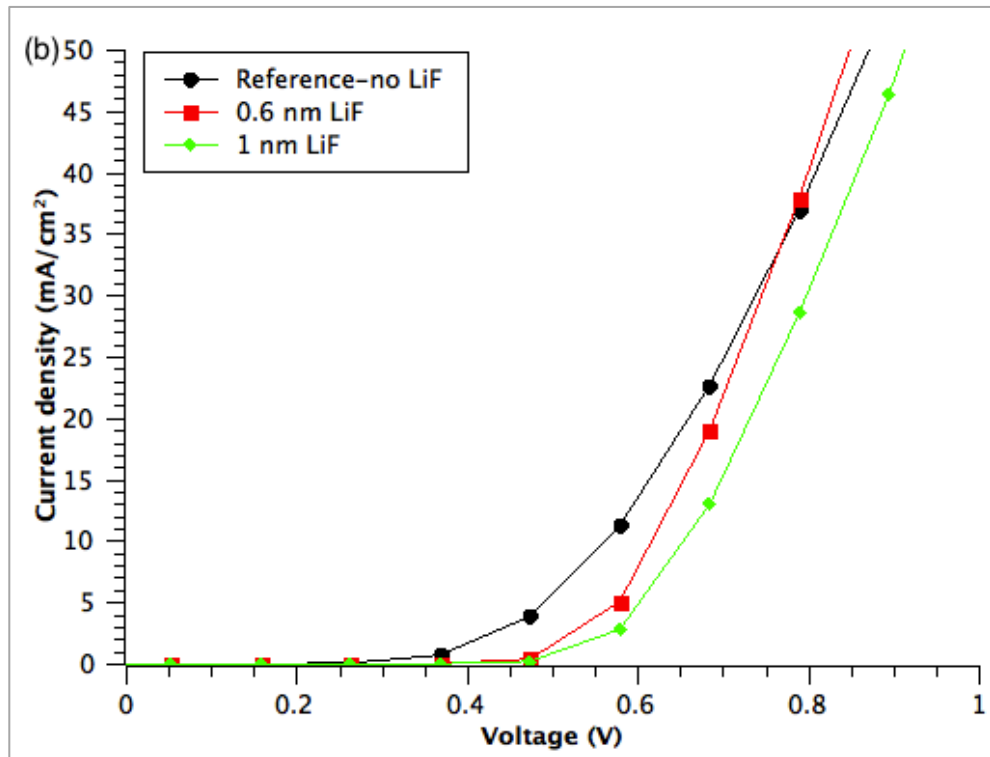
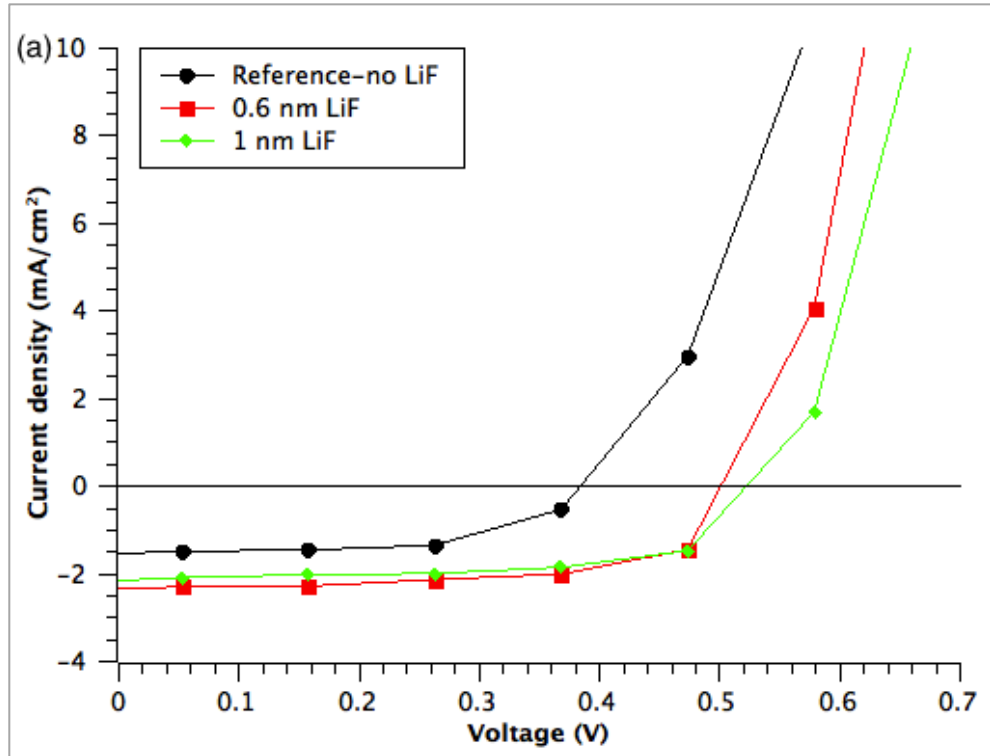


Figure 6. 1: The JV curves for reference device along with devices incorporating LiF as an interfacial layer between organic/Al interface (a) Under illumination and; (b) In dark.

6.2 Optimizing the thermal annealing process and temperature

Many reported studies show that the thermal annealing of the P3HT:PCBM film has an enormous effect on the solar cell performance [43,44,81,83,84,85]. The annealing implies placing the device in a direct contact to a hot plate for a certain period of time. Basically, there are two approaches for the thermal annealing treatment in organic photovoltaic devices:

- Pre-annealing approach: which is the annealing of the photoactive film after being spin-coated on the ITO/PEDOT:PSS anode, and before evaporating the Al cathode. This kind of annealing is also referred as “film annealing”.
- Post-annealing approach: which is the annealing of the complete device after evaporating the cathode material. This kind of annealing is also referred as “device annealing”.

Generally, the thermal annealing treatment of OSC films/devices enhances their PV parameters. This enhancement is related to the improving in the crystalline morphology of the photoactive layer, in which the interfacial surface area between the polymer/fullerene domains increases, which results in efficient charge generation [44,83]. In addition, the annealed P3HT:PCBM film exhibits more packed morphology, in which the interpenetrating networks between polymer and fullerene domains become more obvious [44,84,85], with aspects of size ~ 10 nm [86].

6.2.1 Effect of thermal annealing of the P3HT:PCBM film on its absorptivity

Before presenting the process of optimizing the annealing kind in our devices, we present here the effect of the annealing treatment in the absorption of the photoactive film. Figure 6.2 compares the absorbance spectra for P3HT:PCBM film before and after thermal annealing treatment for 30 min at 130°C. These measurements were carried out using a UV-Vis spectrophotometer (PerkinElmer LAMBDA 650 spectrophotometer). As it is clear from the figure, there is a considerable enhancement in the absorption of the photoactive film, by up to 12%, after the thermal annealing treatment.

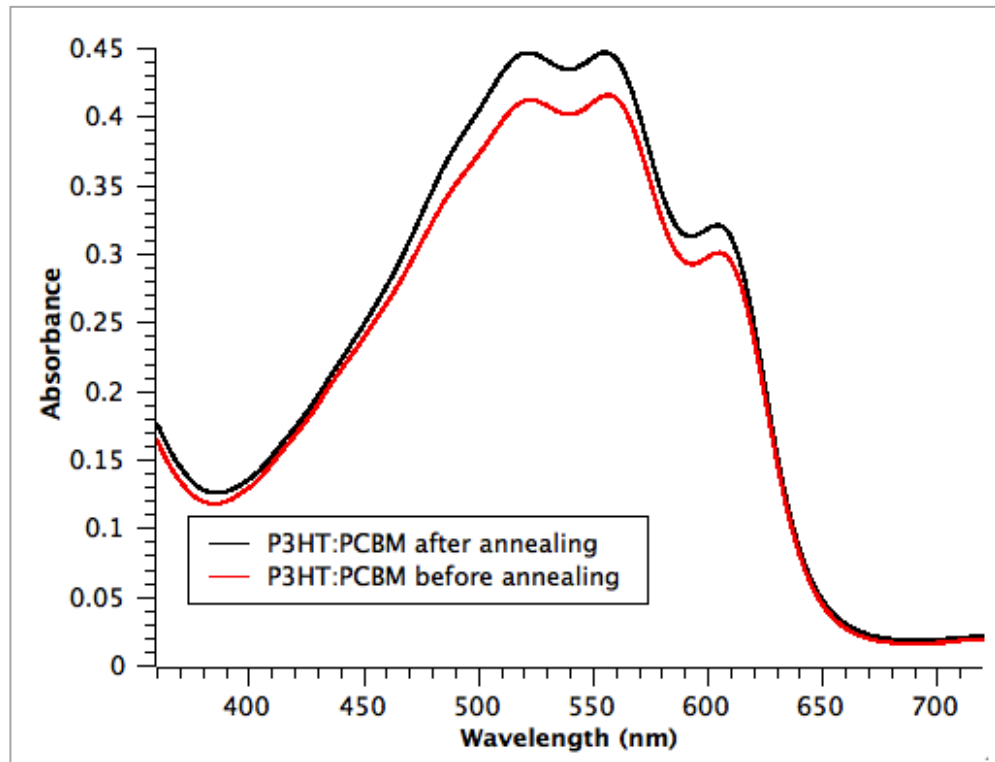


Figure 6. 2: The absorbance spectra for P3HT:PCBM film before and after thermal annealing for 30 min at 130°C.

The increase in the absorption of the P3HT:PCBM film via annealing treatment could be considered as another evidence for annealing effect on the packing morphology of the photoactive film. By increasing the packing and crystallinity of the polymer, the conjugated π electrons become more delocalized since the band gap between π and π^* orbitals becomes lower as compared with the un-annealed film. This in turn enhances the optical transition and increases the film absorption of the incident light [43,85].

6.2.2 Optimizing the annealing process

6.2.2.1 Procedures

To choose the kind of annealing treatment that is appropriate for our OSC devices, devices were fabricated as has been mentioned earlier. For the pre-annealed devices, we annealed the substrate of the configuration ITO/PEDOT:PSS/P3HT:PCBM before evaporating the cathode material (Al). For post-annealed devices, we annealed the complete devices, ITO/PEDOT:PSS/P3HT:PCBM/Al. Both films and devices were annealed at a constant temperature, 100°C, for 30 min.

6.2.2.2 Results and discussions

Figure 6.3 illustrates the current-voltage measurements under illumination and in dark conditions for OSC devices that were post/pre-annealed, and table 2 summarizes the PV parameters corresponding to the resulting devices.

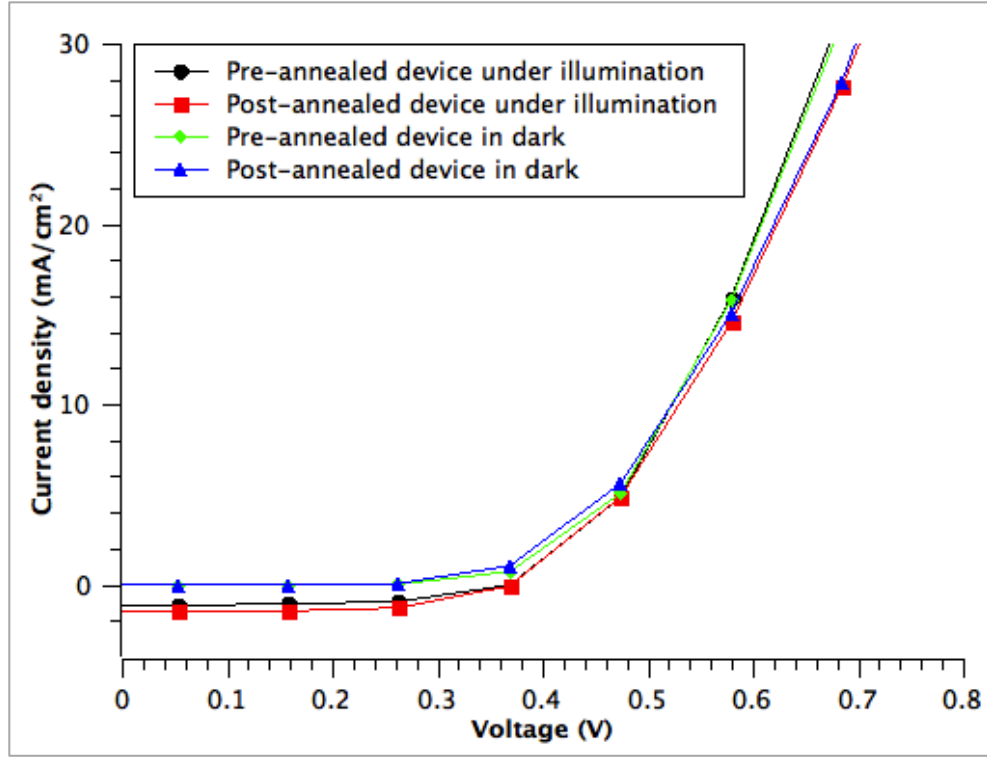


Figure 6. 3: The JV curves for post/pre-annealed OSC devices under illumination and in dark conditions.

Table 2: *The average PV parameters for devices those were pre- and post-annealed. Theses values were obtained from at least five devices made under the same conditions.*

Device type	V_{oc} (V)	J_{sc} (mA/cm ²)	R_S (Ω cm ²)	FF%	PCE%
Pre-annealed	0.37	-1.22	5.26	57.9	0.24
Post-annealed	0.37	-1.54	5.26	61.9	0.33

As table 2 illustrates, the post-annealing treatment showed better results as compared with the pre-annealing one, in which most of the PV parameters were enhanced. While there were no difference in values of V_{oc} and R_S for both kinds of annealing; pre and post, the J_{sc} , FF, and PCE for the post-annealed devices were

increased, respectively, by up to ~ 26%, 7%, and 38% as compared with the pre-annealed devices.

Many reported studies compared the morphology between pre- and post-annealed P3HT:PCBM films. Such comparison showed that the post-annealed film exhibits rougher surface than that of the pre-annealed one. When the surface roughness/area between the photoactive film and the Al cathode increases, more efficient devices are produced. This is due to the increase in the number of the photogenerated charge carriers near the Al cathode, which raises their potential to be efficiently collected by cathode before being recombined [43]. Hence, the increase in the surface roughness between the photoactive film and the metallic electrode promotes more efficient generation, extraction and collection of the photogenerated charge carriers, which results in better efficiency [43,44,84,85].

6.2.3 Optimizing the post-annealing temperature

6.2.3.1 Procedures

To optimize the post-annealing temperature that is appropriate for our OSC devices, devices were fabricated as has been mentioned earlier. After depositing the LiF/Al cathode, devices of the configuration ITO/PEDOT:PSS/P3HT:PCBM/LiF/Al were annealed at various temperatures; 130, 150 and 170°C, for 30 min. There was no annealing treatment for the reference device. All set of devices were then characterized under ambient conditions.

6.2.3.2 Results and discussions

Figure 6.4 illustrates the current-voltage measurements under illumination and in dark conditions for reference device (not annealed) along with devices that were post-annealed at various temperatures; 130, 150 and 170°C for 30 min, and table 3 summarizes the PV parameters corresponding to the studied devices.

Table 3: *The average PV parameters for reference device along with devices that were post-annealed at 130, 150 and 170°C for 30 min. These values were obtained from at least five devices made under the same conditions.*

Device type	V_{oc} (V)	J_{sc} (mA/cm ²)	R_S (Ω cm ²)	FF%	PCE%
Reference-no annealing	0.59	-2.26	7.14	60.2	0.75
At 130°C	0.52	-6.00	9.09	53.6	1.66
At 150°C	0.53	-5.84	6.06	55.1	1.67
At 170°C	0.51	-5.43	7.69	42.4	1.21

It is clear from table 3 that by elevating the post-annealing temperature successively to 130, 150 and 170°C for 30 min, both J_{sc} and PCE increased. On the other hand, the values of V_{oc} were decreased by the post-annealing treatment, which agrees with what have been reported [87]. The optimized annealing temperature in our experiment was 150°C, in which both J_{sc} and PCE were increased, respectively, by 2.6 and 2.2 folds as compared to the non-annealed device. The R_S calculation for the post-annealed devices at 150°C revealed that the annealing treatment helped as well in decreasing the devices series resistance by ~ 1.2 fold. This, according to Eq. 2-2 explains the increase in the J_{sc} , and hence the enhancement in the overall efficiency.

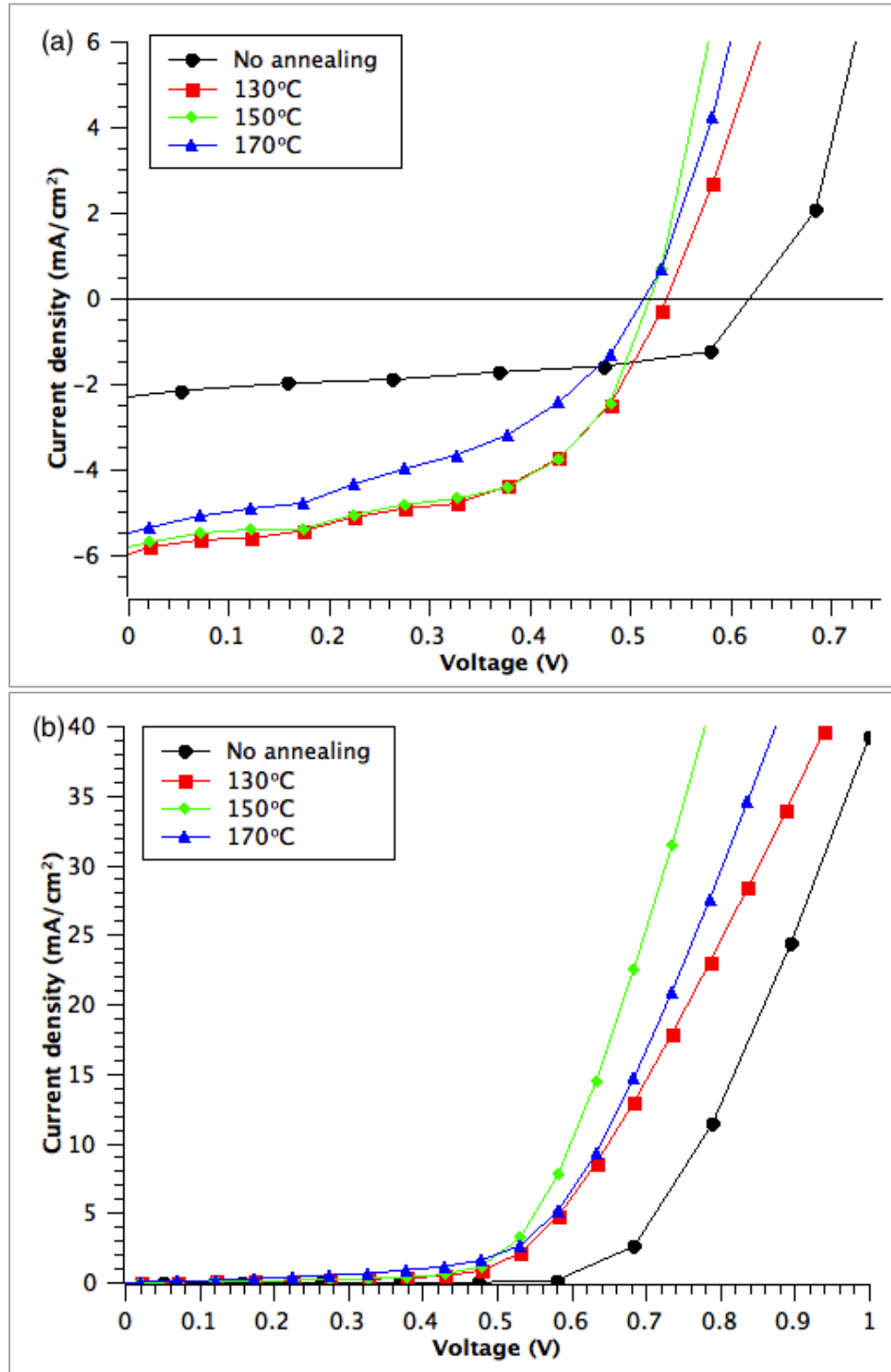


Figure 6. 4: The JV curves for reference device along with devices that were post-annealed at 130, 150 and 170°C for 30 min (a) Under illumination and; (b) In dark.

There is a relation between elevating the annealing temperature and the enhancement in the device performance. The surface of the P3HT:PCBM film becomes rougher as increasing the annealing temperature, which explains the enhancement in the PCE [43]. By elevating the temperature to higher degree, 170°C in our experiment, the enhancement in the PCE was reduced as compared to the devices that were annealed at 130 and 150°C. This reduction in the PCE could be due to the aggregation of the P3HT domains with increasing annealing temperature, which produced a phase separation between the P3HT and PCBM domains [85]. It is also reported that at higher annealing temperatures the surface roughness of the P3HT:PCBM film started to be smoothed out as compared to the one that was treated with a lower annealing temperature [43]. This point could also explain the reduction in the PCE by annealing our devices at 170°C.

6.3 Conclusion

We succeeded in fabricating efficient P3HT:PCBM organic solar cell devices by optimizing the thickness of LiF as well as the post-annealing temperature. The optimal LiF thickness in our experiment was observed to be ~ 0.6 nm, and the optimal post-annealing temperature was 150°C. Inserting the LiF interfacial layer played an enormous role for increasing the short circuit current, open circuit voltage, fill factor and power conversion efficiency. It helped as well in reducing the devices series resistance. Elevating the post-annealing temperature to 150°C helped in increasing both short circuit current and power conversion efficiency, while the open circuit voltage was decreased. By optimizing the LiF thickness and the post-annealing temperature we could successfully enhance the power conversion efficiency of our devices from 0.36% to

1.67%. Figure 6.5 illustrates the increase in the PCE of our devices during the optimization process.

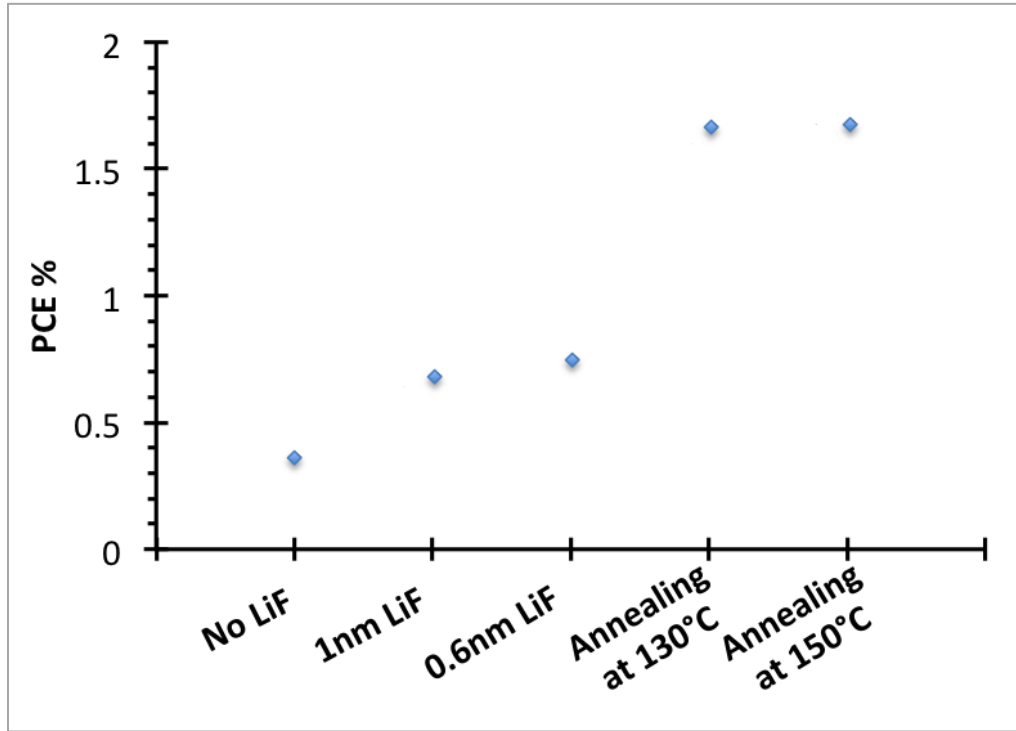


Figure 6. 5: The increase in the PCE of our OSC devices during the optimization process.

Although we optimized the fabrication parameters for our devices, a variation in the PCE% from sample to sample is an expected issue in the laboratory scale. Hence, we tried to minimize such variation by measuring various devices and taking the average.

In the next chapter, we present various approaches to insert gold nanorods in our devices, and the impact of that in the device performance.

CHAPTER VII

Gold Nanorods Incorporated into Polymer Solar Cells

This chapter presents our work of incorporating gold nanorods into various locations in the polymer solar cells devices. Gold nanorods were inserted either in contact with the front electrode of the cells, indium tin oxide, or with their back electrode, Al cathode, or by blending them with the solution of the anodic buffer layer, PEDOT:PSS, or with the solution of the photoactive one, P3HT:PCBM. The motivation behind using each approach is presented, followed by the procedures, results, discussions and conclusions.

7.1 Gold nanorods and P3HT:PCBM film characteristics

Gold nanorods in aqueous solution was synthesized and obtained from the Institut de la Recherche Scientifique at Varennes (INRS-EMT) following the colloidal seed-mediated, cetyltrimethylammonium bromide surfactant-assisted approach method reported in reference [88]. Details about the synthesis are presented in the thesis appendix. Figure 7.1 shows a transmission electron microscopy (TEM) image of the Au NRs, which reveals that the rods have an average aspect ratio of 4, in which the dimensions of the rods' long and short axes are 40 and 10 nm, respectively. To calculate the concentration of the Au NRs in the aqueous solution, the total elemental amount of the Au used in the synthesis was divided by the weight of one rod. The rod weight was calculated roughly by multiplying the density of Au with the volume of one Au rod

(cylinder). The result of this calculation gave the concentration of the Au NRs in the aqueous solution as $\sim 1.593 \times 10^{12}$ rods/ml.

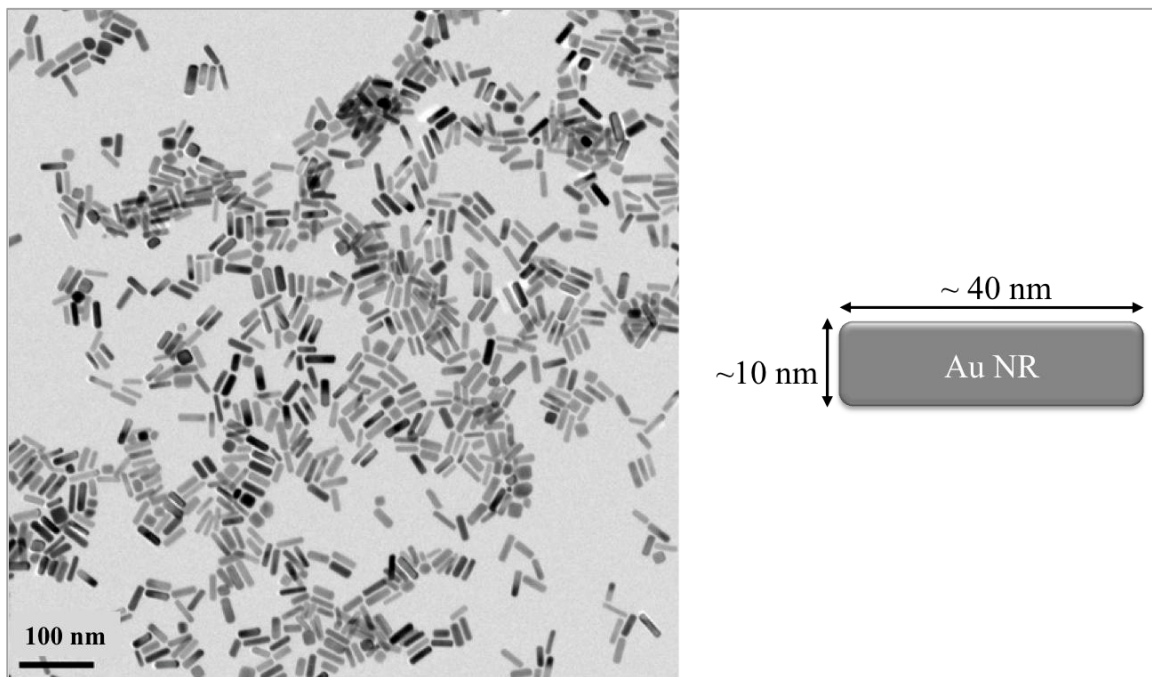


Figure 7. 1: A TEM image showing Au NRs on glass.

Figure 7.2 compares the absorption spectrum of the P3HT:PCBM film along with the resonance spectrum of Au NRs in solution. The red curve in figure 7.2 shows two plasmonic peaks, transverse and longitudinal, respectively at 520 nm and 715 nm for Au NRs. According to a theoretical study [83] for gold nanorods with an aspect ratio ~ 3 -5, their extinction is dominated by the scattering mechanism. However, the absorption also contributes to the total extinction of the rods.

The blue curve in figure 7.2 shows that the absorption of the photoactive film ranges from 370 nm to 650 nm, with an absorbance maximum around 518 nm and two shoulder peaks around 560 and 610 nm. This absorbance profile was due to the π - π^*

electronic transitions between 0-1 and 0-0 spin states for the maximum and the shoulder peaks, respectively [30,89].

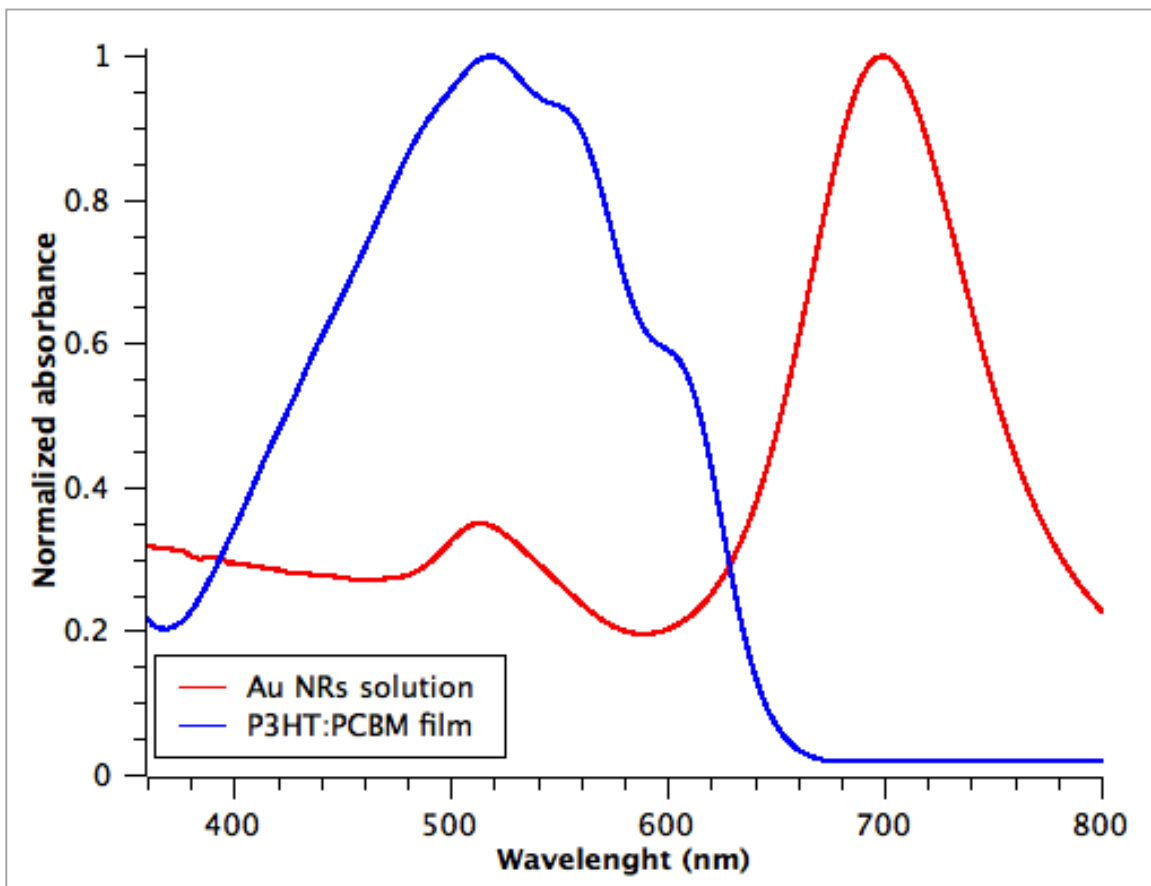


Figure 7. 2: The absorption modes of a P3HT:PCBM film (blue curve) and an Au NRs colloidal solution (red curve).

It is clear from figure 7.2 that the resonance peaks for Au NRs are situated at or near the absorption maximum of the P3HT:PCBM photoactive layer. Besides, the longitudinal peak of Au NRs is close to the IR absorption edge of the photoactive layer. Hence, we assume that by inserting the rods into various locations in our BHJ-OSCs, the intensified EM field around the NRs would reach the photoactive layer, and increase its

absorption near the plasmon peaks of the NRs, even though the total enhancement remains small near the IR wavelengths.

7.2 Depositing Au NRs in contact with the anodic ITO electrode

Motivation: in this approach, we aimed to study the effect of depositing Au NRs on top of the ITO-coated glass on the performance of our BHJ-OSC device. Figure 7.3 illustrates the position of the NRs in our fabricated OSCs. We wanted to observe the advantage of the forward scattering of the incident light by locating the NRs in such position. The presence of the rods in the photoactive film is assumed to increase the quenching energy states for the free charge carriers, which enhances their recombination, leading to a reduction in their numbers at electrodes [30,33]. In contrast, the light trapping mechanism via depositing the Au NRs on the anodic interface (ITO) is suggested to produce higher numbers of free charge carriers at electrodes, which would enhance the overall performance of the device. Hence, we expect that having the rods in such location is favorable as compared with embedding them in the photoactive layer.

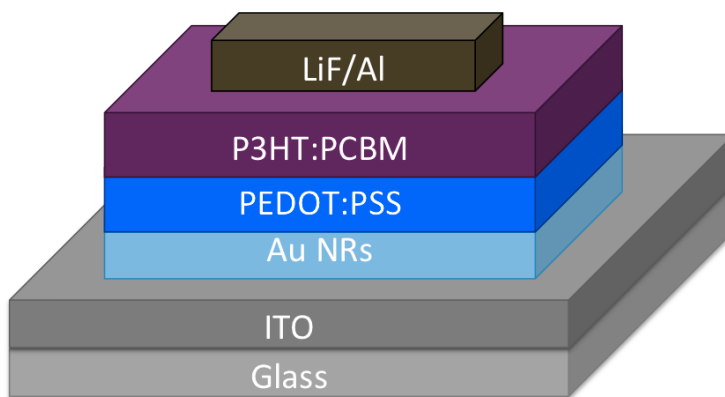


Figure 7. 3: Location of Au NRs on top of the anode electrode.

7.2.1 Procedures

OSC devices were fabricated following our previously mentioned procedures. After treating the ITO-coated glass with an oxygen plasma, Au NRs were deposited on top of ITO before spin-coating the PEDOT:PSS layer. To study the effect of changing the deposition way on the resulting Au NRs layer, and hence on the device overall performance, we deposited the rods with three different approaches illustrated in figure 7.4:

Spin-coating: in this approach, the spin-coating of the Au NRs solution was performed with a two-steps process, first at slow speed of 200 RPM for 3 sec with 1 sec to reach 110 RPM, then at 1000 RPM for 10 sec with 5 sec to reach 550 RPM. In order to study the effect of different concentrations of the rods on the OSC performance, one and five layers of Au NRs were examined.

Drop-casting: in this approach, the substrates were totally covered with drops of Au NRs colloidal solution.

Vertical deposition: in this approach, the substrates were placed vertically in the Au NRs colloidal solution for different periods of time.

After depositing the rods, substrates were then left to dry before spin-coating the PEDOT:PSS buffer layer. For each approach, the optical absorption of the resulting layers was measured using a UV-Vis spectrophotometer, and their surface structure was characterized using an SEM, in which the particles densities on the anodic layer were evaluated.

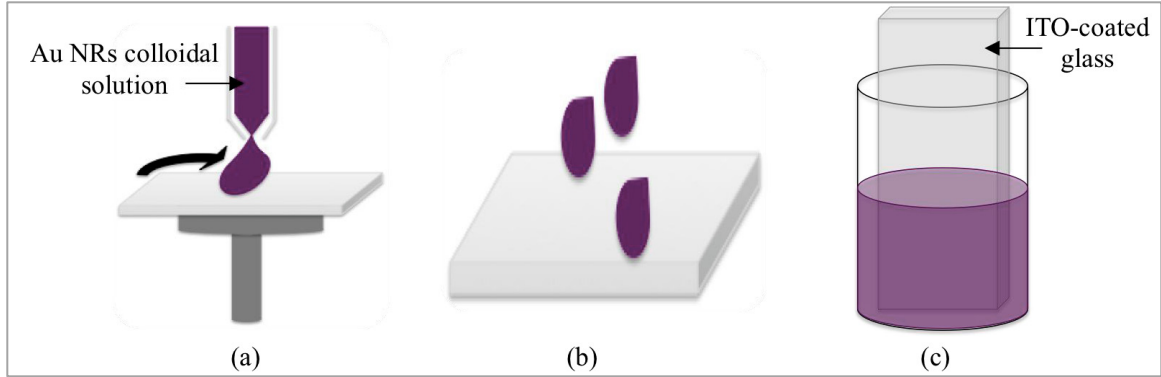


Figure 7. 4: Three approaches of depositing Au NRs on top of ITO-coated glass: (a) Spin-coating; (b) Drop-casting; and (c) Vertical deposition.

7.2.2 Results and discussions

The SEM images in figure 7.5 reveal that varying the deposition techniques of Au NRs on the ITO-coated glass resulted in different densities and alignments of the rods on the substrate. Accordingly, the spectral measurements of the Au NRs layers obtained, illustrated in figure 7.6a, show a noticeable difference in the plasmonic absorption peaks; the drop-casted particles shows two peaks, while a shoulder and a peak are found in the case of particles obtained by the vertical deposition method. A more intense peak is observed for the spin-coated deposit. The drop-casted and five layers spin-coated (images are not presented) Au NRs produced denser rods in the anodic layer ($\sim 4 \times 10^9 \text{ cm}^{-2}$) with nanorod long-axis alignments parallel and perpendicular to the substrate plane. The presence of Au NRs with the two different alignments at the surface explains the appearance of the two peaks in the spectrum. For one layer spin-coated rods, the rod long-axis alignment was mostly in the substrate plane (figure 7.5a), which supports the longitudinal resonance peak in the spectrum of figure 7.6a. In the case of vertically

deposited rods (figure 7.5c), additionally to the longitudinal resonance peak there is the transverse resonance mode, which indicates that some particles were aligned perpendicularly to the substrate plane. For vertically deposited and one layer spin-coated rods, the particles densities on the anodic layer were $\sim 6 \times 10^8 \text{ cm}^{-2}$ and $\sim 8 \times 10^8 \text{ cm}^{-2}$ respectively.

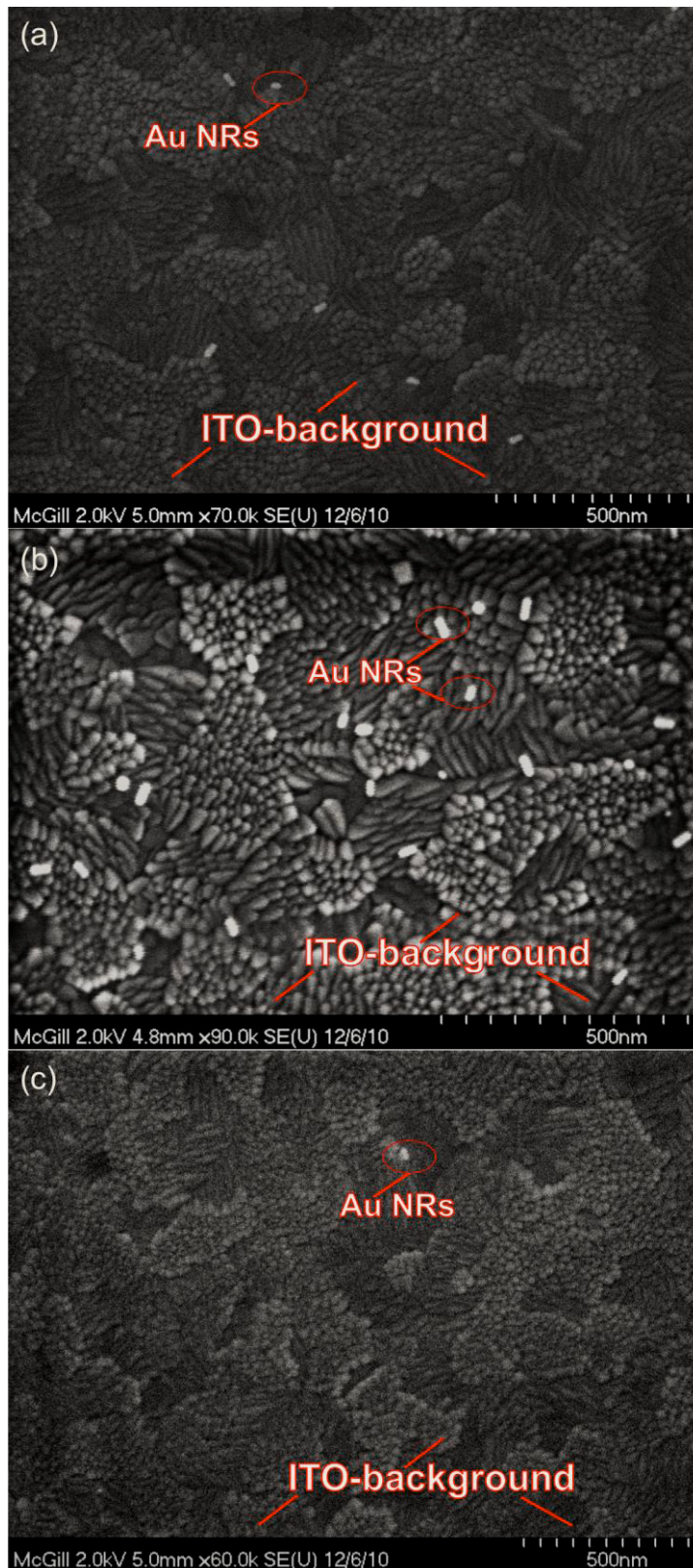


Figure 7. 5: SEM images for one layer of Au NRs deposited on ITO-coated glass using different methods: (a) Spin-coating; (b) Drop-casting; and (c) Vertical deposition.

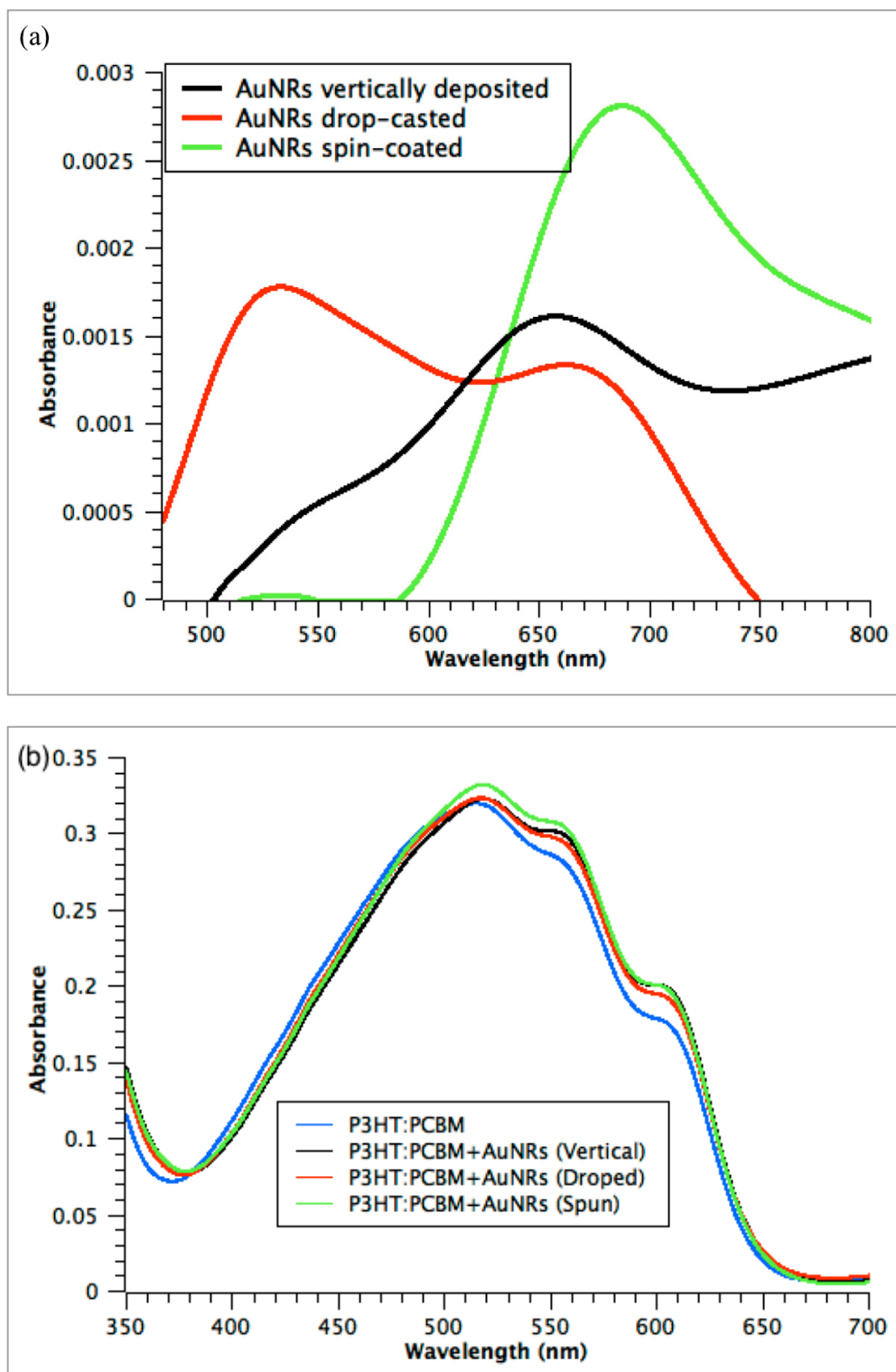


Figure 7. 6: (a) UV-Vis spectra for one layer of Au NRs deposited on top of ITO-coated glass with various deposition techniques; (b) A comparison between the optical density of P3HT:PCBM with and without Au NRs on the ITO-coated glass with different deposition techniques of the rods.

Figure 7.6b shows the optical density of the photoactive layer P3HT:PCBM on ITO-coated glass with and without incorporating the Au NRs plasmonic layer. Due to the match between the optical absorption of both plasmonic (500-700 nm) and P3HT:PCBM (380-660 nm), the addition of Au NRs increased the optical density for the photoactive layer up to ~11%, and the resulting absorption profile for AuNRs/P3HT:PCBM film was the same as that for the pristine one.

Figure 7.7 shows the JV characteristics, under illumination (7.7a) and in dark (7.7b) conditions, for solar cells made with and without Au NRs anodic layers under the same fabrication conditions. The PV parameters for those devices are summarized in table 4. From this table, we can observe that the addition of the plasmonic layer increased the J_{sc} for the OSC device in most cases, which in turn increased the PCE. This is in accordance with previously reported results for gold nanoparticles [27,29,30]. The enhancement in the PCE was 5% and 15.8% for one layer of Au NRs that was deposited using spin-coating and vertical deposition approaches, respectively. Nevertheless, solar cells having higher density of Au NRs, $\sim 4 \times 10^9 \text{ cm}^{-2}$, deposited either by drop-casting or by spin-casting of five layers of Au NRs on top of ITO-coated glass showed a slightly lower performance than control devices without Au NRs. In these cases, the efficiency was decreased by up to 2%.

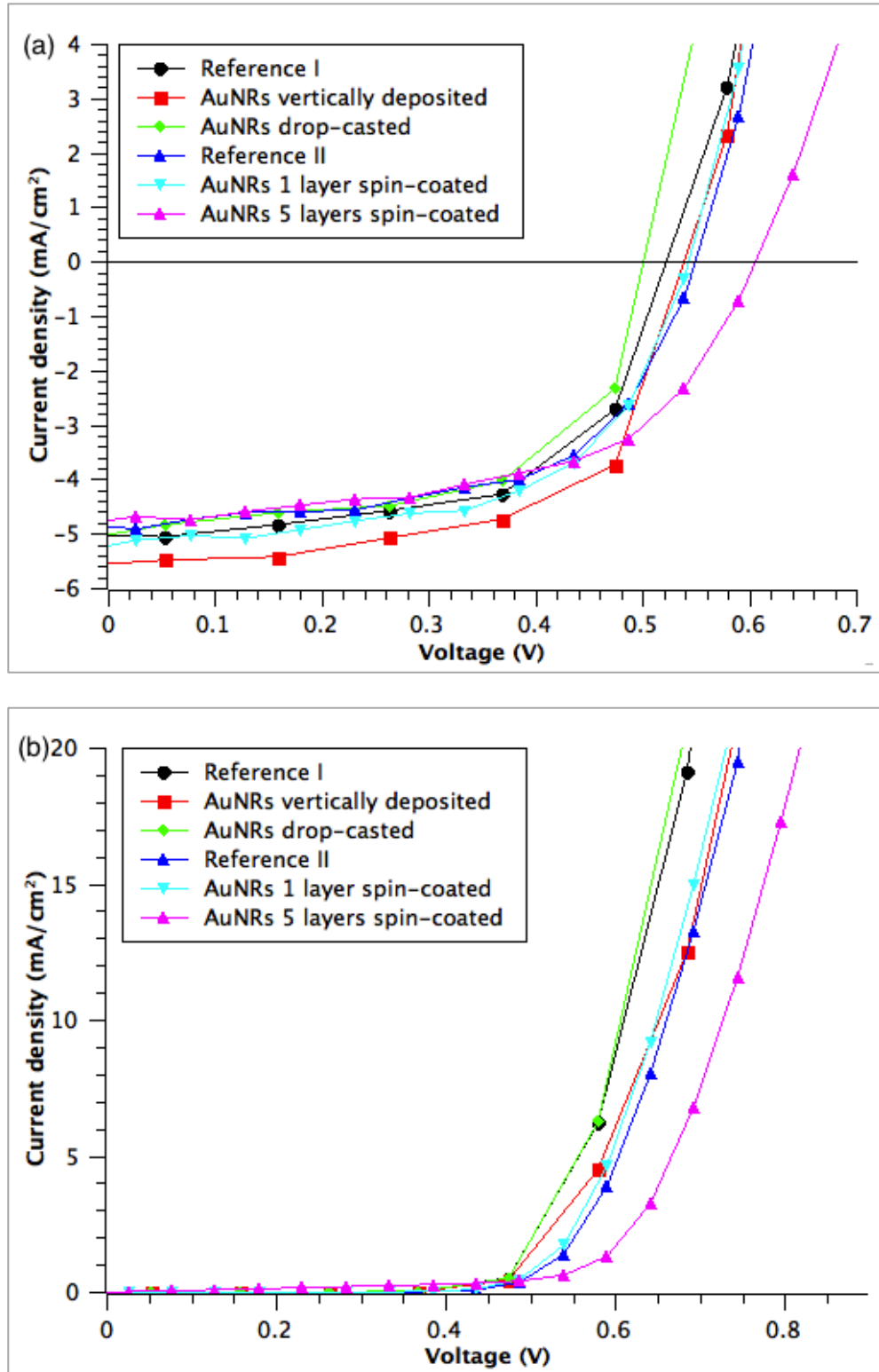


Figure 7. 7: The JV curves for devices without Au NRs (ITO/P3HT:PCBM/LiF/Al) and with Au NRs (ITO/AuNRs/P3HT:PCBM/LiF/Al) (a) Under illumination and; (b) In darkness.

Table 4: The PV parameters for pristine reference devices and devices in the presence of Au NRs on top of ITO-coated glass for different deposition methods.

Device type	Rods surface density/cm ²	V_{oc} (V)	J_{sc} (mA/cm ²)	FF%	PCE%	Enhancement
Reference I	-	0.52	-5.03	67.9	1.52	
Rods vertically deposited	$\sim 6 \times 10^8$	0.54	-5.56	69.0	1.76	+15.8%
Rods drop-casted	$\sim 4 \times 10^9$	0.50	-5.03	64.9	1.48	-2.0%
Reference II	-	0.55	-4.89	68.3	1.55	
Rods spin-coated-1 layer	$\sim 8 \times 10^8$	0.54	-5.35	66.9	1.62	+5.0%
Rods spin-coated-5 layers	$\sim 4 \times 10^9$	0.60	-4.72	63.4	1.54	-0.8%

As we found, Au NR layers that were produced by the vertical deposition method increased significantly the PCE of solar cells. Hence, we tried to maximize this effect by studying some deposition parameters, such as the deposition time, in this process. To study the effect of varying time on the vertical deposition method, rods were deposited respectively at 10, 30 and 50 min. The SEM images for those layers (not presented) show that a 50 min deposition period produced more particles ($\sim 8 \times 10^8 \text{ cm}^{-2}$) as compared to 10 and 30 min deposition periods where the particle density was observed to be $\sim 6 \times 10^8 \text{ cm}^{-2}$. The variation in the deposition time affected the absorption of the resulting layer too as demonstrated in figure 7.8.

Table 5 summarizes the obtained PV parameters of the solar cells made with those layers. Among the 10, 30 and 50 min deposition periods, the 30 min vertically deposited Au NRs produced the highest (18%) enhancement in the PCE. This increase of the efficiency is due to a 16.9% enhancement (from -4.48 to -5.24 mA/cm²) in the J_{sc} .

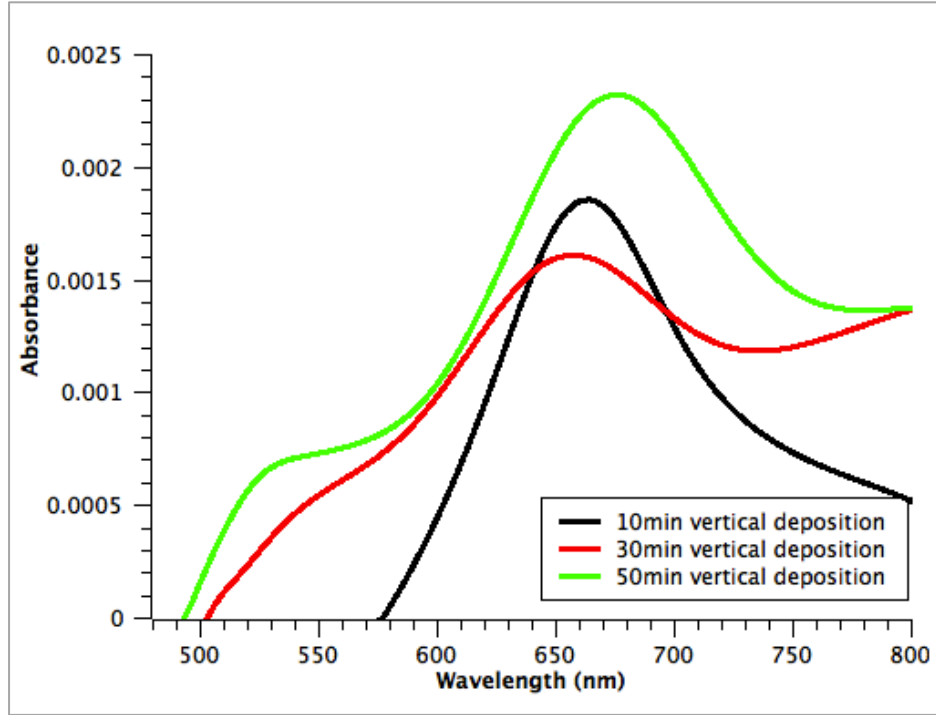


Figure 7. 8: UV-Vis spectra for Au NRs vertically deposited on ITO-coated glass with various periods.

Table 5: *The PV parameters for pristine reference devices and devices in the presence of Au NRs on top of ITO-coated glass for different Au NR vertical deposition times.*

Device type	Rods surface density/cm ²	V_{oc} (V)	J_{sc} (mA/cm ²)	FF%	PCE%	Enhancement
Reference I	-	0.57	-4.48	62.4	1.58	
10 min	$\sim 6 \times 10^8$	0.59	-4.60	65.8	1.79	+13%
30 min	$\sim 6 \times 10^8$	0.57	-5.24	62.4	1.85	+18%
Reference II	-	0.54	-5.03	64.3	1.75	
50 min	$\sim 8 \times 10^8$	0.54	-5.24	65.2	1.85	+3%

According to the Polman et. al. [9,69], the increase in the efficiency of our solar cells with incorporating Au NRs layer on top of the anodic ITO electrode could be related

to the far field effect of the Au NRs. Since the rods were placed at the interfaces of two mediums with different refractive indices, the forward scattered light toward the larger permittivity medium (P3HT:PCBM⁵) becomes favorable. Scattering of the incident light with an angle different than the normal one will result in an increase of its optical path length inside the photoactive layer, which leads to increase of its absorption of light. In addition, the Al cathode helps in reflecting the incident light back to the photoactive layer. Hence the incident light will be trapped inside the P3HT:PCBM layer, and coupled with the rods at the interface, then re-scattered again [9,26]. This enhanced absorption increases the photogeneration of excitons in the photoactive layer near the plasmon peak, which enlarges the J_{sc} and improves the PCE in general.

The decrease in the device efficiency via increasing Au NRs density in the anodic layer in the case of drop-casted and five layers spin-coated rods could be due to the increase in the destructive interference between the incident and reflected E fields, which decreased the intensity of the E field in the photoactive layer. This would affect the charge carriers generation process, and reduce the overall performance [9].

In this study, the PV parameters were determined at ± 5 % error and the superior enhancement in the PCE due to 30 min vertical deposition of Au NRs was reproducible. Yet, those results cannot be fully generalized as it depends on the concentration of Au NRs in the colloidal solution. However, a general trend for the increase in the PCE of organic solar cells can be envisioned. In addition, further investigations have to be done to study the effect of the surface treatment of the ITO-coated glass on the Au NRs deposition.

⁵ The refractive index of P3HT:PCBM is ~ 2 [106], which is larger than that of the PEDOT:PSS and ITO [47]

7.2.3 Conclusion

This experimental study demonstrated the influence, on the PV performance, of both density and alignment of Au NRs that were deposited on the anodic layer of an organic solar cell by three simple methods; the drop-casting, spin-coating and vertical deposition. Due to the plasmonic effect, gold nanorods with density $\sim 6 \times 10^8 \text{ cm}^{-2}$ produced by 30 min vertical deposition enhanced the power conversion efficiency by up to 18%. The forward scattered light via the presence of the rods on the anodic electrode helped in trapping the incident light inside the photoactive film, which enhanced the electric field and improved the photogeneration of excitons in the photoactive layer, leading to an efficient generation of charge carriers that increased the short circuit current by up to 16%. However, the results also suggest that a higher density of Au NRs does not necessarily lead to improvements in the overall efficiency in all cases. Results of this section were reported in [90].

7.3 Embedding Au NRs in PEDOT:PSS layer

Motivation: in this approach, we aimed to study the effect of embedding Au NRs in the anodic buffer layer (ABL), PEDOT:PSS, on the performance of our device. Figure 7.9 illustrates the position of the NRs in this approach. Since the ABL is located at the interfaces between ITO and photoactive layer, we expect that the effect of the rods' far field [9] and near field [26] will produce an enormous enhancement in the performance of our devices. Besides, Dunbar et. al. [91] reported that the enhancement in the device performance due to MNPs embedded in the OSCs layers is higher than that associated

with placing them near front/back electrodes. This is due to their additional role in reducing the device series resistance. In addition, embedding MNPs in the photoactive layer introduces quenching energy states for the excitons, which reduces the number of free charges carriers that are collected by electrodes [30,33]. Hence, introducing MNPs in the anodic buffer layer (ABL) of OSCs is favorable.

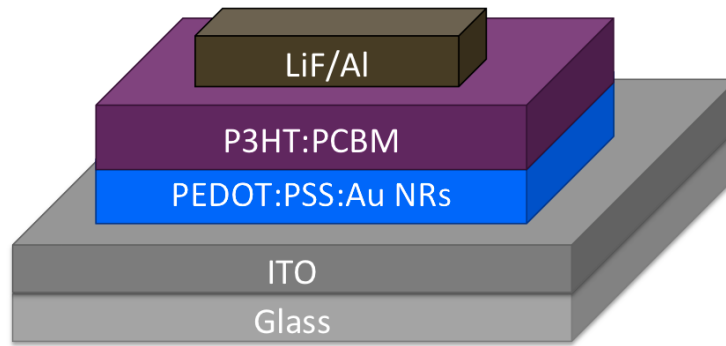


Figure 7. 9: OSC device structure with Au NRs embedded in the PEDOT:PSS layer.

7.3.1 Procedures

In order to prepare our modified anodic buffer layer, PEDOT:PSS: AuNRs, gold nanorods aqueous colloidal solution was mixed with the PEDOT:PSS aqueous solution. Before mixing the rods, PEDOT:PSS solution was passed through a $0.45 \mu\text{m}$ PVDF filter. The mixture PEDOT:PSS: AuNRs was made by adding determined volume-percentages of the Au NR solution (30, 15, 7.5%) to the PEDOT:PSS solution. In order to keep the concentration of the PEDOT:PSS constant in the final mixture, an additional volume of DI-water was added to the mixtures that have lower content of the Au NR solution as illustrated in figure 7.10. Using this modified solution, OSC devices were

fabricated following our previously mentioned procedures. The spin-coating of the PEDOT:PSS:AuNRs blend was performed through a three-steps process, first at slow speed of 200 RPM for 3 sec with 1 sec to reach 110 RPM, then at 1000 RPM for 10 sec with 5 sec to reach 550 RPM, and the final step was at 2000 RPM for 30 sec with 10 sec to reach 1100 RPM.

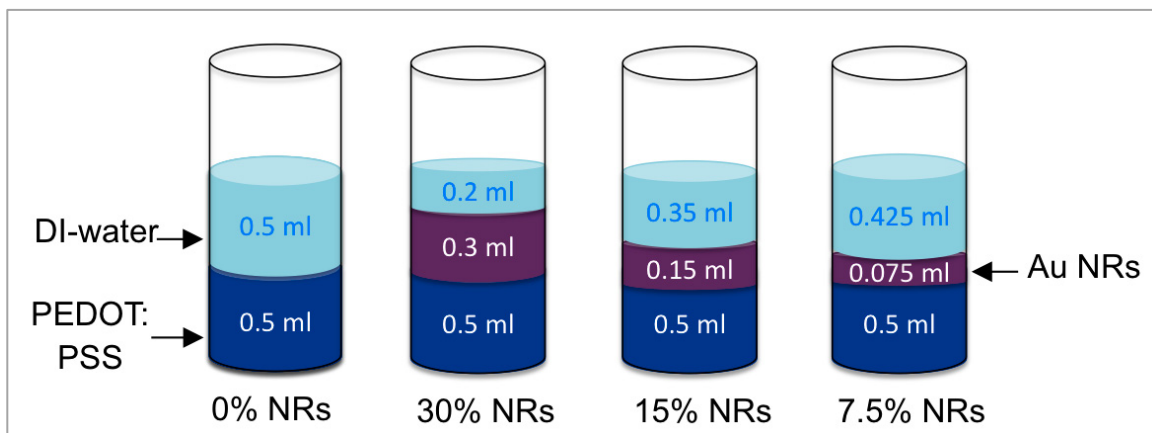


Figure 7. 10: Schematic representation of the Au NRs solution percentages that were mixed with the PEDOT:PSS solution.

7.3.2 Results and discussions

The results of our work in the following section have been recently published in [92]. In order to study the density and orientation of Au NRs in the PEDOT:PSS layer, SEM was made for the PEDOT:PSS:AuNRs spin-coated film. Figure 7.11 shows an SEM image for a film made using a 15% volume ratio of Au NR in the PEDOT:PSS solution. The white droplet-like structures in the SEM image are the Au NRs. From the uniformity of the PEDOT:PSS:AuNRs film, we can presume that the NRs did not aggregate after

being mixed with the PEDOT:PSS [24]. Furthermore, the orientations of Au NRs within the PEDOT:PSS film were arbitrary, and their density was very low.

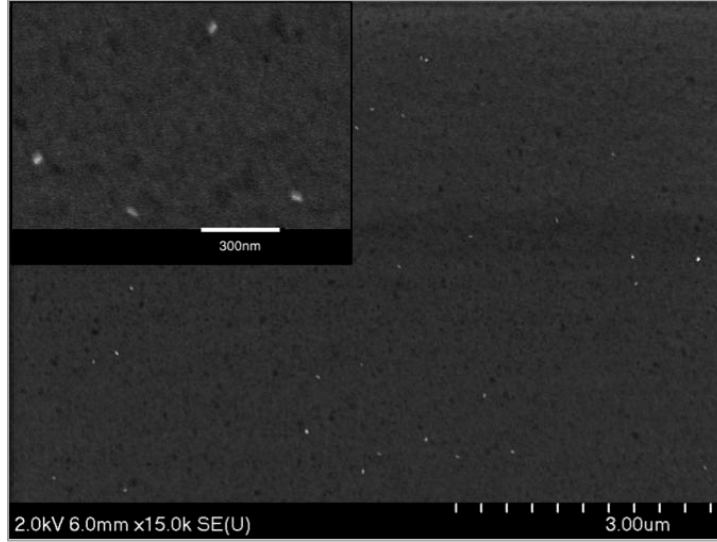


Figure 7. 11: An SEM micrograph of PEDOT:PSS:AuNRs film made with 15% of Au NRs solution in the PEDOT:PSS solution. The bar in the inset indicates 300 nm.

The JV curves under illumination and in dark conditions for reference device along with devices containing Au NRs in the ABL is presented in figure 7.12, and the PV parameters are summarized in table 6. It can be seen from table 6 that the 7% and 15% Au NRs devices showed an increase in both J_{sc} and PCE. The optimal value for the enhancement was observed from the 15% Au NRs devices, which has $\sim 2.38 \times 10^{11}$ rods/ml in the ABL solution. For these devices, we observed a clear enhancement in the J_{sc} from 6.6 to 7.7 mA/cm², which lead to an enhancement of about 21.3% in the PCE. We found such enhancement quite interesting considering the low density of the MNPs in the layer as compared to some reported studies in which the density of the particles was much higher [27,29,30]. The density of the NRs embedded in the buffer layer of our

samples was estimated from the SEM as $\sim 6 - 8 \times 10^8$ rods/cm². Although the cited references did not give the density of the nanoparticles (of other shapes) in the layer, their SEM images showed that their density would indeed be much larger than ours.

Table 6: *The average PV parameters for reference and PEDOT:PSS: AuNRs devices. The standard deviation is calculated for all parameters.*

Device type	V_{oc} (V)	J_{sc} (mA/cm ²)	R_s (Ω cm ²)	FF%	PCE%
Reference-no Au NRs	0.55	-6.67 ± 0.05	18.3 ± 2.4	53.9	1.97 ± 0.11
30% Au NRs	0.54	-6.26 ± 0.35	11.7 ± 1.7	54.9	1.99 ± 0.10
15% Au NRs	0.59	-7.70 ± 0.25	11.9 ± 3.5	53.6	2.39 ± 0.02
7.5% Au NRs	0.57	-6.67 ± 0.43	13.3 ± 4.6	54.2	1.94 ± 0.06

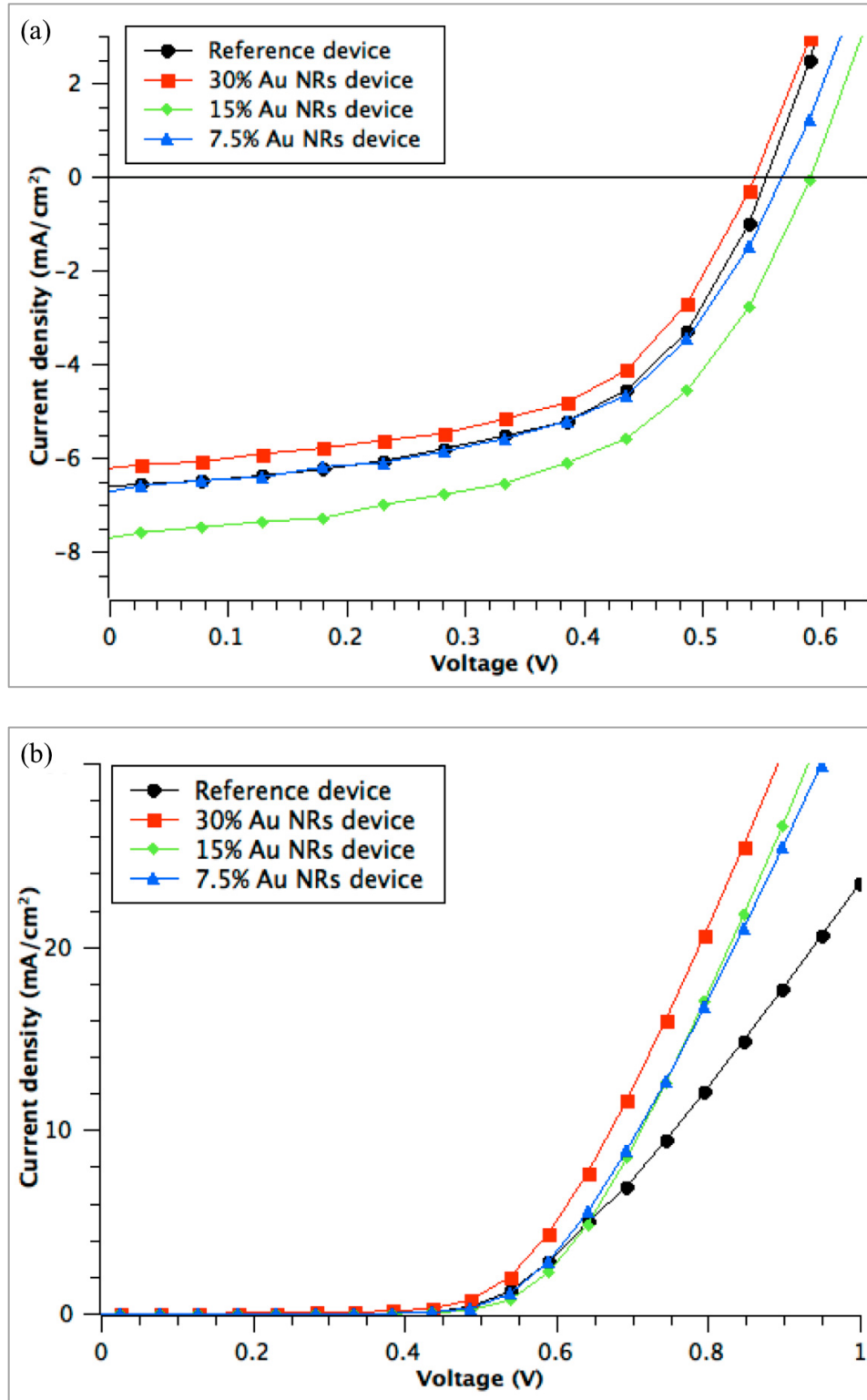


Figure 7.12: The JV curves for reference device along with devices incorporating Au NRs in the PEDOT:PSS layer (a) Under illumination and; (b) In dark.

In order to determine whether the enhanced performance in our devices was indeed related to the plasmonic effect, we performed a comparative study between the absorbance of P3HT:PCBM film made with different conditions: pristine-thick, pristine-thin and thick P3HT:PCBM film with Au NRs. Figure 7.13a shows the absorbance profile of the resulting films: the brown-○ curve corresponds to thick P3HT:PCBM: AuNRs (film I), the green-◇ curve corresponds to thick P3HT:PCBM (film II) and the blue-△ curve corresponds to the thin P3HT:PCBM (film III). The change in the P3HT:PCBM thicknesses was achieved by varying the spin-coater speed (RPM) from 1000 to 1500 for thick and thin films, respectively.

As figure 7.13a shows, while the absorbance shapes of the three films are similar, the absorbance intensity varied and the highest one was associated with the Au NRs incorporated film. Due to the similarity in the absorbance shapes of those films, the multi-modes excitation-dependent for the film with Au NRs was not obvious. However, a clear plasmonic-related shape appeared by comparing the increase in the absorbance between films I and II (red-× curve) along with the one between films II and III (black + curve). Differences in the absorbance of films made at different conditions: (thick pristine film – thin pristine film) and (thick NR incorporated film - thick pristine film) gave the spectra shown in the inset of figure 7.13a. The increase in the thickness of pristine P3HT:PCBM film shows a maximum around 480 nm. In contrast, Au NRs on the photoactive layer produced a peak maximum around 560 nm and two shoulder peaks around 518 and 610 nm.

From figure 7.13b, the enhancement in the absorbance at 518 is related to the transverse mode of the NRs, while the enhancement at 560 and 610 could be linked to the

tail of the longitudinal mode of the NRs. From these peaks and shoulders, we could conclude that both modes of Au NRs are active here. Hence the observed differences in the absorption shapes between films I, II and III would link the enhancement in the P3HT:PCBM absorption to the multi-modes excitation in Au NRs.

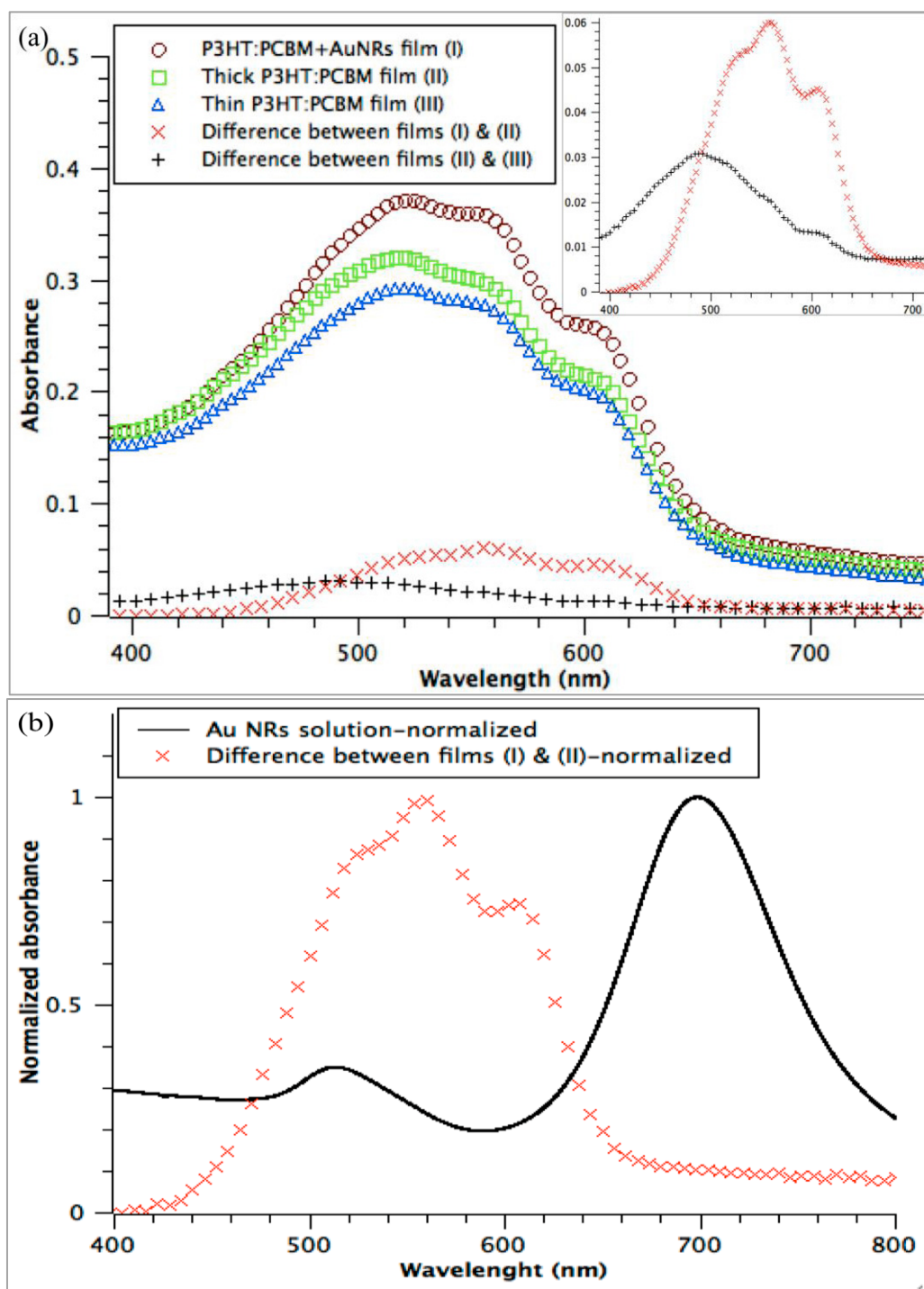


Figure 7. 13: (a) A comparison between the absorption profiles of the P3HT:PCBM films made with three different conditions: thick-pristine (green- \diamond), thin-pristine (blue - Δ), and thick with AuNRs spin-coated on top of it (brown- \circ). The difference between the absorbance of thick and thin films is presented by the black-+ curve, and the difference between the absorbance of pristine and Au NRs film is presented by the red- \times one. The inset shows the absorbance of both black-+ and red- \times profiles alone; (b) A comparison between the absorption spectra of Au NRs solution and the difference between films (I) & (II).

Figure 7.14a illustrates the external quantum efficiency measurements for reference device along with the 15% Au NRs one. To show that the enhancement in the J_{sc} was dependent on the multi-modes excitation of Au NRs, we investigated in Fig. 7.14b the increase in the EQE via incorporating the 15% Au NRs in ABL solution. We found that the EQE was enhanced by up to 12-14% respectively around 520-640 nm, which are near to the transverse absorption mode of Au NRs and the tail of the longitudinal one, respectively. These enhancements in the EQE with incorporating Au NRs are higher than what is reported in the literature [24], showing the advantage of using Au NRs over other shapes of the nanoparticles. Although there was no large enhancement in the absorption profile of P3HT:PCBM:AuNRs near the IR region, a very small increase in the EQE was observed at this region, particularly at 670-700nm, which can be attributed to the longitudinal absorption mode of Au NRs. From this scenario, it is suggested that the photogeneration of excitons near the transverse and longitudinal absorption modes of Au NRs was enhanced, which improved the total device efficiency. Our EQE results are somewhat different from those obtained by Morfa and Rowlen [27] who reported on enhancements in organic cells incorporating Ag nanoparticles. These authors observed a decrease in enhancement near 450 nm where Ag NPs absorb and an increase in the red part of the spectrum. Other groups however reported results similar to ours with the EQE curves for both reference and NPs devices having the same absorption ranges with a slight enhancement in the tail near the IR region [24,30,31].

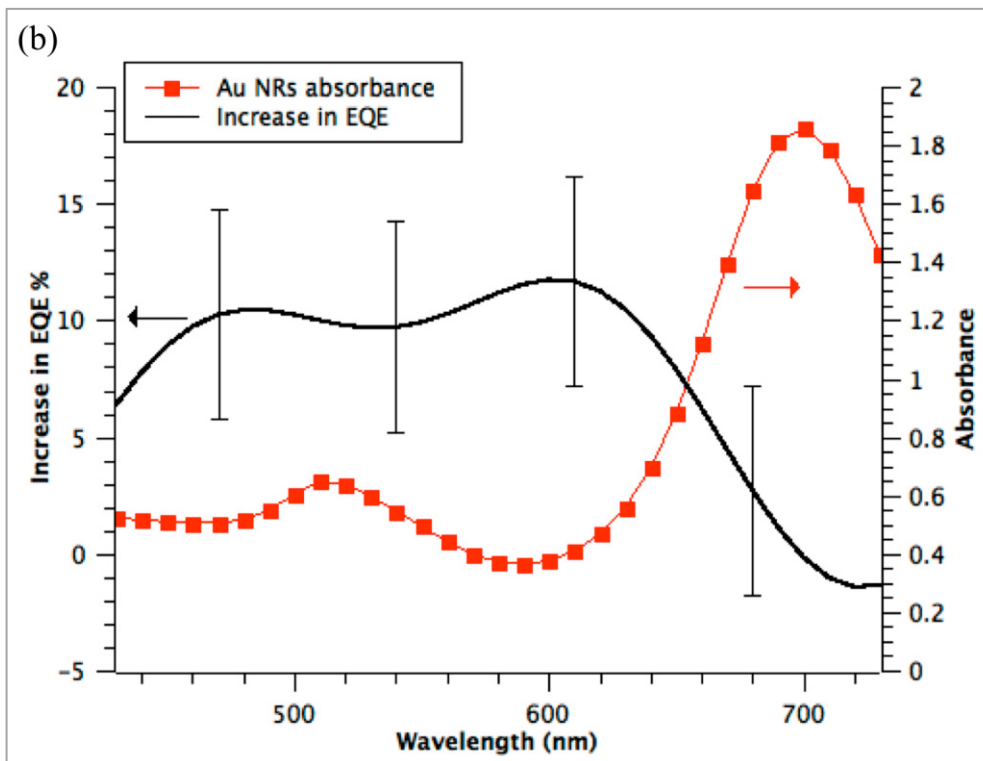
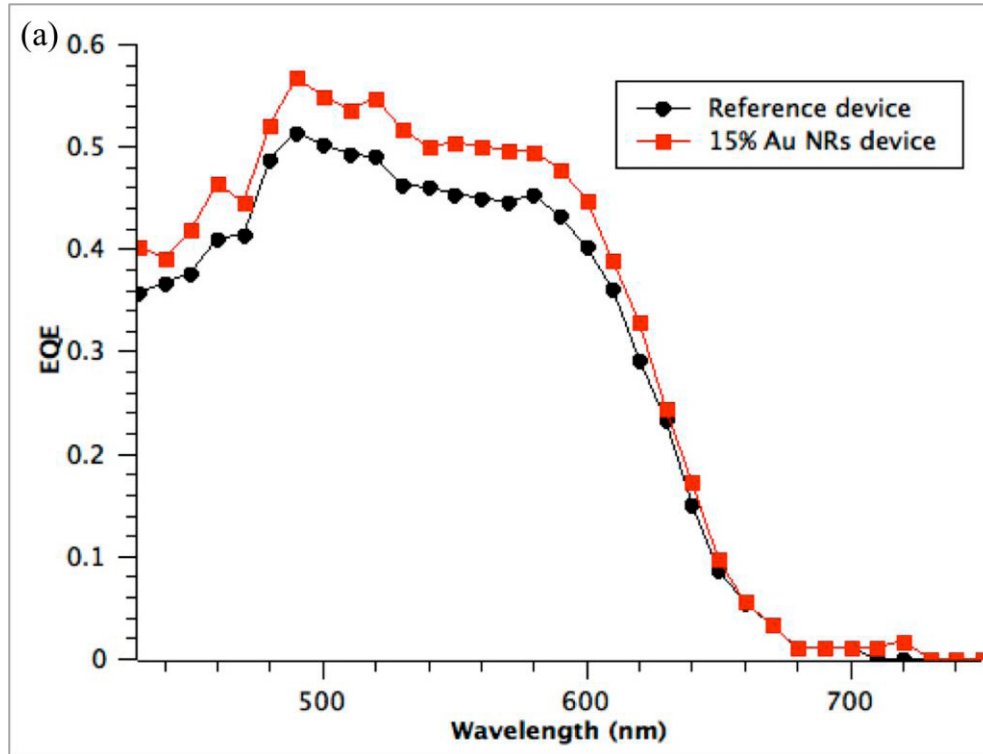


Figure 7. 14: (a) The EQE spectral response for reference device along with the 15% Au NRs one; (b) The increase in the EQE with 15% Au NRs device along with the absorbance of the Au NRs solution. The curve has been smoothed and the bars indicate the errors.

We would expect that the LSPR will enhance the local EM field near the MNPs, thereby intensifying the light that passed through the P3HT:PCBM layer. It is also possible that Au NRs helped trapping the incident light in the photoactive layer via forward scattering mechanism. Thereby, the number of the photogenerated excitons inside the photoactive layer would be increased [29,33], which would then increase the number of the free charge carriers that were collected by electrodes. This would explain the enhancement in the devices J_{sc} , and the improvement in the PCE.

For denser Au NRs in the buffer layer, 30% devices, as listed in table 6, the values for both V_{oc} and J_{sc} were lower than the ones for the reference device. Since the thickness of ABL was ~ 30 nm, comparable to the long axis of the NRs, and the NRs orientations were arbitrary in that layer, a higher density of Au NRs would tend to have the rods located at the interface, touching the photoactive layer. Therefore, we would expect that most of the photogenerated excitons near the ALB/P3HT:PCBM interface to be subjected to recombination processes. Hence, the number of free charge carriers that reached electrodes would be lowered, thus reducing both V_{oc} and J_{sc} [23]. It is also possible that the larger density of NRs would prevent some light from reaching the photoactive layer [31].

Table 6 also shows that by embedding Au NRs in the PEDOT:PSS layer, the devices series resistance R_S was reduced by up to 36%, which contributed to the total enhancement in the PCE. Au NRs in the PEDOT:PSS layer reduced the volume of the PEDOT:PSS, which lowered the value of R_S , and diminished the interfaces that holes had to travel through to reach the anode. This would facilitate the movement of holes toward the anode [33]. As figure 7.15 indicates, the reduction in the R_S could also be due to the

work function of Au NRs, ~ -5.1 eV [33], that matches very well with both the polymer HOMO level and the PEDOT:PSS work function. With that scenario, Au NRs in the ABL would act as a hole-conductor interface, leading to a better extraction of the holes after being dissociated from the excitons. This would result in an increase in the number of free holes reaching the ITO-interface [33].

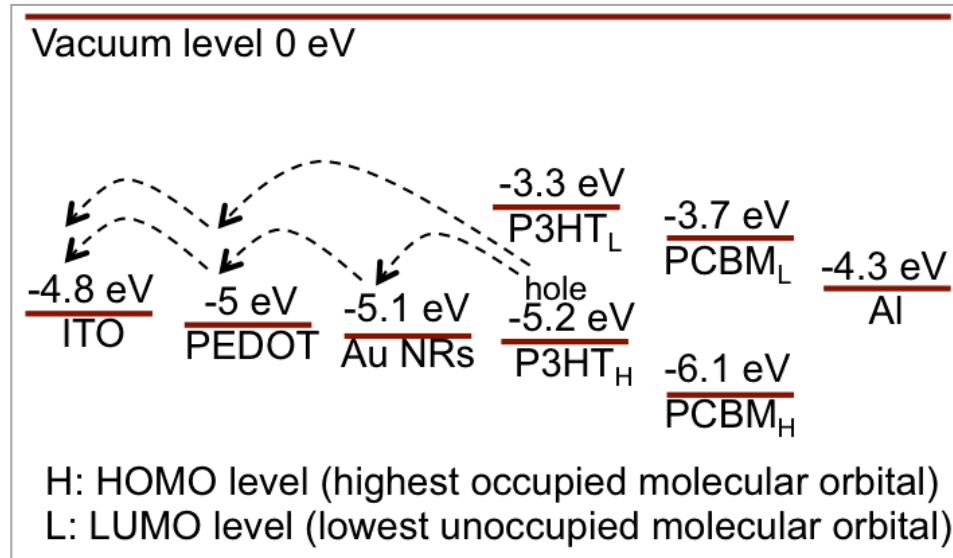


Figure 7. 15: The energy band diagram of the used materials showing the good match of the Au NRs work-function with the HOMO of the polymer (P3HT_H) and the work-function of PEDOT:PSS.

7.3.3 Conclusion

An enhancement in the PCE of polymer solar cells by up to 21% has been achieved by fabricating OSCs that contained Au NRs embedded in the PEDOT:PSS layer. The investigation of the absorption profiles of devices with/without Au NRs revealed that the multi-modes excitations of LSPR in Au NRs, even with a low density of Au NRs, were able to intensify the light that reached the photoactive layer, and increase

the number of the free charge carriers, which enhanced the J_{sc} by up to 16.7%. In addition, the presence of Au NRs in the anodic buffer layer produced a significant reduction in the device series resistance by up to 36%, which lead to a better collection of the charge carriers. This reduction contributed to the total enhancement in the device performance. Higher densities of Au NRs in the PEDOT:PSS layer were however found to reduce the overall performance of OSCs. Such reduction in the PCE could be related to the surface recombination of charge carriers that limited their numbers reaching the electrodes, or the fact that a large part of the incident light was prevented from reaching the photoactive layer for a potential generation of excitons.

7.4 Mixing Au NRs with P3HT:PCBM layer

Motivation: in this approach, we aimed to study the effect of mixing Au NRs with the solution of the photoactive layer on the performance of our device. The effect of embedding MNPs into the photoactive layer of BHJ-OSCs are rarely studied experimentally since the MNPs are usually available in aqueous solutions, which hinders them from being directly mixed with the organic one that is for the photoactive solution. Some reported works [26,91] revealed that the enhancement in the light absorption of OSCs due to embedding of the MNPs in their photoactive films is higher than that associated with placing them in contact with the cells' front/back electrodes. In addition, photoactive layers spin-coated from different concentrations of the polymer:fullerene solutions showed different morphologies in the resulting films, which significantly influences the device performance [93]. Hence, we aimed here to investigate the effect of

mixing gold nanorods with two different concentrations of the P3HT:PCBM solutions on the overall performance of the devices. We expect that having the NRs embedded in the photoactive layer will result in immediate excitation of the adjacent excitons because of the direct effect of LSPR surrounding them [26], which would result in more generation of excitons and in turn produce better devices. In addition, having the rods embedded in the photoactive layer is supposed to reduce the devices series resistance [33]. The reduction in R_S would also contribute to the total enhancement of the device performance. Figure 7.16 illustrates the position of the NRs in our fabricated OSC.

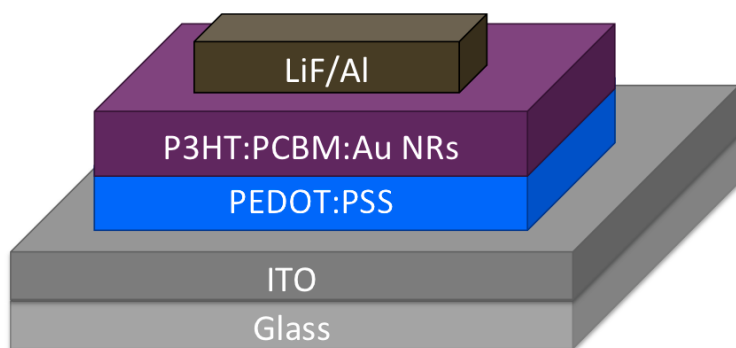


Figure 7. 16: OSC device structure with Au NRs embedded in the P3HT:PCBM photoactive layer.

7.4.1 Procedures

In order to be able to mix the Au NRs aqueous solution with the solvent based P3HT:PCBM one, Au NRs in the aqueous solution were transferred into a toluene-based solution one. Details about the phase transfer process are presented in the appendix. For preparing the photoactive mixture, first P3HT:PCBM (20 mg/ml-polymer) solution was prepared as previously mentioned and stirred overnight inside the glove-box. Solution

was then passed through a 0.45 μm PTFE filter. Afterward, the toluene-based gold nanorods solution was mixed with the pre-filtered P3HT:PCBM solution with determined volume-percentages (5, 2.5, 1.25wt%) of the Au NR solution. In order to keep the concentration of the P3HT:PCBM constant in the final mixture, an additional volume of 1,2-dichlorobenzene was added to the mixtures that have lower contents of Au NR solution. Figure 7.17 presents the volume percentages of Au NRs, P3HT:PCBM, and 1,2-dichlorobenzene solutions that were used in our experiment.

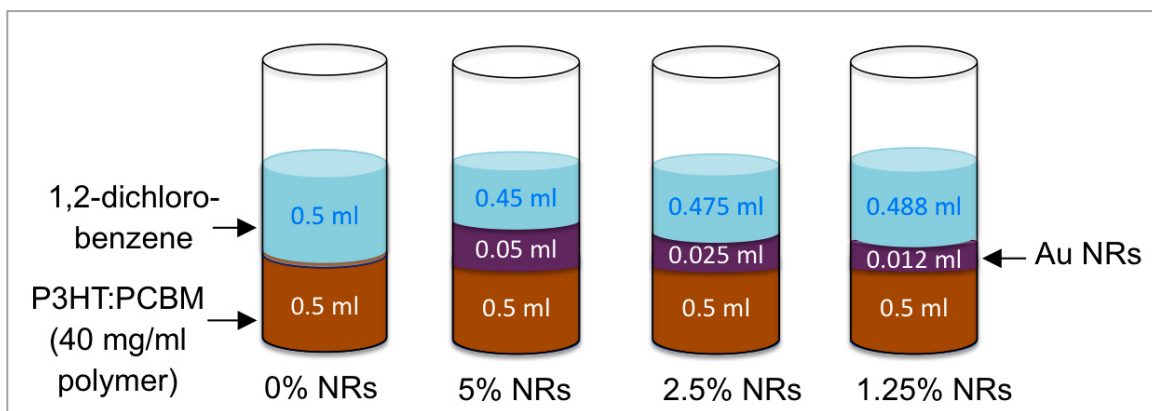


Figure 7. 17: Schematic representations of the volume percentages of Au NRs, P3HT:PCBM, and 1,2-dichlorobenzene that were used in our experiment for preparing the P3HT:PCBM: AuNRs solutions.

We chose such low percentages of the Au NRs in the photoactive solutions particularly to keep the morphology of the resulting photoactive film flat by introducing low concentration of the nanorods in the film [94]. In addition, we noticed from our previous works [90,92] that higher density of the rods in the layer lowered the photovoltaic performance. Using this modified P3HT:PCBM: AuNRs solution, OSC devices were fabricated following our previously mentioned procedures. The final

configurations of the reference device and the NRs one were, respectively,
Glass/ITO/PEDOT:PSS/P3HT:PCBM:/LiF/Al and
Glass/ITO/PEDOT:PSS/P3HT:PCBM: AuNRs/LiF/Al.

7.4.2 Results and discussions

The results of our work in the following section have been recently accepted for publication in Solar Energy Materials & Solar Cells journal. Figure 7.18 shows an SEM image for the synthesized toluene-based Au NRs that were spin-coated on an ITO-coated glass. It is clear that spin-coating of the rods solution produced rods with arbitrary orientations in the layer.

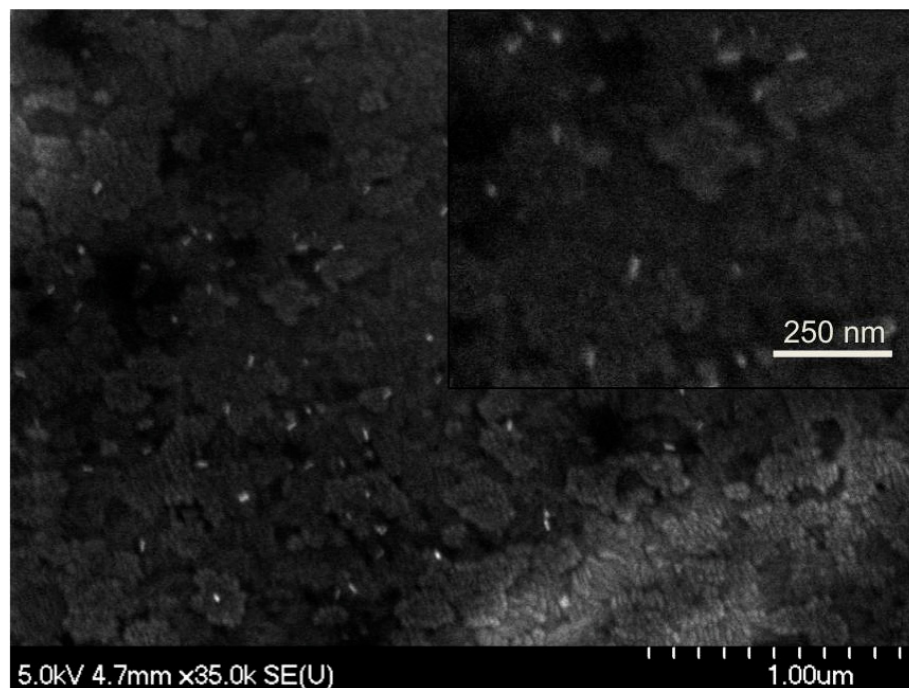


Figure 7. 18: SEM image showing the toluene-based Au NRs on ITO-coated glass. The white droplet-like structures indicate the rods.

To study the effect of changing the dispersion solvent of Au NRs on their absorbance of light, optical measurements were performed. Figure 7.19 illustrates the normalized absorption spectra for the toluene-based Au NRs and the water-based one along with the spectra of the P3HT:PCBM film. The black curve shows that the shapes of both transverse and longitudinal absorption peaks of the toluene-based Au NRs (respectively located at 540 nm and 740 nm) were broadened and red-shifted as compared to the corresponding ones in the water-based solution. The green curve shows that the absorption of the photoactive film ranges from 370 nm to 650 nm, with maxima around 518 nm and two shoulder peaks around 560 and 610 nm. It is clear that the transverse absorption peak of toluene-based Au NRs is situated near to the absorption maximum of the P3HT:PCBM. Besides, the longitudinal peak of Au NRs (~740 nm) is close to the IR absorption edge of the photoactive film. Hence, the intensified EM field around Au NRs is expected to increase the absorption of the photoactive film near the plasmon peaks of the NRs, even though the total enhancement remains small near the IR wavelengths.

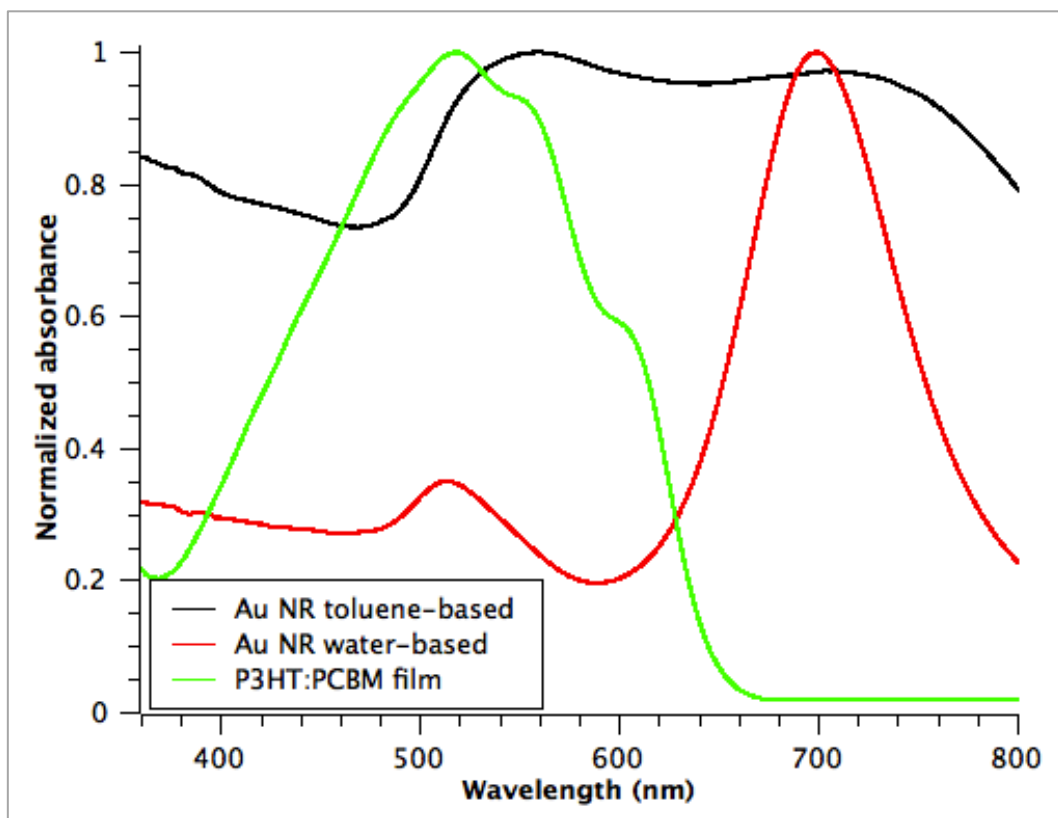


Figure 7. 19: Spectra comparison between Au NRs toluene based and water based solutions along with the spectra of P3HT:PCBM film.

To examine the effect of incorporating toluene-based solutions of Au NRs into the photoactive layer of the OSC devices, the PV parameters of fully fabricated devices with/without rods were measured and compared. Figure 7.20 illustrates the JV curves under illumination and in dark conditions for reference device along with devices containing Au NRs embedded in the photoactive layer, and table 7 summarizes their corresponding PV parameters. It is noticeable from table 7 that while the V_{oc} remained constant via embedding different densities of Au NRs in the photoactive layer of the OSC devices, the J_{sc} increased in all cases. For the 5 wt% Au NRs devices, both J_{sc} and PCE showed an increase by 13.4% and 6.5%, respectively. We would expect that such an

increase is due to the intensification of the EM field inside the P3HT:PCBM layer [95]. It is clear from table 7 that a higher increase in the J_{sc} was associated with a higher density of the rods in the layer. This indeed indicates that the LSPR enhances the local EM field surrounding the rods, and increases the number of photogenerated excitons inside the photoactive layer [29,33,95], which generates more charge carriers and hence enlarges the J_{sc} . This generation of charge carriers is related to the electronic transition probability, which is proportional to the strength of the E^2 field in the molecule [96]. The enlargement in the J_{sc} indicates that the LSPR helped in enhancing the mobility of the charge as well [94,97].

Table 7: The average PV parameters for reference and P3HT:PCBM: AuNRs devices, and the corresponding standard deviation.

Device type	V_{oc} (V)	J_{sc} (mA/cm ²)	R_S (Ω cm ²)	FF%	PCE%
Reference-no Au NRs	0.54	-4.64 ± 0.09	9.76	60.7	1.53 ± 0.01
5.0% Au NRs	0.54	-5.26 ± 0.05	7.41	56.7	1.63 ± 0.01
2.5% Au NRs	0.54	-5.18 ± 0.10	6.34	57.2	1.61 ± 0.01
1.25% Au NRs	0.54	-5.12 ± 0.06	12.9	54.4	1.53 ± 0.01

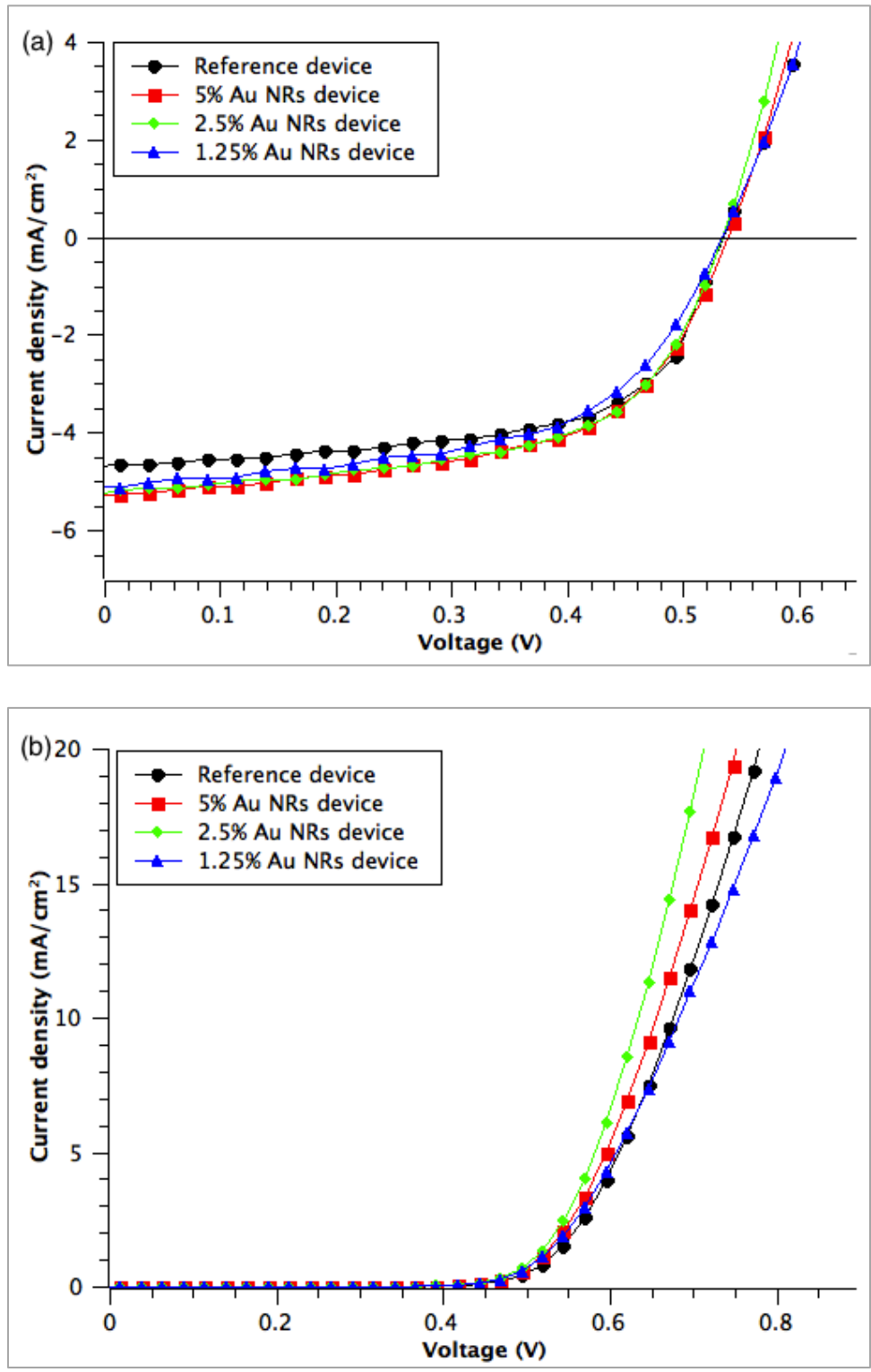


Figure 7. 20: The *JV* curves for reference device along with devices incorporating Au NRs in the photoactive layer (a) Under illumination and; (b) In dark.

It is also noticeable from table 7 that embedding Au NRs in the photoactive layer results in a decrease in the devices series resistance by up to 24%, which contributes to the total enhancement in the PCE. In theory, the reduction in the device series resistance leads to better device performance [44]. Hence, embedding the rods in the photoactive layer helped in reducing the P3HT:PCBM volume, which lowered the value of R_S , and diminished the interfaces that charge carriers had to travel through to reach both electrodes. This thereby facilitated the movement of the free charge carriers toward the electrodes [33]. Although devices made with lower density of rods in the photoactive layer, 1.25 wt% Au NRs case, showed ~10% increase in the J_{sc} , the overall PCE of the resulting device did not increase. We expect that the enhanced EM field in this case was not enough for more generation of charge carriers, which did not affect the PCE of the devices.

Since the 5 wt% of Au NRs solution in P3HT:PCBM solution produced better devices, we fabricated another set of devices with a slight increase in the volume percentage of the Au NRs, to 6.25 wt%, in P3HT:PCBM solution. This time, we aimed to study the effect of incorporating such percentage of Au NRs into two different thicknesses of the photoactive layer. To do so, we prepared P3HT:PCBM blends with two different concentrations of polymer in the final blend, 10 mg/ml and 20 mg/ml respectively. The percentage of Au NRs in the final photoactive blend was 6.25 wt% in both cases. Figure 7.21 presents the volume percentages of Au NRs, P3HT:PCBM, and 1,2-dichlorobenzene solutions that were used in this approach. The P3HT:PCBM:AuNRs mixtures were then spin-coated at 1000 RPM for 60 sec. Deposition by spin-coating using different concentrations of photoactive solutions produced P3HT:PCBM:AuNRs

films with two different thicknesses; thick films (~100 nm) that resulted from the use of 20 mg/ml concentrated polymer blend, and thin film (~40 nm) which corresponds to the usage of the diluted blend (10 mg/ml polymer). The thickness of the resulted layers was measured using AFM. For both concentrations, reference devices without Au nanorods were made and compared with devices containing nanorods.

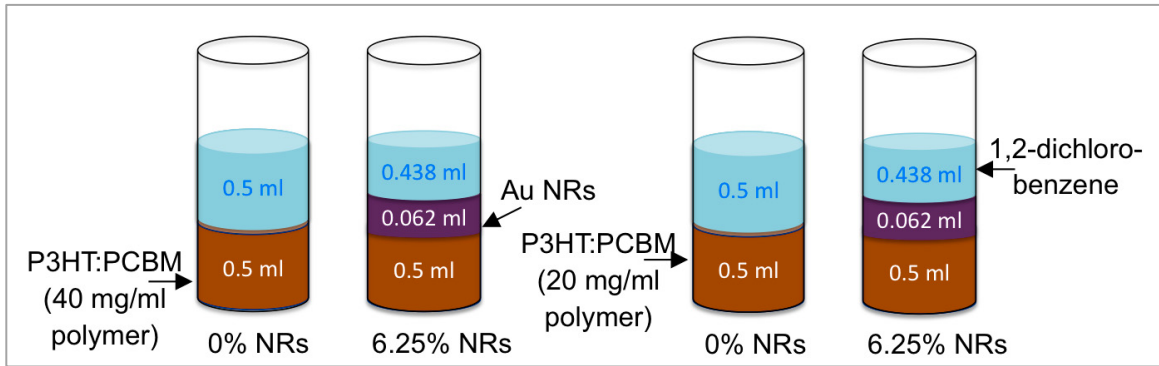


Figure 7. 21: Schematic representations of the volume percentages of Au NRs, P3HT:PCBM, and 1,2-dichlorobenzene that were used in preparing the P3HT:PCBM: AuNRs thin/thick films.

To study the effect, on the devices performance, of embedding Au NRs with same densities into thick/thin photoactive layer, the JV characteristics were measured for those devices under illumination and in dark conditions. The electrical characterization results are shown on figure 7.22, and their corresponding PV parameters are summarized in table 8. As table 8 shows, the J_{sc} was increased in both thick and thin devices by the percentage of 4.5 and 33.2, respectively. This indeed indicates that the LSPR around Au NRs helped in increasing the electric field of the incident light in the surrounding material, P3HT:PCBM, which resulted in more photogeneration of excitons in the photoactive

layer [9,95], and then a higher short circuit current. Table 8 also reveals that devices with a thin photoactive layer showed an enhancement up to 27% in the PCE when incorporating Au NRs. However, there was a slight decrease in the PCE for devices made of rods incorporated into the thick photoactive layer. It is also noticeable that for thin/thin photoactive films incorporated with Au NRs, the value of V_{oc} is decreased. This was not the case in the former set of experiments on thick devices made with 5, 2.5 and 1.25 wt% of rods in the active blend. The decrease in V_{oc} in the current experiment indicates that denser rods in the photoactive film affect the organic/metallic interface [24].

Table 8: *The average PV parameters for reference and P3HT:PCBM:AuNRs devices for thick and thin P3HT:PCBM layer, and the corresponding standard deviation.*

Device type	V_{oc} (V)	J_{sc} (mA/cm ²)	R_S (Ω cm ²)	FF%	PCE%
Thin active layer-no rods	0.52	-1.90 ± 0.01	8.33	59.8	0.591 ± 0.001
Thin active layer + 6.25% rods	0.50	-2.53 ± 0.02	9.09	59.9	0.751 ± 0.003
Thick active layer-no rods	0.55	-4.40 ± 0.02	5.88	57.1	1.461 ± 0.006
Thick active layer + 6.25% rods	0.50	-4.60 ± 0.04	7.14	57.6	1.301 ± 0.005

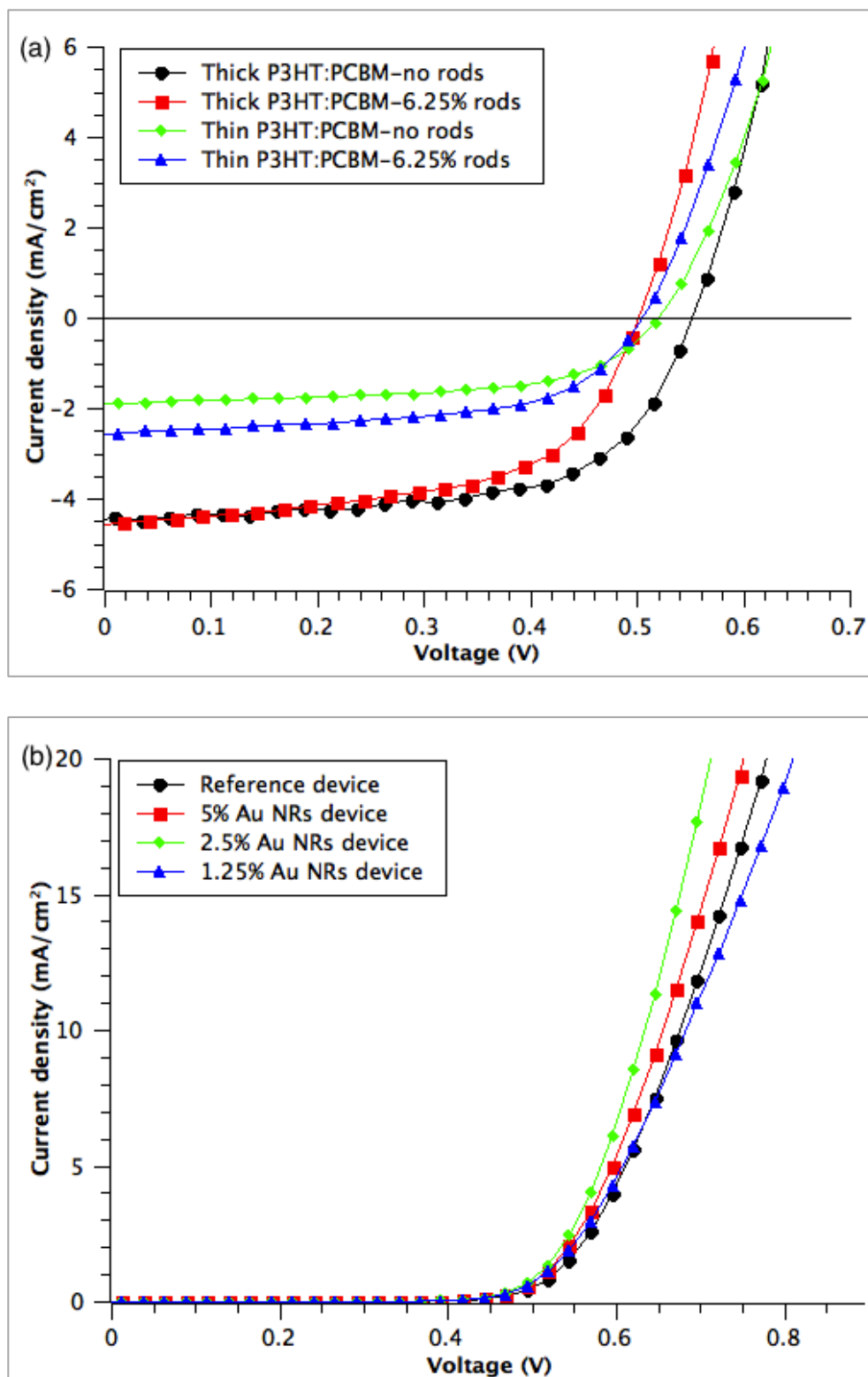


Figure 7. 22: The JV curves for reference thick/thin P3HT:PCBM devices along with devices incorporating 6.25% Au NRs in the photoactive layer (a) Under illumination and; (b) In dark.

To explain the difference in the increase in the J_{sc} for OSC devices made of thick/thin P3HT:PCBM:AuNRs film, spectroscopic measurements were performed for pristine thick/thin P3HT:PCBM films along with their corresponding films incorporating Au NRs. Figure 7.23a illustrates the absorption profiles for those films, and figure 7.23b illustrates the percentage of the increase in the absorbance of both thick/thin photoactive films after incorporating the rods. It is clear from figure 7.23a that while the shape of the absorption curves did not change after incorporating the rods, the absorption intensity of the photoactive films was increased. Figure 7.23a also shows that the absorption profiles of thin film with/without rods are red-shifted as compared with the thick one. This indeed indicates that the morphology of both spin-coated films was changed with changing thickness [93]. Since the concentrated polymer solution exhibits more aggregation than the diluted one, the resulted densely packed polymer chain films lead to a blue-shift in the spectra [93]. Figure 7.23b reveals that the rapid increase in the films absorbance after incorporating the Au NRs takes place between 500-700 nm, which is near to the transverse and longitudinal absorption peaks of the Au NRs (at 540 nm and 740 nm, respectively). This in fact indicates that the two absorption modes of the Au NRs are active here. It is also noticeable from figure 7.23b that the nanorods effect on the thin photoactive films is higher than the effect in the thick one although both films were incorporated with the same density of the Au NRs. To illustrate further this point, we calculated, in table 9, the area under the absorbance curves of figure 7.23a for thin/thick films with/without gold nanorods. We found that the increase in absorbance of the thin film via incorporating the rods was 12% higher than the corresponding one of thick film. This could be due to the fact that the thick film has a more aggregated photoactive layer

as compared to the thin one, which results in more quenching energy states for charge carriers [93]. It is also possible that changing in the morphology of the thick/thin films would result in different reflection response of the incident light for both films, which would influence their absorption response [98]. Since each film is characterized with different absorptivity response to the incident light, the change in the generated J_{sc} for both thick/thin OSC devices incorporated with Au NRs is understandable. This change indeed affects the PV behavior of the resulting devices.

Table 9: *The area under the absorbance curves, figure 7.24a, of thin/thick films with/without Au NRs nanorods.*

		Area under the absorbance curve (a.u.) ²	Increase in the area under the absorbance curve
Thin photoactive film	Without rods	34.72	22.8%
	With rods	42.64	
Thick photoactive film	Without rods	63.99	10.8%
	With rods	71.74	

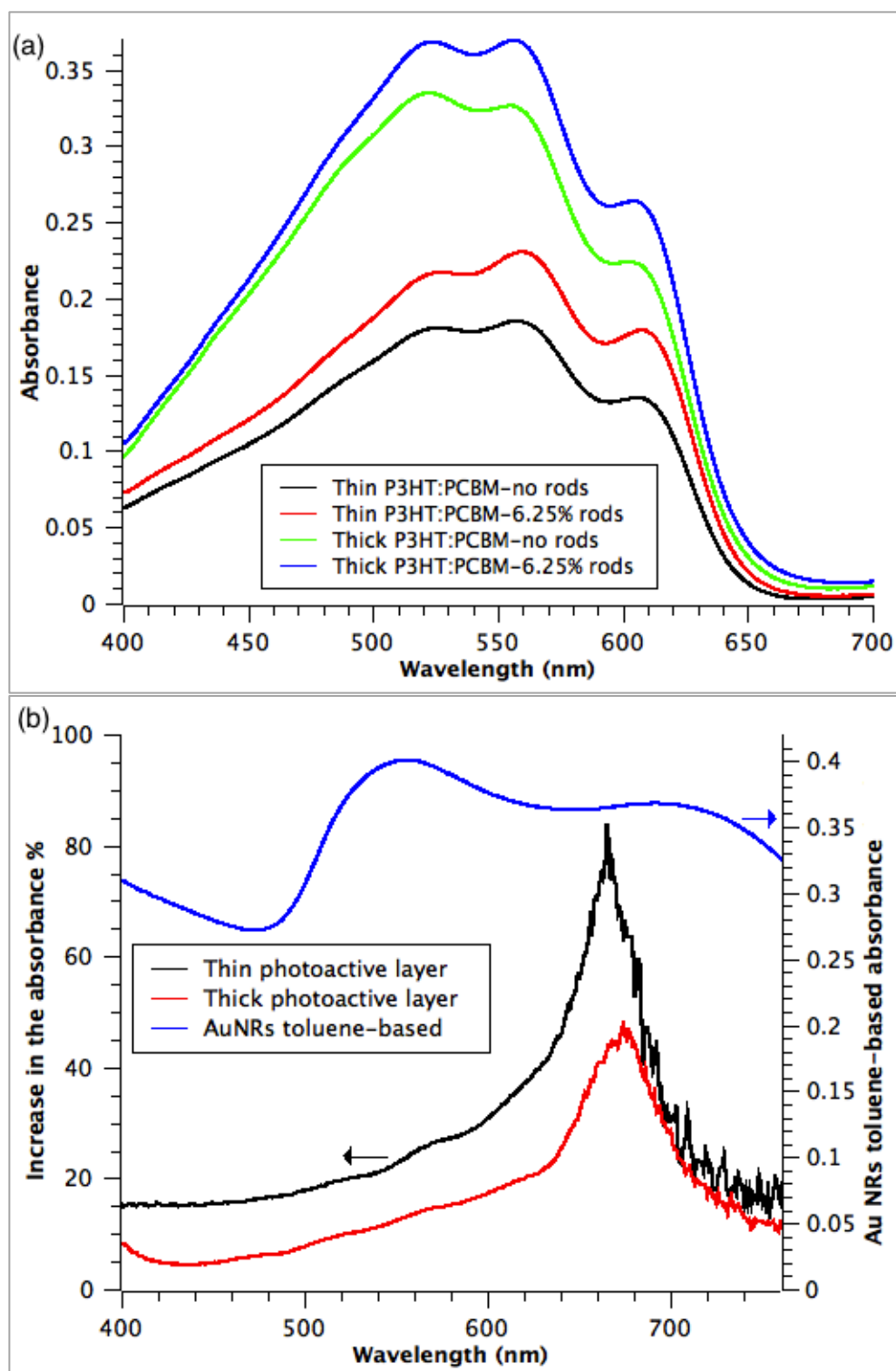


Figure 7. 23: (a) A comparison between the absorption of pristine thick/thin photoactive layer along with the corresponding ones that contain Au NRs; (b) The increase in the absorbance of the thick/thin films after incorporating Au NRs along with the NR toluene-based spectra. It is clear that the influence of the rods on the thin photoactive film is larger than that in the thick one.

In order to investigate more about the morphology of the examined thick/thin films, AFM scanning, figure 7.24, was performed, which showed that the addition of the rods in the photoactive films resulted in a change in their morphology. It seems that embedding the rods in the photoactive film created a phase-separation of the rods from the materials of the photoactive film [97]. This separation is more obvious in the case of thick photoactive film as compared to the thin one. As a consequence of such separation, charge carriers are most likely trapped inside the rods' network. Hence, their dissociation would be hindered, which reduces their numbers at electrodes. It is also noticeable from the AFM images that the stacking orders of the thick-pristine P3HT:PCBM film does not look similar to the one in thin-pristine film. The change in the morphologies between thick/thin P3HT:PCBM: AuNRs could also explain the difference in the absorbance response for both films to the incident light via incorporating the rods. Table 8 also shows that the R_s of devices made with thick/thin P3HT:PCBM: AuNRs film was increased with incorporating the rods. This suggests that the enhancement in the performance of thin devices was mainly due the LSPR associated with the rods [31].

We suggest that embedding Au NRs in the thick P3HT:PCBM layer creates more quenching energy states, as compared with the thin one, which trap the free charge carriers, and serve as recombination centers [97]. This in turn prevents the free charge carriers from reaching electrodes, and hence from contributing in the photovoltaic effect, which reduces the overall efficiency of the device. Since the thickness of the thick photoactive layer, ~100 nm, is much larger than the exciton diffusion length, the charge carriers need to travel through a relatively longer distance to reach the electrodes as compared with the case of the thin 40 nm film. This indeed increases the possibility for

the free charge carriers of getting trapped by the presence of the rods in the case of thick photoactive film. Hence the leakage current due to the recombination of the free charge carriers is more obvious in the case of thick OSC devices.

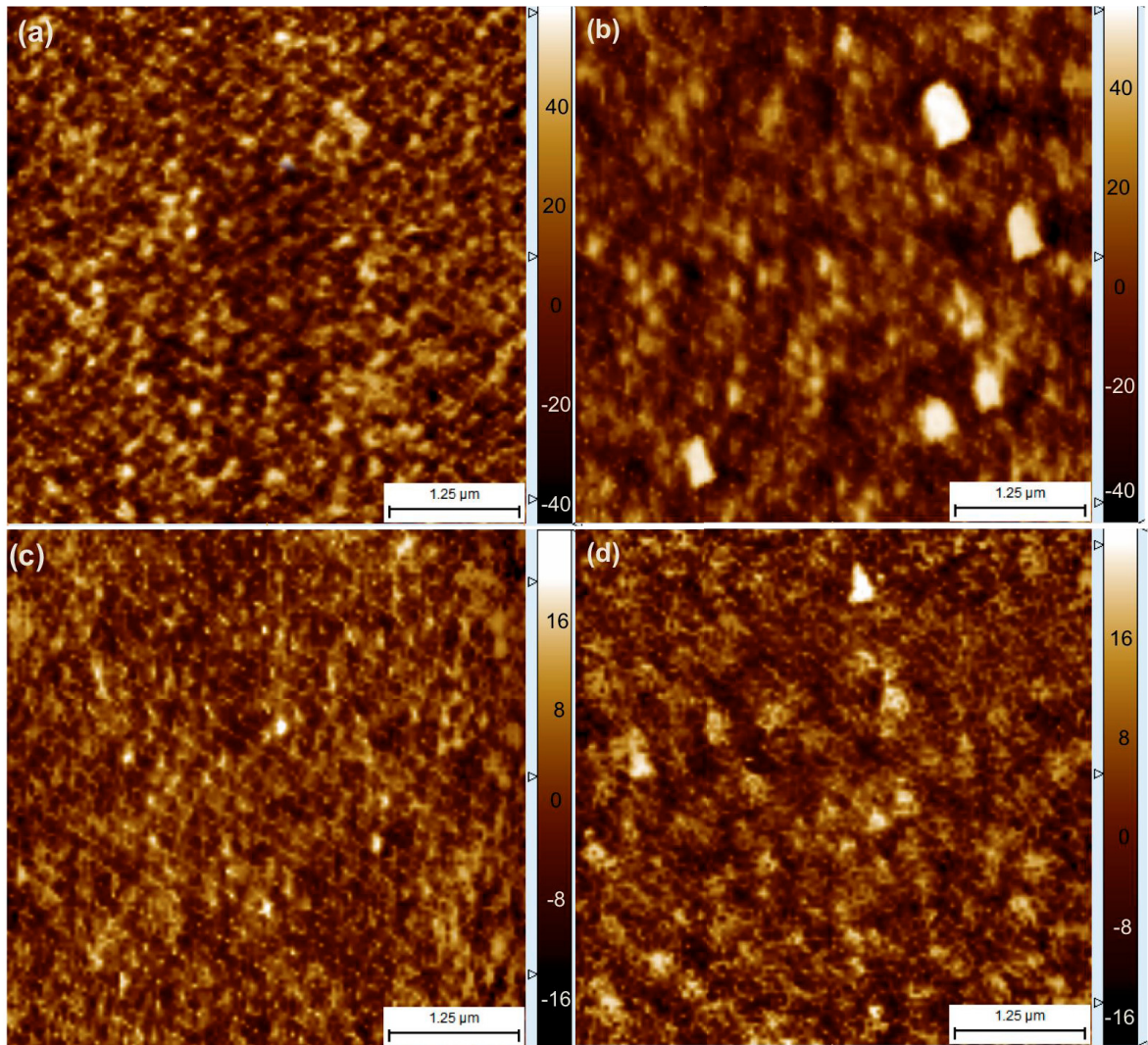


Figure 7. 24: AFM micrographs for (a) Thick P3HT:PCBM film; (b) Thick P3HT:PCBM:AuNRs film; (c) Thin P3HT:PCBM film; and (d) Thin P3HT:PCBM:AuNRs film. The bars indicate 1.25 microns. While the surface roughness of the films, ~ 1.4 nm, did not change after incorporating the rods, the morphology of the films changed for both cases.

To have a clear picture about the resulted leakage current in thick/thin devices, we calculated the shunt resistance R_{SH} for both thick/thin devices by measuring the inverse of the slope of the JV curves under illumination condition at 0.1 V. Interestingly, the R_{SH} for devices made of thin photoactive film was $\sim 1.26 \text{ k}\Omega \text{ cm}^2$, which was much higher than $0.56 \text{ k}\Omega \text{ cm}^2$ that is associated with devices made of thick photoactive film. This explains the high value of the FF for the thin P3HT:PCBM device as compared with the thick one. The decrease in the R_{SH} with increasing the thickness of the photoactive layer indicates that there are more leakage current and recombination of the free charge carriers in the case of thick OSC devices [51]. This point indeed supports our suggestion that the thick P3HT:PCBM: AuNRs devices have more recombination of the free charge carriers that resulted from the quenching energy states associated with the presence of the rods in the photoactive film. Such recombination increases the leakage current and reduces the overall efficiency of the device.

7.4.3 Conclusion

We experimentally studied the dependence in the efficiency of polymer solar cells, incorporated with 6.25 wt% gold nanorods in their active solution, on the thickness of their photoactive films. While the power conversion efficiency of devices made with thin photoactive layers, $\sim 40 \text{ nm}$, was enhanced by 27% with incorporating the rods, its value was slightly decreased in devices made of thick photoactive layers, $\sim 100 \text{ nm}$. The optical spectral investigations on thin/thick photoactive films with/without gold nanorods revealed that the multi-modes excitations of LSPR in gold nanorods embedded in our devices were active in both cases of thin/thick films. The comparison between the optical

measurements of thin/thick photoactive films with/without gold nanorods showed that the absorptivity of the thin film incorporated with the rods was 12% higher than that of the thick one. Incorporating the rods in the thin photoactive films enlarged their short circuit current by 28.6% as compared with the thick film case. This enlargement is related to the increase in both numbers and mobilities of charge carriers due to the effect of the induced LSPR via the presence of the rods in the layer. The surface morphology comparison of thin/thick films with/without rods revealed that the morphology of thick films was different from the thin ones. Comparison between shunt resistances of thick/thin devices incorporated with the rods showed that the thin devices have a shunt resistance that is higher than the one in thick devices by 2.25 fold. The changing in the morphology besides the reduction in the shunt resistances of devices made with thick films suggested that their leakage current was increased by the presence of the gold nanorods in their photoactive layer. Gold nanorods would increase the quenching energy states that trap the free charge carriers, and serve as recombination centers, which in turn reduces the number of free charge carrier at electrodes, and prevents further enhancement in the device performance. When the concentration of the rods in the concentrated photoactive blend was reduced, as in the 5 wt% case, both power conversion efficiency and short circuit current density of thick devices were enhanced by $\sim 6.5\%$ and 13% , respectively.

7.5 Depositing Au NRs on top of the P3HT:PCBM layer

Motivation: in this approach, we aimed to study the effect of depositing Au NRs on top of the photoactive layer on the performance of our device. It has been reported that

placing the MNPs on the cell's rear electrode is better than having them in the front one although the fraction of the backward scattered light into the cell (from MNPs placed on the cell's rear electrode) is comparable to the forward scattered one (from MNPs placed on the front electrode) [99]. This is due to the point that the loss in the absorption of light at wavelengths with energies $\omega > \omega_{sp}$ is prevented by limiting the destructive interference between the scattered and unscattered light, while keeping the light of lower energy to get coupled inside the cell [9,99,100]. Hence, the optical path length of the incident light would be increased inside the absorber. Furthermore, placing the rods in contact with the photoactive layer makes it possible for the intensified EM field around the rods to reach the photoactive film and excite more charge carriers. These points suggested that having the rods on top of the photoactive layer would lead to better increase in both the EM field and the optical path length of the incident light inside the absorber, which favors the use of the rods in such location. In addition, there have been no previous studies on the effect of depositing metallic nanoparticles in contact to the polymer solar cell's cathode. Figure 7.25 illustrates the position of the NRs in our fabricated OSC.

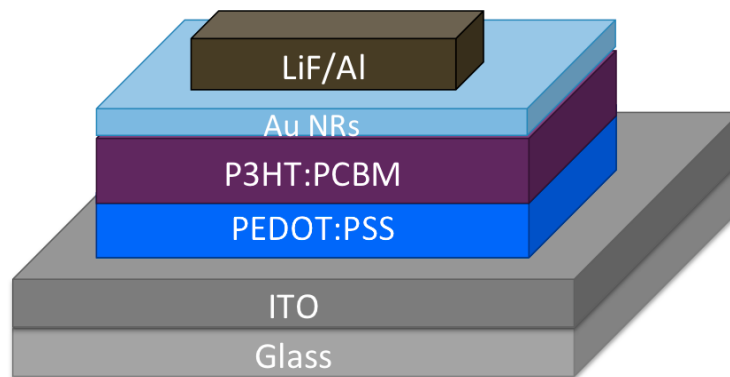


Figure 7. 25: OSC device structure with Au NRs deposited on top of the P3HT:PCBM photoactive layer.

7.5.1 Procedures

In this approach, OSC devices were prepared following our developed recipe mentioned earlier. After spin-coating of the P3HT:PCBM layer, Au NRs layers (1, 3 and 5 layers) were directly deposited on top of the photoactive film by spin-coating technique of the Au NRs aqueous solution. The whole process was done inside the nitrogen filled glove-box. The spin-coating of the rods' layer(s) was performed in a two-steps process, first at a slow speed of 200 RPM for 3 sec with 1 sec to reach 110 RPM, then at 1000 RPM for 10 sec with 5 sec to reach 550 RPM. After depositing the rods, devices were annealed at 150°C for 30 min to be dehydrated, then the LiF/Al cathode layers were thermally evaporated. No post-annealing treatment was done to the devices after the cathode deposition since we have noticed from our various experiments that the combination between pre- and post- annealing treatment on OSC devices reduced their performance dramatically.

7.5.2 Results and discussions

To compare both of the microscopic and spectroscopic properties of the deposited Au NRs layers, one, three and five layers of Au NRs were separately spin-coated on ITO-coated glass. The SEM images in figure 7.26 show that such spin-coating deposition produced Au NRs with various densities and arbitrary alignments on the substrate. Accordingly, the spectral measurements of the obtained rods layers, illustrated in figure 7.27, were different.

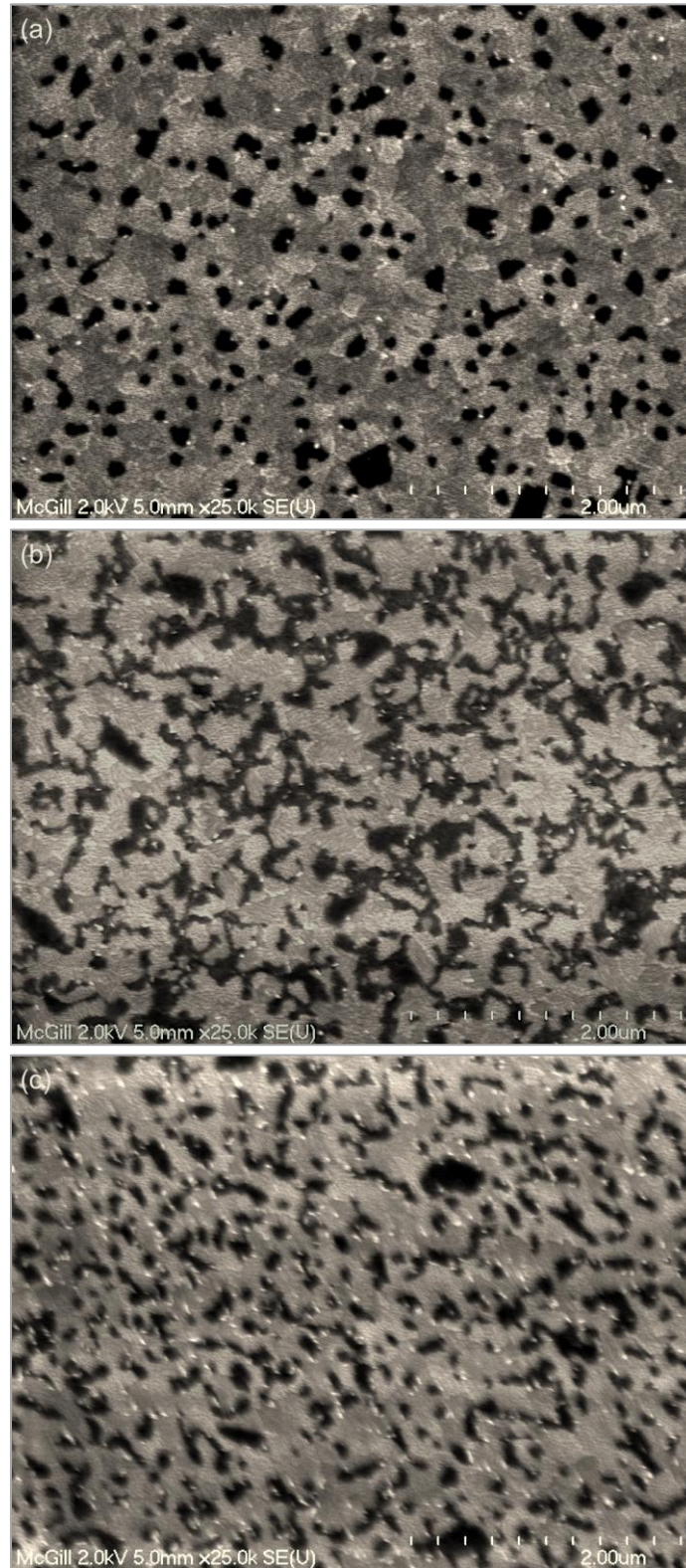


Figure 7. 26: SEM images for various layers of Au NRs spin-coated on ITO-coated glass: (a) 1 layer; (b) 3 layers; and (c) 5 layers. The white droplet-like structures indicate the Au NRs. The bar indicates 2 microns.

The presence of Au NRs with different alignments at the ITO surface explains the appearance of the two peaks in the spectrum of figure 7.27. More intense peaks were observed for the five layers deposit, which produced denser rods in the layer ($\sim 4 \times 10^9$ cm^{-2}). For one and three layers of rods, the particles densities were $\sim 8 \times 10^8$ and 1×10^9 cm^{-2} , respectively.

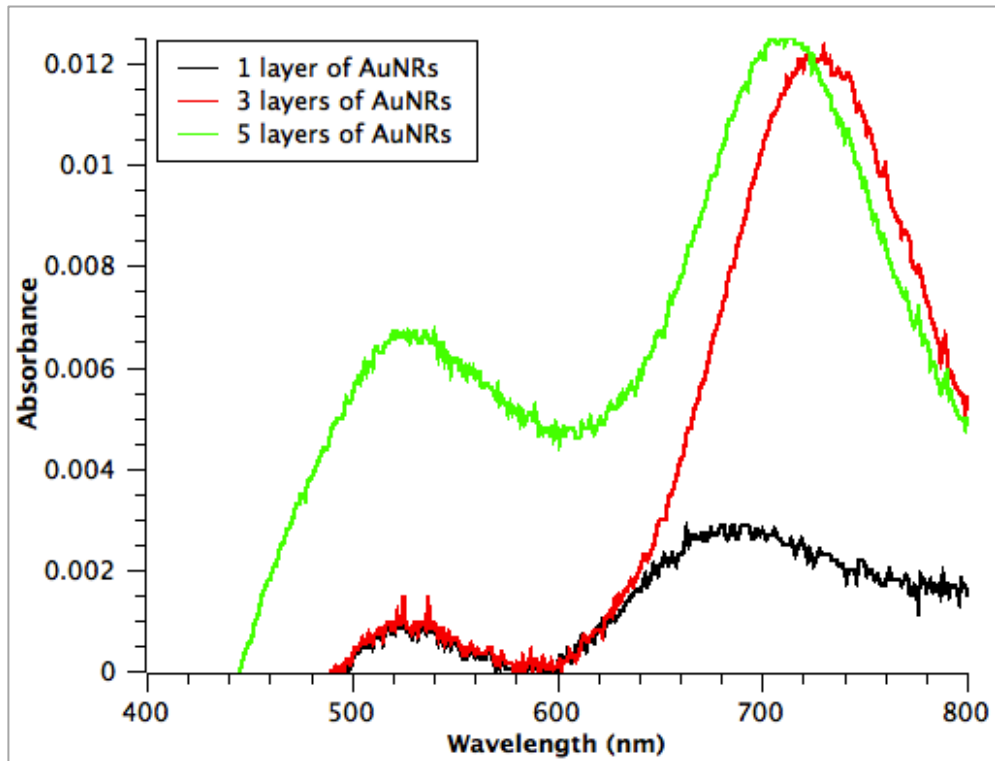


Figure 7. 27: UV-Vis spectra for 1, 3, and 5 layers of Au NRs spin-coated on top of ITO-coated glass.

To examine the effect of incorporating Au NRs on top of the photoactive layer of the OSC devices, the PV parameters of fully fabricated devices with/without rods were measured and compared. Figures 7.28 illustrates the JV curves under illumination and in dark conditions for reference device along with devices incorporated Au NRs on top of

the photoactive layer, and table 10 summarizes their corresponding PV parameters. As table 10 shows, depositing the Au NRs on top of the P3HT:PCBM film increased the J_{sc} by up to 5% which succeeded to enhance the PCE by up to 14.1% for devices incorporated with one layer of Au NRs. However, devices with 3 and 5 layers of the rods on top of the photoactive layer showed a slight decrease in the PCE. The increase in the device performance via incorporating a layer of the rods in contact to the cell's back electrodes could be explained by the following mechanisms: the EM associated with the LSPR in Au NRs (near field effect) was intensified near the photoactive layer, or the optical path length of the incident light inside the photoactive layer was increased due to the backward scattering (far field effect) of the incident light [9,44,99]. Both mechanisms will result in intensification in the incident light inside the P3HT:PCBM layer, leading to better generation of the charge carriers in such layer. This would cause the increase in the J_{sc} and the enhancement in the PCE of the resulting device.

Table 10: The average PV parameters for pristine and P3HT:PCBM/AuNRs devices with 1,3, and 5 layers of the rods, and the corresponding stander deviation.

Device type	Rods density/cm ²	V_{oc} (V)	J_{sc} (mA/cm ²)	R_S (Ω cm ²)	FF%	PCE%
Reference	-	0.58	-4.61 ± 0.19	10.5	59.4	1.56 ± 0.03
1 layer AuNRs	~ 8 × 10 ⁸	0.58	-4.82 ± 0.11	10.5	62.6	1.78 ± 0.03
3 layers AuNRs	~ 1 × 10 ⁹	0.58	-4.24 ± 0.05	18.2	60.9	1.46 ± 0.01
5 layers AuNRs	~ 4 × 10 ⁹	0.58	-4.61 ± 0.02	22.2	56.2	1.47 ± 0.01

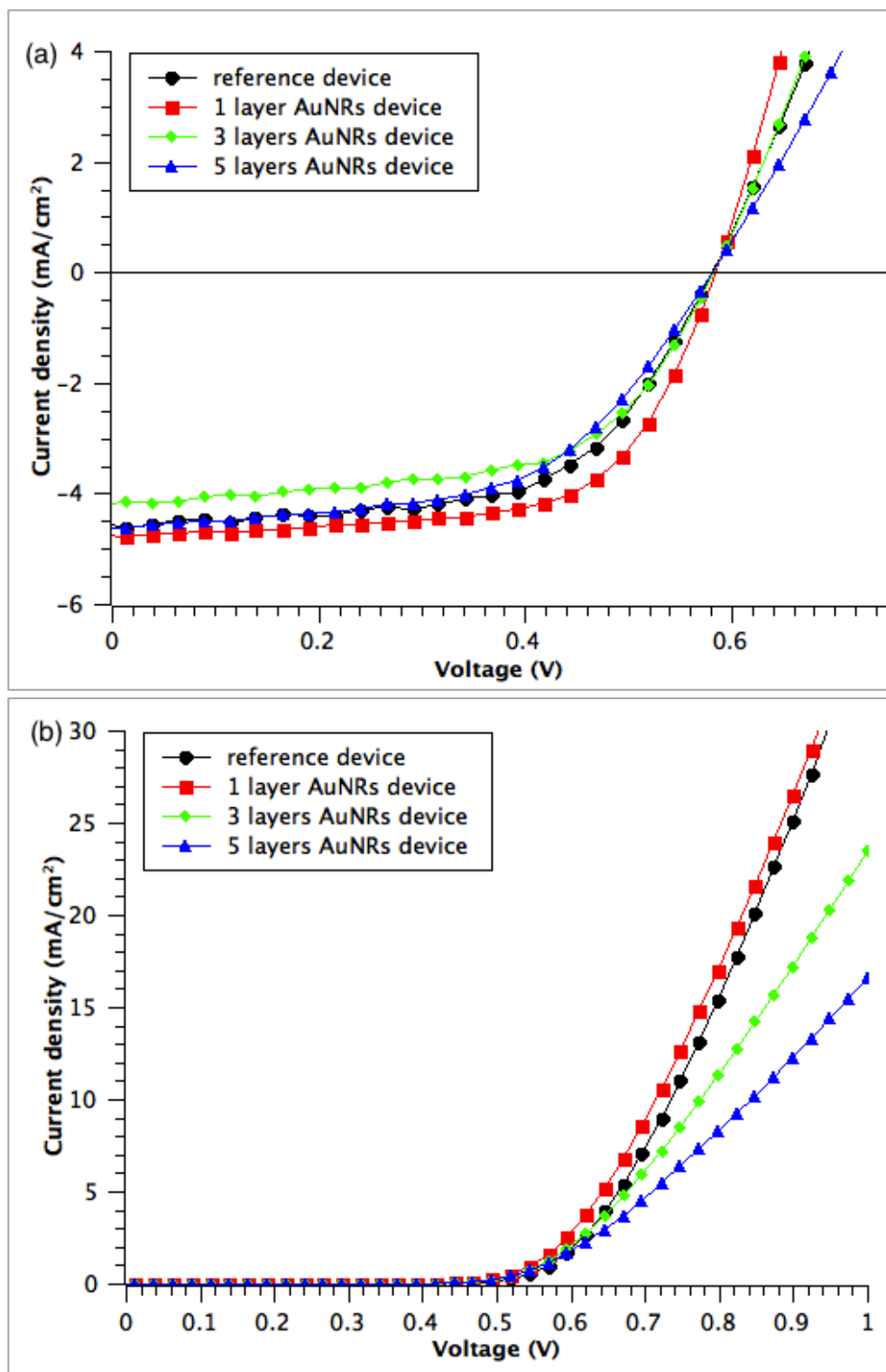


Figure 7. 28: The JV curves for reference P3HT:PCBM device along with devices incorporating 1, 3, and 5 layers of Au NRs on top of P3HT:PCBM (a) Under illumination and; (b) In dark.

Figure 7.29a shows the spectral measurements of the photogenerated current density for reference device along with the one that incorporated a layer of Au NRs on top of the photoactive film. The photocurrent measurements give a picture of the photogenerated charge carriers upon light illumination [100]. It is obvious that the J_{sc} was enhanced by the deposition of the rods layer. To study the effect of the multi-modes excitation of the nanorods on the photogenerated current density before (J_{Re}) and after (J_{NR}) incorporating one layer of Au NRs on the cell's rear electrode, we investigated in figure 7.30b the spectral measurements of the ratio J_{NR}/J_{Re} along with the spectrum of Au NRs solution. Since the absorption of our photoactive film does not exceed 650 nm, there was a decrease in the enhancement of the photogenerated current around 680-760 nm. As figure 7.29b depicts, the J_{Re} enhanced by 1.13, 1.14 and 1.16 folds, respectively, at 460, 640 and 670 nm. These remarkable enhancements in the J_{Re} are, respectively, near the transverse absorption mode of the Au NRs and the tail of the longitudinal one considering the probability of shifting the absorption maxima for Au NRs with changing the surrounding environments. The increase in the J_{Re} could be related to the increase in the generated free charge carriers in the photoactive film due to the backward scattering process from the rods, or the intensification of the EM field surrounding them. Although there was no large enhancement in the absorption profile of the P3HT:PCBM/AuNRs films near the IR region, a very small increase in the J_{Re} was observed at this region, particularly at 670-700 nm, which can be attributed to the longitudinal absorption mode of Au NRs. Hence, we suggested that the photogeneration of excitons near the transverse and longitudinal absorption modes of Au NRs was enhanced, which improved the total device efficiency. Our results are somewhat similar to those obtained by Xiaohong et. al.

[34] who reported on enhancements in organic cells with gold nano-films thermally evaporated in vacuum onto a LiF/Al electrode. Their results showed an enhancement in the J_{NR}/J_{Re} ratio near the absorption profile of nanotextured Au thin films.

For more than a layer of the rods on the P3HT:PCBM film, 3 and 5 layers cases, as presented in table 10, there was a reduction in the values of both J_{sc} and PCE than the corresponding ones in the reference device. Since these devices have denser rods on top of the photoactive film with arbitrary orientations, the possibility of having some rods embedded in the photoactive film is increased. Hence, we would expect that the photogenerated excitons near the P3HT:PCBM/AuNRs interface to be subjected to recombination, which in turn lowered the numbers of free charge carriers that reached the electrodes in these cases, and thus reduced both J_{sc} and PCE [23,92].

Table 10 also reveals that the devices series resistance (R_S) was increased from 10.5 to 22.5 Ωcm^2 with having more than a layer of Au NRs deposited on top of the photoactive film. The increase in R_S lead to a reduction in the FF from ~ 63 to 56%. The increase and decrease in both R_S and FF, respectively, affected the overall performance of the resulting device. Since Au NRs were dispersed in an aqueous solution, we suggest that having more than a layer of Au NRs on top of the photoactive film will accelerate the diffusion of oxygen and water into the photoactive layer, which resulted in the device degradation. The increase in the devices R_S could be considered as an evidence for the degradation of the photoactive film [101]. This degradation would be another reason for the reduction in the device performance with more than a layer of the rods on top of the photoactive film.

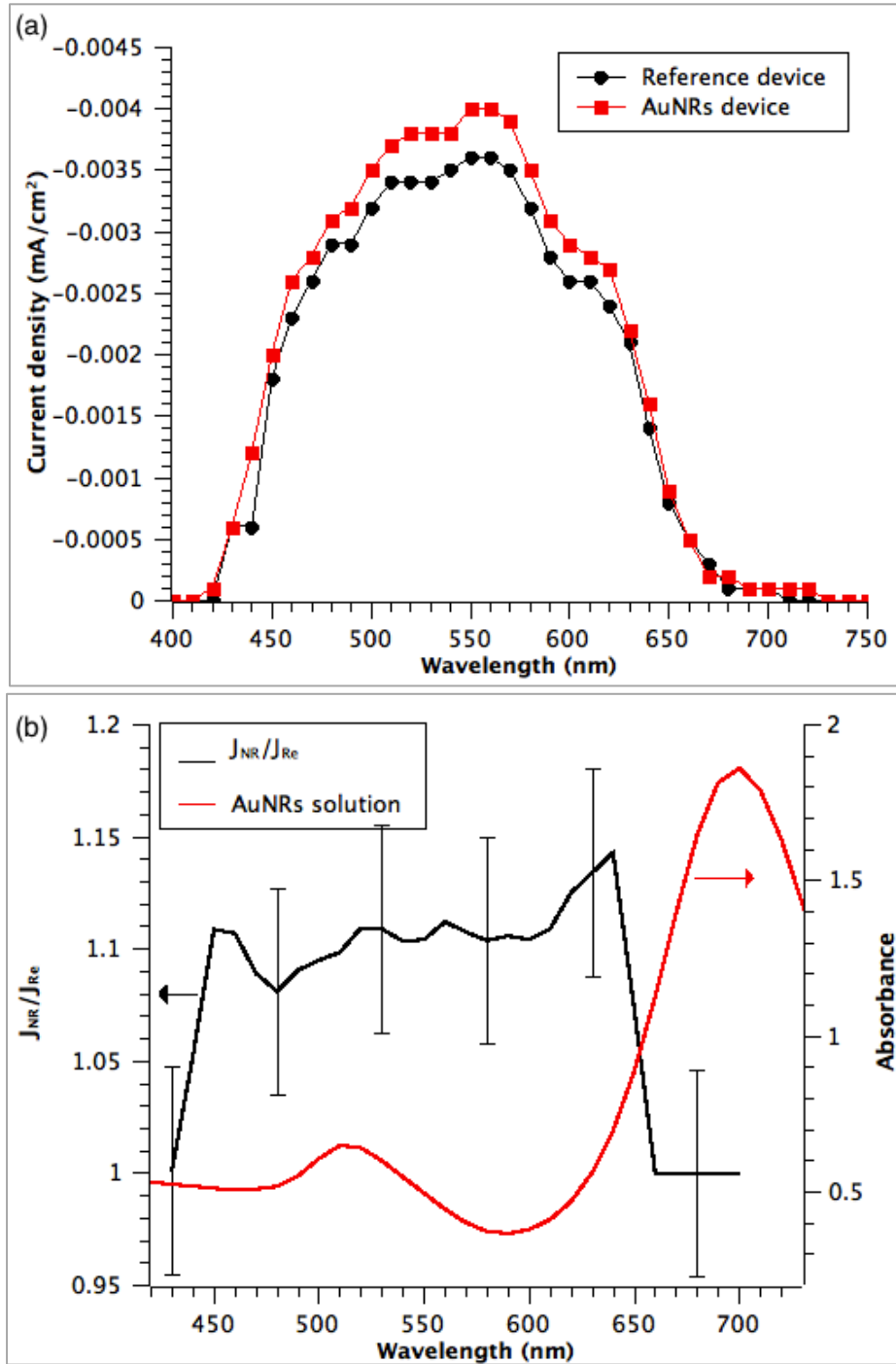


Figure 7.29: (a) The J_{sc} spectral response for pristine P3HT:PCBM device along with the P3HT:PCBM:AuNRs (1 layer) one; (b) J_{Re}/J_{NR} spectra (for 1 layer NRs) along with the absorbance of the Au NRs water-based solution. The curve has been smoothed and the bars indicate the errors.

7.5.3 Conclusion

We achieved $\sim 14\%$ and 5% increase, respectively, in power conversion efficiency and short circuit current density of polymer solar cells by spin-coating a layer of Au NRs on top of the photoactive film in contact with the cell's rear electrode. The improvement in the device performance was related to both far field and near field effect associated with the LSPR of Au NRs. The spectral measurements of the short circuit current revealed that its values were increased near the plasmonic absorption modes of the rods. More than a layer of Au NRs (3 and 5 layers cases) on top of the photoactive film, however, decreased the overall performance of the resulting devices. We found that dense Au NRs in the layer increased the devices series resistance by up to 12.5% . Such increase in the series resistance would be considered as an evidence for the degradation of the photoactive layer, which negatively affected both devices' short circuit current and power conversion efficiency. Results of this section have been recently reported in [102].

Main findings and future work

This experimental investigation on the effect of incorporating gold nanorods into P3HT:PCBM bulk heterojunction organic solar cells shows that such approach produced a remarkable enhancement in the device performance, in which the power conversion efficiency was increased by up to 21.3%.

In our study, we used the reported hypotheses regarding the effect of both far field and near field effects associated with the localized surface plasmon resonance in gold nanorods to explain the resulted data. However, we cannot emphasize on the exact effect (far field or near field) that was the reason behind enhancing (or reducing) the device performance.

We are presenting, in table 11, all of our approaches for incorporating gold nanorods in the organic solar cell devices along with their effects on the devices' photovoltaic parameters. There is no doubt that inserting gold nanorods in our devices had a good impact on the overall performance of the device.

Table 11: The effect of using different approaches of incorporating Au NRs in BHJ-OSC devices in the PV parameters of the resulting devices.

Used approach for inserting AuNRs on OSC	Rods surface density/cm ²	Effect on V_{oc}	Effect on J_{sc}	Effect on R_s	Effect on FF	Effect on PCE
In contact with front electrode	$\sim 6 \times 10^8$	-	+17%	-	-	+18%
Embedded with anodic buffer layer	$\sim 6-8 \times 10^8$	-	+17%	-36%	-	+21.3%
Embedded with photoactive layer	$> 6 \times 10^8$	-	+13.4%	-24%	-2%	+6.5%
In contact with rear electrode	$\sim 8 \times 10^8$	-	+05%	-	-	+14%

We have found that:

- Using the rod-shape of gold nanoparticles in photovoltaic applications is a very promising approach to enhance their performance since a fairly low density of the rods results in an enormous positive impact on their parameters.
- The multi-modes excitations of the surface plasmon resonance in gold nanorods were active.
- The external quantum efficiency of our devices was enhanced by up to 12-14% near the transverse absorption mode of rods and the tail of the longitudinal one. These enhancements are higher than what is reported in the literature, showing the advantage of using Au NRs over other shapes of the nanoparticles
- Gold nanorods enhanced both external quantum efficiency and short circuit current near IR region, which is related to the longitudinal absorption mode of the rods.
- The influence of embedding the rods in the photoactive film depends strongly on the film thickness. The absorption of the thin film is more affected by the presence of the rods as compared with the thick one.
- The best way of incorporating gold nanorods into organic solar cell devices is by blending them with the solution of the anodic buffer layer due to its intermediate position between the anodic electrode and the photoactive layer, which enable the both the far field and near field effects of the nanorods.
- Dense gold nanorod in the layer have negative impact on the device performance. This could be due to: increasing in the destructive interference between scattered and transmitted light, which reduces the amplitude of the electric field inside the

photoactive layer, or increasing in the excitons quenching energy states, which increases the recombination of the free charge carriers.

Although our experimental work highlighted important points regarding the effect of incorporating gold nanorods into polymer solar cells, there is still a lot of work to be done for a better understanding of this subject. From the experimental point of view, uniformly deposited rods with various orientations would provide researchers with a clearer idea regarding the effect of plasmonic modes on the device performance; an additional layer of gold nanostructure incorporated in the cathode surface would be of interest to study the effect of induced coupling between localized and delocalized surface plasmon resonances on the cell behavior. This field of study would be a rich experimental and theoretical area. Further investigation, optimizations and characterizations are required for a full understanding of the plasmonic solar cells subject. In addition, theoretical considerations regarding the coupling between adjacent nanoparticles, ohmic loss, and interference effects are required for underlying the physical mechanisms behind the associated increase/decrease in the photovoltaic parameters via incorporating gold nanorods into polymer solar cells. Finally, it would be equally interesting to consider the optoelectronic model proposed recently by Zhu *et al.* [103] in which the optical properties of the plasmonic active layers are described by an effective medium theory and an organic semiconductor model is used to study the short-circuit photocurrent influenced by the plasmonic particles. Such model has indeed the potential to provide an excellent tool for the design, fabrication and optimization of plasmonic organic solar cells.

Bibliography

1. S. Solomon, D. Qin, M. Manning, Z. Chen, M. Marquis, K.B. Averyt, M.Tignor, H.L. Miller (eds.): Climate Change 2007: The Physical Science Basis. Contribution of Working Group I to the Fourth Assessment Report of the Intergovernmental Panel on Climate Change., IPCC, Cambridge and New York (2007)
2. Martin I. Hoffert, Ken Caldeira, Gregory Benford, David R. Criswell, Christopher Green, Howard Herzog, Atul K. Jain, Haroon S. Kheshgi, Klaus S. Lackner, John S. Lewis, H. Douglas Lightfoot, Wallace Manheimer, John C. Mankins, Michael Mauel, L. John Perki: Advanced Technology Paths to Global Climate Stability: Energy for a Greenhouse Planet. Science 298, 981-987 (2002)
3. Nathan S. Lewis, Daniel G. Nocera: Powering the Planet: Chemical Challenges in Solar Energy Utilization. PNAS 103, 15729-15735 (2006)
4. Ottmar Edenhofer, Ramón Pichs Madruga, Youba Sokona, Kristin Seyboth, Patrick Matschoss, Susanne Kadner, Timm Zwickel, Patrick Eickemeier, Gerrit Hansen, Steffen Schlömer, Christoph Von Stechow: Renewable Energy Sources and Climate Change Mitigation., IPCC, New York (2012)
5. Ashok, S.: Encyclopedia Britannica. In: Solar Energy. Available at: <http://www.britannica.com/EBchecked/topic/552905/solar-energy>. Accessed on 19 July 2012.
6. S. O. Kasap: Optoelectronics and Photonics: Principles and Practies. Prentice-Hall,

- Inc., New Jersey (2000)
7. The History of Solar. In: U.S. Department of Energy- Energy Efficiency and Renewable Energy. Available at:

http://www1.eere.energy.gov/solar/pdfs/solar_timeline.pdf. Accessed on 14 March 2012
 8. Research Cell Efficiency Records. In: National Center for Photovoltaics. Available at: http://www.nrel.gov/ncpv/images/efficiency_chart.jpg. Accessed on 13 March 2013
 9. Harry A. Atwater, Albert Polman: Plasmonics for Improved Photovoltaic Devices. Nature Materials 9, 205-213 (2010)
 10. Arnulf Jäger-Waldau: PV Status Report 2010., European Commission (2010)
 11. P. A. Troshin, R. N. Lyubovskaya, V. F. Razumov: Organic Solar Cells: Structure, Materials, Critical Characteristics, and Outlook. Nanotechnologies in Russia 3, 242–271
 12. Meng Tao: Inorganic Photovoltaic Solar Cells: Silicon and Beyond. The Electrochemical Society Interface 17, 30-35 (2008)
 13. Federik C. Krebs, Jan Alstrup, Holger Spanggaard, Kaj Larsen, Esben kold: Production of Large-Area Polymer Solar Cells by Industrial Silk Screen Printing, Lifetime Considerations and Lamination with Polyethyleneterephthalate. Solar

- Energy Materials & Solar Cells 83, 293-300 (2004)
14. Carsten Deibel, Vladimir Dyakonov: Polymer–Fullerene Bulk Heterojunction Solar Cells. Reports on Progress in Physics 73, 096401 (2010)
 15. Li LiGui, Lu GuangHao, Yang XiaoNiu, Zhou EnLe: Progress in Polymer Solar Cell. Chinese Science Bulletin 52, 145-158 (2007)
 16. Arun Tej Mallajosyula, Naveen Srivastava, S. Sundar Kumar Iyer, Baquer Mazhari: Characterization of Matrix and Isolated Organic Solar Cells. Solar Energy Materials & Solar Cells 94, 1319–1323 (2008)
 17. Selya Price, Robert Margolis: 2008 Solar Technology Market Report., Energy Efficiency & Renewable Energy (2010)
 18. W. Shockley, H. J. Queisser: Detailed Balance Limit of Efficiency of PN Junction Solar Cells. Journal of Applied Physics 32 (1961)
 19. Chu-Jung Ko, Yi-Kai Lin, Fang-Chung Chen, Chi-Wei Chu: Modified Buffer Layers for Polymer Photovoltaic Devices. Applied Physics Letters 90, 063509 (2007)
 20. Markus C. Scharber, David Mühlbacher, Markus Koppe, Patrick Denk, Christoph Waldauf, Alan J. Heeger, Christoph J. Brabec: Design Rules for Donors in Bulk-Heterojunction Solar Cells-Towards 10 % Energy-Conversion Efficiency. Advanced Materials 18, 789–794 (2006)

21. Adam J. Moulé, Jörg B. Bonekamp, Klaus Meerhol: The effect of Active Layer Thickness and Composition on the Performance of Bulk-Heterojunction Solar Cells. *Journal of Applied Physics* 100, 094503 (2006)
22. J. Peet, I. Wen, P. Byrne, S. Rodman, K. Forberich, Y. Shao, N. Drolet, R. Gaudiana, G. Dennler, D. Waller: Bulk Heterojunction Solar Cells with Thick Active Layers and High Fill Factors Enabled by a Bithiophene-Co-Thiazolothiazole Push-Pull Copolymer. *Applied Physics Letters* 98, 043301 (2011)
23. Woo-Jun Yoon, Kyung-Young Jung, Jiwen Liu, Thirumalai Duraisamy, Rao Revur, Fernando-L Teixeira, Suvankar Sengupta, Paul-R Berger: Plasmon-Enhanced Optical Absorption and Photocurrent in Organic Bulk Heterojunction Photovoltaic Devices Using Self-Assembled Layer of Silver Nanoparticles. *Solar Energy Materials & Solar Cells* 94, 128-132 (2010)
24. Jyh-Lih Wu, Fang-Chung Chen, Yu-Sheng Hsiao, Fan-Ching Chien, Peilin Chen, Chun-Hong Kuo, Michael H. Huang, Chain-Shu Hsu: Surface Plasmonic Effects of Metallic Nanoparticles on the Performance of Polymer Bulk Heterojunction Solar Cells. *ACS Publications* 5, 959-967 (2011)
25. M. Pelton, J. Aizpurua, G. Bryant: Metal-Nanoparticle Plasmonics. *Laser & Photonics Reviews* 2, 136–159 (2008)
26. S. Pillai, M.A. Green: Plasmonics for Photovoltaic Applications. *Solar Energy Materials & Solar Cells* 94, 1481–1486 (2010)

27. Anthony J. Morfa, Kathy L. Rowlen: Plasmon-Enhanced Solar Energy Conversion in Organic Bulk Heterojunction Photovoltaics. *Applied Physics Letters* 92, 013504 (2008)
28. David Duche, Philippe Torchio, Ludovic Escoubas, Florent Monestier, Jean-Jacques Simon: Improving Light Absorption in Organic Solar Cells by Plasmonic Contribution. *Solar Energy Materials & Solar Cells* 93, 1377-1382 (2009)
29. Seok-Soon Kim, Seok-In Na, Jang Jo, Dong-Yu Kim, Yoon-Chae Nah: Plasmon Enhanced Performance of Organic Solar Cells Using Electrodeposited Ag Nanoparticles. *Applied Physics Letters* 93, 073307 (2008)
30. Ji-Hwang Lee, Jong-Hwan Park, Jong-Soo Kim, Dong-Yun Lee, Kilwon Cho: High Efficiency Polymer Solar Cells with Wet Deposited Plasmonic Gold Nanodots. *Organic Electronics* 10, 416-420 (2009)
31. Fang-Chung Chen, Jyh-Lih Wu, Chain-Ling Lee, Yi Hong, Chun-Hong Kuo, Micheal H. Huang: Plasmonic-Enhanced Polymer Photovoltaic Devices Incorporating Solution-Processable Metal Nanoparticles. *Applied Physics Letters* 95, 013305 (2009)
32. Linfang Qiao, Dan Wang, Lijian Zuo, Yuqian Ye, Jun Qian, Hongzheng Chen, Ailing She: Localized Surface Plasmon Resonance Enhanced Organic Solar Cell with Gold Nanospheres. *Applied Energy* 88, 848–852 (2011)
33. Dong Hown Wang, Do Youb Kim, Kyeong Woo Choi, Jung Hwa Seo, Sang Hyuk

- Im, Jong Hyeok Park, O. Ok Park, Alan J. Heeger: Enhancement of Donor-Acceptor Polymer Bulk Heterojunction Solar Cell Power Conversion Efficiencies by Addition of Au Nanoparticles. *Angewandte Chemie International Edition* 50, 5519-5523 (2011)
34. Xiaohong Chen, Chunchang Zhao, Lewis Rothberg, Man-King Ng: Plasmon Enhancement of Bulk Heterojunction Organic Photovoltaic Devices by Electrode Modification. *Applied Physics letters* 93, 123302 (2008)
35. Tapan K. Sau, Andrey L. Rogach, Frank Jackel, Thomas A. Klar, Jochen Feldmann: Properties and Applications of Colloidal Nonspherical Noble Metal Nanoparticles. *Advanced Materials* 22, 1805–1825 (2010)
36. Sam-Shajing Sun, Niyazi Serdar Sariciftci: *Organic Photovoltaics: Mechanisms, Materials, and Devices*. CRC Press, USA (2005)
37. Chiu-Sheng Ho, E-Ling Huang, Wei-Chou Hsu, Ching-Sung Lee, Ying-Nan Lai, Wen-Hsuan Lai: Effects of Annealing on Polymer Solar Cells with High Polythiophene–Fullerene Concentrations. *Japanese Journal of Applied Physics* 50, 04DK21 (2011)
38. Miscibility Research Highlighted in Advanced Light Source News. In: Ade Research Group. Available at: <http://carbon.physics.ncsu.edu/2011/05/miscibility-research-highlighted-in-advanced-light-source-news/>. Accessed on 21 July 2012
39. Serap Gunes; Helmut Neugebauer, Niyazi Serdar Sariciftci: Conjugated Polymer-

- Based Organic Solar Cells. Chemical Review 107, 1324-1338 (2007)
40. Attila J. Mozer, Niyazi Serdar Sariciftci: Conjugated Polymer Photovoltaic Devices and Materials. Comptes Rendus Chimie 9, 568-577 (2006)
41. Available at:

<http://dissertations.ub.rug.nl/FILES/faculties/science/2008/l.m.popescu/01-c1.pdf>

Accessed on 20 July 2012
42. Sigma and Pi Bonds. Available at:

http://www.mhhe.com/physsci/chemistry/animations/chang_7e_esp/bom5s2_6.swf

Accessed on 20 July 2012
43. Gang Li, Vishal Shrotriya, Yan Yao, Yang Yang: Investigation of Annealing Effects and Film Thickness Dependence of Polymer Solar Cells Based on Poly(3-hexylthiophene). Journal of Applied Physics 98, 043704 (2005)
44. Wanli Ma, Cuiying Yang, Xiong Gong, Kwanghee Lee, Alan J. Heeger: Thermally Stable, Efficient Polymer Solar Cells with Nanoscale Control of the Interpenetrating Network Morphology. Advanced Functional Materials 15, 1617-1622 (2005)
45. Steffan Cook, Akihiro Furube, Ryuzi Katoh, Liyuan Han : Estimate of Singlet Diffusion Lengths in PCBM Films by Time-Resolved Emission Studies. Chemical Physics Letters 478, 33–36 (2009)
46. Li-Min Chen, Zheng Xu, Ziruo Hong, Yang Yang: Interface Investigation and

- Engineering - Achieving High Performance Polymer Photovoltaic Devices. *Journal of Materials Chemistry* 20, 2575–2598 (2010)
47. M. A. López, J. C. Sánchez, M. Estrada: Characterization of PEDOT:PSS Dilutions for Inkjet Printing Applied to OLED Fabrication. In : *Devices, Circuits and Systems, 7th International Caribbean Conference on*. IEEE (2008)
48. Christoph J. Brabec, Sean E. Shaheen, Christoph Winder, N. Serdar Sariciftci: Effect of LiF/Metal Electrodes on the Performance of Plastic Solar Cells. *Applied Physics Letters* 80, 1288-1290
49. Weihao Ge: An Overview on P3HT:PCBM, the Most Efficient Organic Solar Cell So Far. Available at:
http://sces.phys.utk.edu/~dagotto/condensed/HW1_2009/osc.pdf. Accessed on 25 July 2012
50. Carsten Deibel: Picture Story – How Do Organic Solar Cells Function? In: *Note on Disordered Matter*. Available at: <http://blog.disorderedmatter.eu/2008/06/05/picture-story-how-do-organic-solar-cells-function/>. Accessed on 25 July 2012
51. Andre Moliton, Jean-Michel Nunzi: Review How to Model the Behaviour of Organic Photovoltaic Cells. *Polymer International* 55, 583-600 (2006)
52. Mario Pagliaro, Giovanni Palmisano, Rosaria Ciriminna: *Flexible Solar Cells*. Wiley-VCH Verlag GmbH & Co., Germany (2008)

53. Carsten Deibel: Polaron, Polaron Pair, Exciton, Exciplex. In: Notes on Disordered Matter. Available at: <http://blog.disorderedmatter.eu/2008/04/15/polaron-polaron-pair-exciton-exciplex/>. Accessed on 25 July 2012
54. Donald A. Neamen: Semiconductor Physics and Devices 3rd edn. McGraw-Hill, New York (2003)
55. Available at: <http://pvcadrom.pveducation.org/CELLOPER/QUANTUM.HTM>. Accessed on 28 July 2012
56. Chetan Singh Solanki: Solar Photovoltaics: Fundamentals, Technologies and Applications 2nd edn. PHI Private Limited, New Delhi (2011)
57. Darren M. Bagnall, Matt Boreland: Photovoltaic Technology. Energy Policy 36, 4390–4396 (2008)
58. C. S. Solanki, G. Beaucarne: Advanced Solar Cell Concepts. Energy for Sustainable Development XI, 17-23 (September 2007)
59. Reference Solar Spectral Irradiance: ASTM G-173. Available at: <http://rredc.nrel.gov/solar/spectra/am1.5/ASTMG173/ASTMG173.html>. Accessed on 31 July 2012
60. Craig F. Bohren, Donald R. Huffman: Absorption and Scattering of Light by Small Particles. Wiley-VCH (2004)
61. William L. Barnes, Alain Dereux, Thomas W. Ebbesen: Surface Plasmon

- Subwavelength Optics. *Nature* 424, 824-830 (2003)
62. W. Andrew Murray, William L. Barnes: Plasmonic Materials. *Advanced Materials* 19, 3771–3782 (2007)
 63. Richard B. M. Schasfoort, Anna J. Tudos: Handbook of Surface Plasmon Resonance. The Royal Society of Chemistry (2008)
 64. Sujit Kumar Ghosh, Tarasankar Pal: Interparticle Coupling Effect on the Surface Plasmon Resonance of Gold Nanoparticles: From Theory to Applications. *Chemical Reviews* 107, 4797–4862 (2007)
 65. Jin Z. Zhang, Cecilia Noguez: Plasmonic Optical Properties and Applications of Metal Nanostructures. *Plasmonics*, 127–150 (2008)
 66. Eliza Hutter, Janos H. Fendler: Exploitation of Localized Surface Plasmon Resonance. *Advanced Materials* 16, 1685-1706 (2004)
 67. Matthew Pelton, Javier Aizpurua, Garnett Bryant: Metal-Nanoparticle Plasmonics. *Laser & Photonics Reviews* 2, 136-159 (2008)
 68. Nanoparticle Synthesis. In: Nanobiotechnology Sönnichsen Group. Available at: http://www.nano-bio-tech.de/157_ENG_HTML.php. Accessed on 10 August 2012
 69. K. R. Catchpole, A. Polman: Design Principles for Particle Plasmon Enhanced Solar Cells. *Applied Physics Letters* 93, 191113 (2008)

70. Vincent Rotello: Nanoparticles Building Blocks for Nanotechnology. Springer, USA (2004)
71. Jorge Perez-Juste, Isabel Pastoriza-Santos, Luis M. Liz-Marzan, Paul Mulvaney: Gold nanorods: Synthesis, Characterization and Applications. Coordination Chemistry Reviews 249, 1870–1901 (2005)
72. What Causes the Colors of Metals Like Gold? In: Causes of the Color. Available at: <http://www.webexhibits.org/causesofcolor/9.html>. Accessed on 7 August 2012
73. Jon A. Schuller, Edward S. Barnard, Wenshan Cai, Young Chul Jun, Justin S. White, Mark L. Brongersma: Plasmonics for Extreme Light Concentration and Manipulation. Nature Materials 9, 193-204 (2010)
74. Juan Yguerabide, Evangelina E. Yguerabide: Light-Scattering Submicroscopic Particles as Highly Fluorescent Analogs and Their Use as Tracer Labels in Clinical and Biological Applications. Analytical Biochemistry 262, 137–156 (1998)
75. S. Pillai, K. R. Catchpole, T. Trupke, M. A. Green: Surface Plasmon Enhanced Silicon Solar Cells. Journal of Applied Physics 101, 093105 (2007)
76. R. K. Harrison, Adela Ben-Yakar: Role of Near-Field Enhancement in Plasmonic Laser Nanoablation Using Gold Nanorods on a Silicon Substrate. Optics Express 18, 22556 (2011)
77. C. R. Simovski, A. J. Viitanen, S. A. Tretyakov: Resonator Mode in Chains of Silver

- Spheres and its Possible Application. *Physical Review E* 72, 066606 (2005)
78. C. Sönnichsen, T. Franzl, T. Wilk, G. Von Plessen, J. Feldmann: Drastic Reduction of Plasmon Damping in Gold Nanorods. *Physical Review Letters* 88, 077402 (2002)
 79. Hiroshi Nakashima: Control of Gold Nanorod Arrays Through Self-Assembly of Biomolecules. *NTT Technical Review* 7 (2008)
 80. Christopher Tabor, Desiree Van Haute, Mostafa A. El-Sayed: Effect of Orientation on Plasmonic Coupling Between Gold Nanorods. *ACS Nano* 3, 3670-3678 (2009)
 81. Gang Li, Vishal Shrotriya, Jinsong Huang, Yan Yao, Tom Moriarty, Keith Emery, Yang Yang : High-Efficiency Solution Processable Polymer Photovoltaic Cells by Self-Organization of Polymer Blends. *Nature Materials* 4, 864-868 (2005)
 82. Taner Aytun, Ayse Turak, Iain Baikie, Grzegorz Halek, Cleva W. Ow-Yang: Solution-Processed LiF for Work Function Tuning in Electrode Bilayers. *Nano Letters* 12, 39-44 (2012)
 83. Kyeong-Seok Lee, Mostafa A. El-Sayed: Dependence of the Enhanced Optical Scattering Efficiency Relative to that of Absorption for Gold Metal Nanorods on Aspect Ratio, Size, End-Cap Shape, and Medium Refractive Index. *The Journal of Physical Chemistry B* 109, 20331-20338 (2005)
 84. Heejoo Kim, Won-Wook So, Sang-Jin Moon: Effect of Thermal Annealing on the Performance of P3HT/PCBM Polymer Photovoltaic Cells. *Journal of the Korean*

Physical Society 48(3), 441-445 (2006)

85. Heejoo Kim, Won-Wook So, Sang-Jin Moon: The Importance of Post-Annealing Process in the Device Performance of Poly(3-hexylthiophene): Methanofullerene Polymer Solar Cell. *Solar Energy Materials & Solar Cells* 91, 581–587 (2007)
86. Kyungkon Kim, Jiwen Liu, Manoj A. G. Namboothiry, David L. Carroll: Roles of Donor and Acceptor Nanodomains in 6% Efficient Thermally Annealed Polymer Photovoltaics. *Applied Physics Letters* 90, 163511 (2007)
87. P. Vanlaekea, A. Swinnenb, I. Haeldermansb, G. Vanhoylandb, T. Aernoutsa, D. Cheynsa, C. Deibela, J. D’Haena, P. Heremansa, J. Poortmansa, J.V. Manca: P3HT/PCBM Bulk Heterojunction Solar Cells: Relation Between Morphology and Electro-Optical Characteristics. *Solar Energy Materials & Solar Cells* 90, 2150–2158 (2006)
88. Tapan K. Sau, Catherine J. Murphy: Seeded High Yield Synthesis of Short Au Nanorods in Aqueous Solution. *Langmuir* 20, 6414-6420 (2004)
89. Vishal Shrotriya, Jianyong Ouyang, Ricky-J Tseng, Gang Li, Yang Yang: Absorption Spectra Modification in Poly(3-hexylthiophene):Methanofullerene Blend Thin Films. *Chemical Physics Letters* 411, 138–143 (2005)
90. Alaa Y. Mahmoud, Jianming Zhang, Jayanta K. Baral, Ricardo Izquierdo, Dongling Ma, Muthukumaran Packirisamy, Vo-Van Truong: Low Density of Gold Nanorods in the Anodic Layer for Enhancing the Efficiency of Organic Solar Cells. In :

Photonics North 2011, vol. Proc. SPIE, 80071V (2011)

91. R. B. Dunbar, T. Pfadler, L. Schmidt-Mende: Highly Absorbing Solar Cells- a Survey of Plasmonic Nanostructures. *Optics Express* 20, 177-189 (2012)
92. Alaa Y. Mahmoud, Jianming Zhang, Dongling Ma, Ricardo Izquierdo, Vo-Van Truong: Optically-Enhanced Performance of Polymer Solar Cells with Low Concentration of Gold Nanorods in the Anodic Buffer Layer. *Organic Electronics* 13, 3102–3107 (2012)
93. Y. Shi, J. Liu, Y. Yang: Device Performance and Polymer Morphology in Polymer Light Emitting Diodes: The Control of Thin Film Morphology and Device Quantum Efficiency. *Journal of Applied Physics* 87, 4254-4263 (2000)
94. Jinfeng Zhu, Mei Xue, Ryan Hoekstra, Faxian Xiu, Baoqing Zenga, Kang L. Wang: Light Concentration and Redistribution in Polymer Solar Cells by Plasmonic Nanoparticles. *Nanoscale* 4, 1978-1981 (2012)
95. Charlie C. D. Wang, Wallace C. H. Choy, Chunhui Duan, Dixon D. S. Fung, Wei E. I. Sha, Feng-Xian Xie, Fei Huang, Yong Cao: Optical and Electrical Effects of Gold Nanoparticles in the Active Layer of Polymer Solar Cells. *Journal of Material Chemistry* 22, 1206–1211 (2012)
96. Feng Liu, Jean-Michel Nunzi: Enhanced Organic Light Emitting Diode and Solar Cell Performances Using Silver Nano-Clusters. *Organic Electronics* 13, 1623–1632 (2012)

97. Mei Xue, Lu Li, Bertrand J. Tremolet de Villers, Huajun Shen, Jinfeng Zhu, Zhibin Yu, Adam Z. Stieg, Qibing Pei, Benjamin J. Schwartz, Kang L. Wang: Charge-Carrier Dynamics in Hybrid Plasmonic Organic Solar Cells with Ag Nanoparticles. *Applied Physics Letter* 98, 253302 (2011)
98. Olivier P. M. Gaudin, Ifor D. W. Samuel, Samia Amriou, Paul L. Burn: Thickness Dependent Absorption Spectra in Conjugated Polymers: Morphology or Interference? *Applied Physics Letters* 96, 053305 (2010)
99. F. J. Beck, A. Polman, K. R. Catchpole: Tunable Light Trapping for Solar Cells Using Localized Surface Plasmons. *Journal of Applied Physics* 105, 114310 (2009)
100. S. H. Lim, W. Mar, P. Matheu, D. Derkacs, E. T. Yu: Photocurrent Spectroscopy of Optical Absorption Enhancement in Silicon Photodiodes via Scattering from Surface Plasmon Polaritons in Gold Nanoparticles. *Journal of Applied Physics* 101, 104309 (2007)
101. Mikkel Jørgensen, Kion Norrman, Frederik C. Krebs: Stability/Degradation of Polymer Solar Cells. *Solar Energy Materials & Solar Cells* 92, 686–714 (2008)
102. Alaa Y. Mahmoud, Neda Etebari Alamdari, Ricardo Izquierdo, Vo-Van Truong: Gold Nanorods on the Cathode Electrode for Enhancing the Efficiency of Polymer Solar Cells. In : *Photonics North 2012*, vol. Proc. SPIE 8412M (2012)
103. J. Zhu, M. Xue, R. Hoekstra, F. Xiu, B. Zeng, K.L. Wang: Light Concentration and Redistribution in Polymer Solar Cells by Plasmonic Nanoparticles. *Nanoscale* 4,

1978-1981 (2012)

104. Meghan Jebb , P. K. Sudeep , P. Pramod , K. George Thomas , Prashant V. Kamat:
Ruthenium(II) Trisbipyridine Functionalized Gold Nanorods. Morphological
Changes and Excited-State Interactions. The Journal of Physical Chemistry B 111,
6839–6844 (2007)
105. Andy Wijaya, Stefan B. Schaffer, Ivan G. Pallares, Kimberly Hamad-Schifferli:
Selective Release of Multiple DNA Oligonucleotides from Gold Nanorods. ACS
Nano 3, 80-86 (2009)

Appendices

Synthesis of water-based and toluene-based gold nanorods

The gold nanorods have been graciously supplied by Professor Dongling Ma of the Institut de la Recherche Scientifique at Varennes (INRS-EMT).

Chemicals and Materials

Hydrogen tetrachloroauric acid ($\text{HAuCl}_4 \cdot 3\text{H}_2\text{O}$), cetyltrimethylammonium bromide (CTAB), sodium borohydride (NaBH_4), silver nitrate (AgNO_3) and ascorbic acid (AA) were purchased from Sigma-Aldrich. Ultrapure DI-water (Millipore system) was used throughout the experiments.

1. Synthesis of water-based Au NRs [88]:

- a. *Seed Solution:* CTAB solution (2.5 ml, 0.2 M) was mixed with 1.5 ml of 1 mM $\text{HAuCl}_4 \cdot 3\text{H}_2\text{O}$ and stirred for a while. Afterwards, 0.6 ml of ice-cold 0.01 M NaBH_4 was added to the stirred solution. As a result, a brownish-yellow seed solution is formed. Vigorous stirring of the seed solution was continued for 2 min. The solution was kept at 25°C after stirring.
- b. *Growth solution:* the growth solution was prepared by mixing all the following components: 10 ml of 0.2 M CTAB, 560 μl of 4 mM AgNO_3 , 1 ml of 15 mM $\text{HAuCl}_4 \cdot 3\text{H}_2\text{O}$ and 9 ml of DI-water. Approximately 250 μl of AA (0.08 M) was

slowly added to the mixture. The addition of ascorbic acid was conducted drop-wise; until the mixture became colorless after adding one quarter more of the total number of droplets to that point.

- c. *Nanorods colloidal solution*: the final step was the addition of 200 μl of the seed solution to the growth solution at 27-30°C. The color of the resulted solution gradually changed into brownish-red within 10-20 min. The temperature of the growth medium was kept constant at 27-30°C during the full procedure. By finishing this step, water-based gold nanorods were produced.

2. Synthesis of toluene-based Au NRs [104,105]:

- d. *Phase transfer to organic solution*: this process includes three steps:
- I. *Purification*: 20 ml of the water-based Au NRs solution was centrifugated at 9000 RPM for 30 min, following by discarding the clear supernatant, and reloading 20 ml of DI-water. The solution was then sonicated, and the rods were re-dispersed (this step is to remove most of the free CTAB molecules).
 - II. *Phase transfer*: 30 ml of dodecanethiol (DDI) and 40 ml of acetone were successively added to 20 ml of the re-dispersed rods water solution, and shaken for several minutes to mix the liquid layers. The solution was thereafter allowed to stand for phase transfer. The brown water layer at the

bottom became clear, and the top organic layer turned into deep-brown or blue, which indicated the completion of the phase transfer.

- III. *Purification*: this step is to extract the organic layer completely (rods inside) to remove excessive DDT. 20 ml of methanol was added to 10 ml of the above prepared organic solution, mixed, and then centrifugated at 8000 RPM for 20 min. Afterwards, supernatant was discarded and 20 ml of methanol was reloaded to re-disperse the rods. The resulting solution was then centrifugated again at 8000 RPM for 20 min. Supernatant was discarded and toluene was introduced to disperse the rods.